



Universiteit Utrecht

Utrecht University
Faculty of Geosciences
Department of Earth Sciences
Geochemistry

Master Thesis

The fate of phosphorus in methane-rich sediments in three eutrophic coastal systems

Luisa Joëlle Kubeneck
Marine Sciences

Utrecht, 5th of May 2018

Supervisors
Prof. Dr. Caroline Slomp
Dr. Sairah Malkin
Wytze Lenstra, MSc

Acknowledgment

I would like to thank my three supervisors Caroline Slomp, Sairah Malkin and Wytze Lenstra. I am grateful for your guidance and support during this work. I appreciated that your doors were always open for all my questions. A special thanks to Wytze, for helping me with the lab work in Utrecht.

I would also like to thank various lab technicians of GML for their support during the lab work.

I am very grateful for the financial support of the Olaf Schuiling fund, which partly financed this work and made it possible for me to participate in the field work in the USA.

Also a special thanks to the geochemistry group, especially Marie and Martijn, for support during the lab- and writing phase.

For the Chesapeake Bay field- and lab work, I would like to thank Michael Hulme and Robert Nilsen, crew of R/V Rachel Carson (MD, USA), Andrew McCarthy and Pinky Liau for their support during sampling and lab work. I thank also the crew of the R/V Electra and project partners Christoph Humborg and Daniel Conley for the fieldwork in the Baltic Sea in 2017.

Abstract

Anthropogenic activities have led to a worldwide increase in coastal eutrophication. Coastal water column phosphorus (P) has three potential fates: internal recycling prolonging possible eutrophication, export to the open sea, or removal through permanent P burial. The P retention capacity of coastal sediments influences the water quality and management of eutrophication.

Authigenic ferrous phosphates, such as vivianite, have traditionally been thought to play a minor role in P burial in coastal systems. However, recent work suggests that anthropogenic eutrophication may enhance vivianite formation in coastal sediments by inducing a vertical upward migration of the sulphate/ methane transition zone (SMTZ). Consequently, vivianite may form in sulphate-poor, but phosphate- and iron-rich sediments directly below the SMTZ. Besides in the Bothnian Sea, the wider distribution of vivianite in coastal systems remains to be explored.

In this thesis, the fate of permanently buried P at three eutrophic coastal sites, located in the Chesapeake Bay (USA) and in the Stockholm Archipelago (Sweden), is studied. A combination of porewater, solid phase and spectroscopic data highlight the importance of sulfur-iron dynamics for P burial. With increasing salinity (associated to higher sulphate concentrations), the total amount of permanently buried P declines. Simultaneously, the iron bound P burial flux decreases. Authigenic ferrous phosphate formation occurs only in two of the three study sites, where the reactive Fe availability surpasses the scavenging capacity of hydrogen sulfide. The spectroscopic data revealed the influence of surrounding geochemical conditions on the elemental composition of vivianite. Cations, such as magnesium and manganese, may play significant roles in vivianite formation. Concluding, the results strongly suggest the importance of formation and burial of iron-bound P as an efficient coastal nutrient filter. As the iron-bound P pool declines with salinity, the coastal P retention capacity declines simultaneously.

Contents

1	Introduction	6
1.1	Theoretical Background	6
1.2	Research questions	10
2	Materials and Methods	11
2.1	Study sites	11
2.1.1	Chesapeake Bay	11
2.1.2	Stockholm Archipelago	13
2.2	Sample collection	14
2.2.1	Chesapeake Bay	14
2.2.2	Stockholm Archipelago	15
2.3	Porewater subsampling	15
2.3.1	Methane sampling & analyses	17
2.4	Solid-phase analyses	17
2.4.1	Total elemental composition and organic carbon	17
2.4.2	Porosity and Grain Size	18
2.4.3	²¹⁰ Pb dating	18
2.4.4	Sulfur extraction	19
2.4.5	Iron sequential extraction	19
2.4.6	Phosphorus extraction	19
2.5	Identification of Fe(II)-phosphates	20
2.5.1	Scanning electron microscopy (SEM)	21
2.5.2	μXRF mapping	21
2.6	Data processing	22
2.6.1	Calculations based on solid phase analyses	22
2.6.2	Saturation calculations	23
3	Results	24
3.1	General characteristics	24
3.2	Porewater profiles	25
3.3	Solid phase profiles	27
3.4	Assessment of the relationship between Fe-P-Mg in sediment burial	33
3.4.1	SEM-EDS	33
3.4.2	μXRF	36
4	Discussion	39
4.1	Steadily versus non-steadily accumulating sedimentary systems	39
4.1.1	Strömmen	39
4.1.2	ET5.1	39
4.1.3	CB2.2	39
4.2	Fe-S-P dynamics	40
4.2.1	Role of vivianite-type minerals in P burial	40

4.2.2	Influence of lateral intrusion on P dynamics: CB2.2	42
4.3	Nature of CDB-P pool	44
4.3.1	Limitations	44
4.3.2	Interactions of Mg in ferrous phosphates	44
4.4	Influence of salinity on coastal nutrient filter capacity	46
4.4.1	Implications	47
5	Conclusion	49
A	²¹⁰Pb ET5.1	60
B	Additional porewater profiles and saturation indices	60
C	CDB fractions & Elemental ratios	64
D	P burial rates	66
E	SEM-EDS images	66
E.1	Strömmen	66
E.2	ET5.1	67
E.3	CB2.2	69
F	Additional μXRF based correlation plots	70
G	Water column trends of study sites	72
G.1	Strömmen	72
G.2	ET5.1	73
G.3	CB2.2	75
H	Calculations to estimate the amount of vivianite in the CDB-step	76
I	Comparison of Strömmen, US5B and Öre estuary	77

List of Figures

1	Schematic of important processes during early diagenetic P transformations in coastal sediments and vertical redox zonation of electron acceptors used for OM degradation	8
2	Schematic of the coupled Fe and HPO_4^{2-} cycles during early diagenesis in coastal sediments	9
3	Study sites ET5.1 & CB2.2 in the Chesapeake Bay, USA	12
4	Location of study site Strömmen, Stockholm Archipelago, Sweden	14
5	Depth profiles of organic carbon, porosity and CaCO_3	24
6	^{210}Pb depth profile and sedimentary composition at CB2.2	25
7	Porewater profiles of each study site	26
8	Depth profiles of total S, Fe, P, Mn, and Mg concentrations at the three study sites	28
9	Depth profiles of S and Fe pool distribution	30
10	Comparison of the degree of pyritization between pyrite determined based on S and Fe extractions for all three study sites	31
11	Depth profile of particulate phosphorus pool distribution	32
12	Ratios used to assess likelihood for the presence of vivianite	33
13	Crystal enriched in Mg and P at 30 cm depth, Strömmen	34
14	Vivianite-like crystal found at 11 cm depth at ET5.1	35
15	Elemental μXRF maps of Fe, P, Mg, Ca and S of Strömmen at 22, 30 and 34 cm .	37
16	Correlation between Fe+ Mn+ Mg to P intensity counts based on the μXRF . . .	38
17	Elemental μXRF maps of ET5.1 at 11 cm depth	38
18	Decline and change in composition in the permanent buried P pool with increasing salinity	46
19	^{210}Pb depth profile and sedimentary composition at ET5.1	60
20	Zoomed in porewater profiles for Strömmen	61
21	Supplement porewater profiles	61
22	Elemental concentrations extracted in the CDB fraction of the SEDEX besides P	65
23	Fe/Al, Fe/S, and S/Al depth profiles at Strömmen	65
24	Overview SEM image of 30 cm sediment depth, Strömmen	67
25	Mg and Fe enriched crystal at 30 cm depth, Strömmen	67
26	Crystals resembling vivianite at 5 and 30 cm depth of ET5.1	68
27	SEM image of CB2.2 at 29 cm indicating an enrichment in pyrite	70
28	Additional μXRF correlation plots	71
29	μXRF count intensity of Cu and Zn against P respectively	72
30	Dissolved oxygen and HPO_4^{2-} concentrations from the water column at Strömmen, 2004-2009	73
31	Annual mean salinity, temperature, oxygen and soluble reactive phosphorus trend in the surface and bottom water at ET5.1 from January 1986 to January 2018 . .	73
32	Soluble reactive phosphorus and dissolved oxygen in the surface and bottom water at ET5.1 from January 1986 to January 2018	74

33	Annual mean salinity, temperature, oxygen and soluble reactive phosphorus trend in the surface and bottom water at CB2.2 from January 1986 to January 2018 . .	75
34	Soluble reactive phosphorus and dissolved oxygen in the surface and bottom water at CB2.2 from January 1986 to January 2018	76
35	Depth profiles of SO_4^{2-} , Fe^{2+} , Mn^{2+} , Mg^{2+} , HPO_4^{2-} , NH_4^+ , Cu, and total S to reactive Fe at Strömmen, US5B and Öre estuary	77

List of Tables

1	Key characteristics of study sites on sampling day	13
2	Sub-sampling and analyses of the porewater	16
3	Overview of the sequential Fe extraction	20
4	Overview of SEDEX	20
5	Investigated depth intervals by the SEM of study sites	21
6	Saturation indices for hydroxylapatite, vivianite, MnHPO_4 and struvite at Strømmen	62
7	Saturation indices for hydroxylapatite, vivianite, MnHPO_4 and struvite at ET5.1 .	63
8	Saturation indices for hydroxylapatite, vivianite, MnHPO_4 and struvite at CB2.2 .	64
9	P burial rates	66
10	Relative elemental abundances in vivianite like crystals at ET5.1	69

1 Introduction

Human activities on land have altered and still alter nutrient cycles and fluxes. Riverine nutrient inputs into estuarine systems have increased 6-50 times for nitrogen (N) from pristine conditions to present, while a 18-180 times increase in phosphorus (P) loading has been observed (Conley, 1999). The increase in primary production and accumulation of organic matter (OM) associated to anthropogenic nutrient enrichment is referred to as eutrophication (Rabalais et al., 2009). It is expected that eutrophication in most estuarine and coastal waters will continue and even intensify in the future due to a rising population, continuous industrialization, intensification of conventional agriculture and consequences of climate changes such as enhanced stratification of aquatic systems (Kemp et al., 2005; Rabalais et al., 2009). Processes change in coastal ecosystems as primary production is increased by eutrophication. The most acute symptoms are hypoxia and harmful algal blooms (Selman et al., 2008). Hypoxia has been reported in the Baltic Sea and the Chesapeake Bay as early as the 1930's (Diaz and Rosenberg, 2008). Since then the number of known regions with severe low oxygen stress (dead zones) has increased exponentially (Diaz and Rosenberg, 2008; Selman et al., 2008).

Mitigating eutrophication is motivated by a desire to maintain valuable ecosystem services, such as recreational and commercial fisheries production and tourism (Conley et al., 2009; Garnier et al., 2010). Such activities may be indirectly, or directly negatively influenced by decreased water quality associated with eutrophication. Consequently, the scientific community needs to improve its understanding on how nutrients are recycled and retained in the coastal zone, and if the coastal zone acts as an efficient nutrient filter preventing nutrient loading to the marine realm. As each coastal system may react differently, location specific monitoring and studies are essential to adequately manage these systems and advise responsible stakeholders (Kemp et al., 2009).

Increasing OM loading associated with eutrophication strongly influences rates and patterns of early diagenetic transformations, with implication for P cycling and burial fluxes (Middelburg and Levin, 2009). Despite a reduction in P input from land, an improvement in water quality has not been observed in some systems (Conley et al., 2009; Kemp et al., 2009). The input of bioavailable P from the sediment to the water column (internal P loading), especially during seasonal hypoxia, is made responsible for prolonging eutrophication (Van Cappellen and Ingall, 1994; Mort et al., 2007; Vahtera et al., 2007). This thesis aims to improve the understanding of bioavailable P burial in coastal sediments, impacting potentially the recovery of coastal waters from eutrophication. The next section will provide a concise overview of sedimentary processes capable of changing sedimentary P retention, highlighting current knowledge gaps.

1.1 Theoretical Background

Most P is introduced to the coastal zone via the rivers (Slomp, 2011) and can then be further transported towards the open sea. Not all of the supplied nutrients enter the open sea as they are retained in the coastal zone (Almroth-Rosell et al., 2016). The coastal zone may act as a nutrient filter, permanently removing bioavailable nutrients from the system (McGlathery et al., 2007).

The only way of permanently removing P from the ecological system is via burial (Ruttenberg, 2003). The efficiency of the burial depends on physical and biogeochemical processes (Nixon et al., 1996; Voss et al., 2005). Understanding the filter efficiencies in different coastal systems, such as estuaries, would contribute to the knowledge necessary for managing the coastal zone's health (Almroth-Rosell et al., 2016). The possible biogeochemical processes influencing the P burial efficiency are explained in the following paragraphs.

Sources of P to the sediment-water interface include allochthonous river-borne inorganic and organic P as well as authochthonous, biogenic P formed by primary production in the euphotic zone and consequent biological recycling in the water column (Figure 1a), (Ruttenberg, 2014). Refractory P phases, for instance detrital apatite, are simply buried in the sediment. Reactive particulate P phases are subject to various biogeochemical processes in the early diagenetic environment, affecting the retention of P in the sediment and the form in which they are ultimately buried (Ruttenberg, 2014). These processes involve OM degradation leading to the release of dissolved phosphate (denoted as HPO_4^{2-} , the dominant phosphate ion at seawater pH), sorption of HPO_4^{2-} onto particulate phases, removal of HPO_4^{2-} during authigenic mineral formation, and benthic efflux of HPO_4^{2-} from sediments to bottom waters (Ruttenberg, 2014), (Figure 1a). The first process regarded is OM degradation.

The first oxidant used for OM degradation is oxygen (O_2) as it provides the greatest amount of free energy (Froelich et al., 1979). High OM fluxes, as during eutrophication, cause O_2 penetration depths to be very shallow (less than 1 mm in muddy sediments) due to high O_2 consumption rates (Glud, 2008). In such systems, anaerobic respiration processes dominate OM degradation using the most efficient remaining electron acceptor (based on Gibbs free energies). After O_2 is consumed, nitrate (NO_3^-) is used, followed by manganese oxides (Mn-oxides) and iron (oxyhydr)oxides (Fe-oxides) and lastly sulphate (SO_4^{2-}) (e.g. Burdige, 2011; Aller, 2014), (Figure 1b). After the depletion of SO_4^{2-} , carbon (C) is used as a terminal electron acceptor, leading to the formation of methane (CH_4).

An important process removing the released HPO_4^{2-} permanently from the porewater is authigenic mineral formation. Three different scenarios of HPO_4^{2-} porewater profiles are indicated in Figure 1a. The exponential increase of HPO_4^{2-} is typical for a steady-state system, in which OM degradation is the sole process controlling HPO_4^{2-} release. No precipitation of authigenic minerals occurs (Berner, 1980). The vertical HPO_4^{2-} profile indicates immediate precipitation/sorption of HPO_4^{2-} , leading to no build up in the porewater. The intermediate case shows an initial build-up of HPO_4^{2-} due to OM degradation/desorption of inorganics and followed by a decline, pointing towards authigenic mineral formation (Ruttenberg, 2014). Of special interest are the processes controlling authigenic mineral formation since it is one major way of permanently burying P and removing it from the water column (Froelich et al., 1982; Ruttenberg, 1993; Compton et al., 2000). Possible authigenic minerals are for instance apatite (e.g. hydroxylapatite ($\text{Ca}_5(\text{PO}_4)_3(\text{OH})_2$)) or ferrous phosphates (e.g. vivianite ($\text{Fe}_3(\text{PO}_4)_2 \cdot 8 \text{H}_2\text{O}$)), (Ruttenberg, 2014).

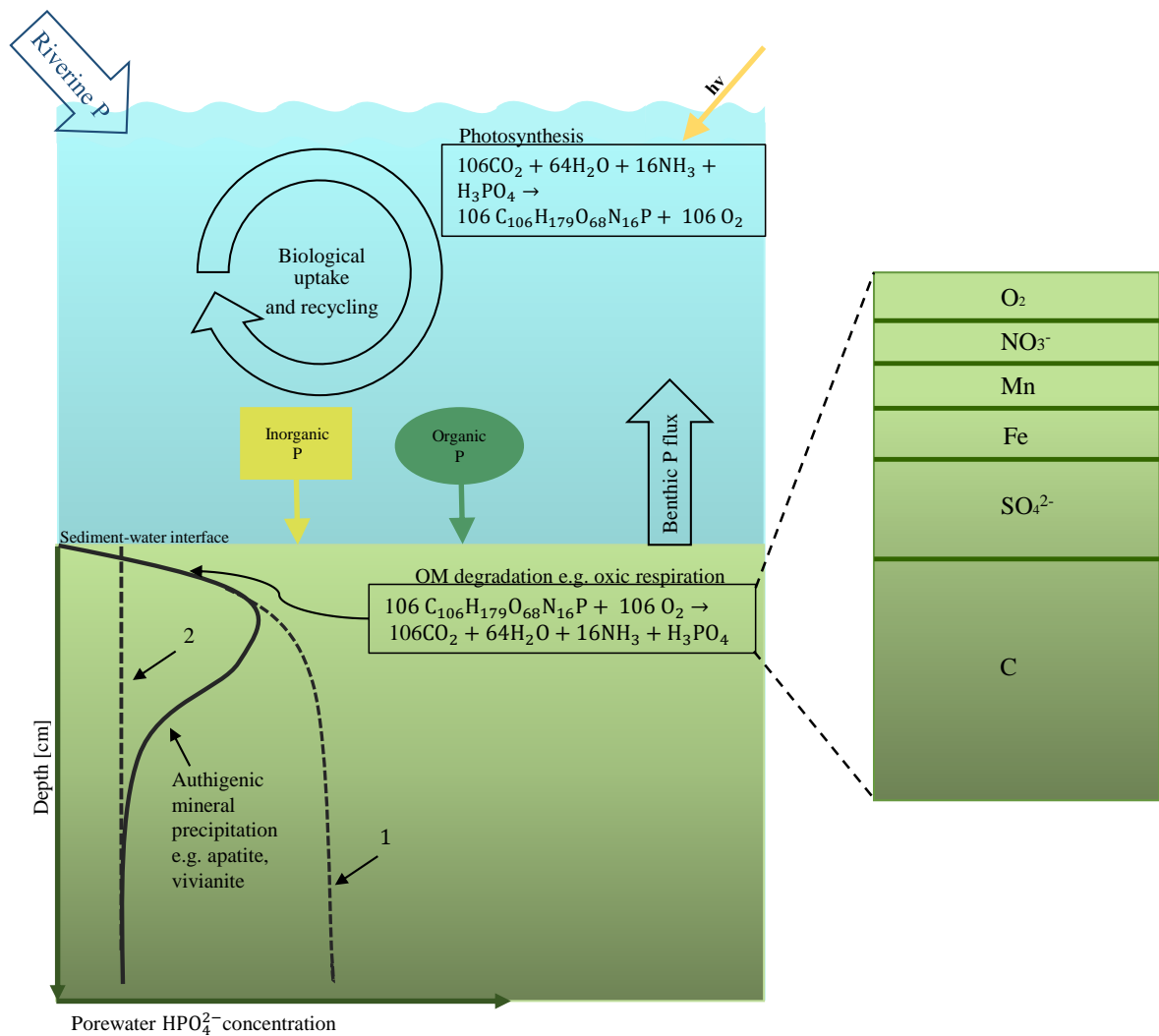


Figure 1: Schematic of important processes during early diagenetic P transformations in coastal sediments. **(a)** P is mainly introduced through rivers to the coastal zone. OM is degraded via microbial respiration in the sediment, releasing HPO_4^{2-} to the porewater. Another important source of HPO_4^{2-} to the porewater is the release of sorbed HPO_4^{2-} from Fe-oxides in suboxic and anoxic sediment. For simplicity, this is not added here. Three schematic porewater profiles for steady-state P diagenesis are shown. The dashed profiles show HPO_4^{2-} profile shapes present when (1) OM degradation is the dominant process, and there is no precipitation (exponential increase of HPO_4^{2-} with increasing depth), and (2) there is immediate precipitation or sorption of HPO_4^{2-} (vertical gradient). The intermediate scenario is demonstrated by the solid curve, in which a reversal of the initially exponentially increasing porewater gradient is observed, implying removal of HPO_4^{2-} from porewaters during authigenic mineral formation. Possible authigenic minerals include for instance hydroxylapatite, ferrous phosphate, struvite (an ammonium-magnesium-phosphate $\text{NH}_4\text{MgPO}_4 \cdot 6\text{H}_2\text{O}$) and manganese phosphate (MnHPO_4). Adapted from Ruttenberg (2014) **(b)** Classical biogeochemical zonation of major electron acceptors that are used for OM degradation. The zonation is based on standard state free energy changes for the remineralization processes. Adapted from Burdige (2011).

The burial of ferrous phosphates is presumed to be limited by the availability of ferrous iron (Fe^{2+}) in sediments with sulfidic bottom waters. Due to the high abundance of SO_4^{2-} in seawater, the

majority of anaerobic OM degradation is coupled to SO_4^{2-} reduction, resulting in the formation of dissolved sulfide (referred to as HS^- , the dominant form at seawater pH), (Jørgensen, 1977, 2006; Soetaert et al., 1996). The HS^- that accumulates below the depth of bioturbation generally removes all reactive Fe-oxides to form ironmonosulfides (FeS) and eventually pyrite (FeS_2), (Berner, 1970; Jensen et al., 1995). Due to the scavenging of reactive Fe by HS^- , it is assumed that P burial in estuarine systems takes mainly place in the form of organic P, authigenic and/or detrital apatite (Schenau and De Lange, 2000; Ruttenger, 2003; Mort et al., 2010).

However, the availability of SO_4^{2-} can be limited at low salinity sites in the coastal zone. In combination with an increased OM input due to eutrophication, the rapid depletion of SO_4^{2-} in the sediment might lead to a shallowing of the sulphate/methane transition zone (SMTZ) (Egger et al., 2014). The shallowing of the SMTZ may enable the preservation of Fe-oxides at depth by reducing the exposure time of Fe-oxides to HS^- (Figure 2). Fe-oxide reduction (also coupled to anaerobic oxidation of methane (AOM)) leads to the release of Fe^{2+} at depth, creating favorable conditions for authigenic ferrous phosphate formation (Egger et al., 2014; Gao et al., 2017) (Figure 2).

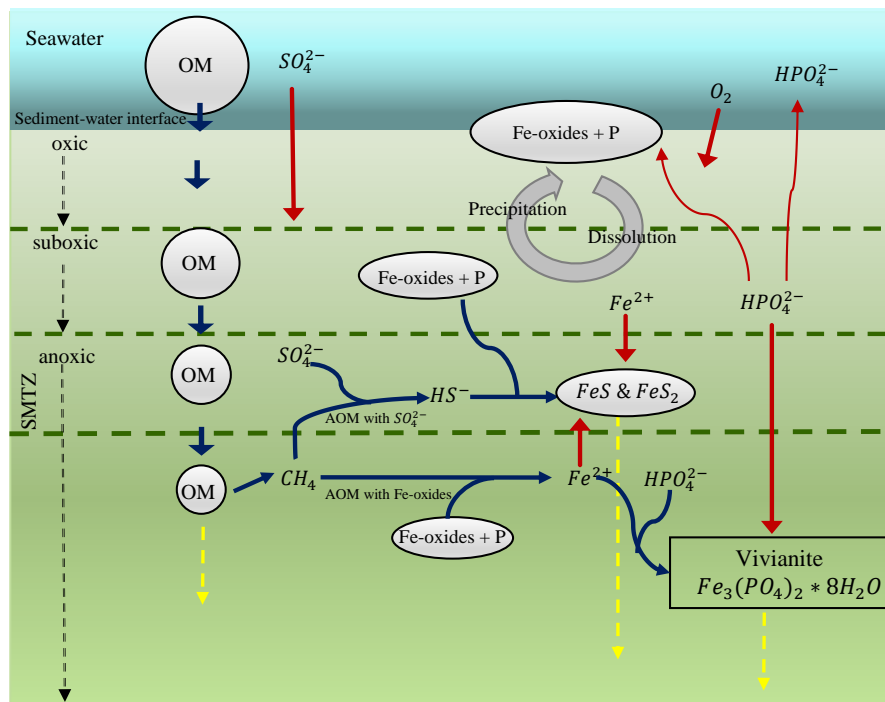


Figure 2: Schematic of the coupled Fe and HPO_4^{2-} cycles during early diagenesis in coastal sediments. The shallow position of the SMTZ results from eutrophication and low salinity, allowing potentially the preservation of Fe-oxides. Reduction of Fe-oxides leads to the release of Fe^{2+} at depth, creating favorable conditions for vivianite formation. Solid phases are bordered, blue arrows are fluxes from solid phases and/or reactions, red arrows indicate diffusion pathways, and yellow arrows indicate phases buried in the sediment. For simplicity, the removal of HPO_4^{2-} by the formation of other authigenic minerals (e.g. apatite) is not shown here. Apatite would lead to an uptake of calcium, fluoride and HPO_4^{2-} . Figure 2 is adapted from Ruttenger (2014) & Egger et al. (2015)

The most stable ferrous phosphate in the environment is vivianite (Nriagu, 1972). Vivianite is the Fe-rich end member of the vivianite mineral group ($M_3(XO_4)_2 \cdot 8H_2O$, where M can be a divalent cation such as Mg, Mn, Fe, Co, Ni, Cu, Zn and X is either P or As) (Rothe et al., 2016). The Mg-rich end member is called baricite. The theoretical ratio of Fe to P is low (1.5), making vivianite a very efficient phase for P burial. In comparison, the Fe to P ratio typical for P sorbed to Fe-oxides is ~ 10 (Slomp et al., 1996). Eutrophication may therefore lead to a positive feedback mechanism enhancing the P retention of coastal sediments. While the P burial in form of vivianite is known to be important in lacustrine systems (Rothe et al., 2014), the wider distribution of vivianite in brackish coastal systems besides the Bothnian Sea still remains to be explored (Egger et al., 2015). The potential role of vivianite in P burial has also been widely ignored in the past due to methodological limits. The commonly applied sequential extractions do not target the ferrous phosphate pool, making it challenging to identify the presence of vivianite (Li et al., 2015; Egger et al., 2015; Rothe et al., 2016).

1.2 Research questions

The goal of this thesis is to answer the following questions derived from the presented knowledge gaps:

- Is there evidence for authigenic ferrous phosphate formation in other brackish coastal systems than the Bothnian Sea?
- How is P permanently retained in methane-rich sediments in three eutrophic coastal sites and what role does ferrous phosphate play in P burial?
- Is a combination of traditional sequential extractions and spectroscopic techniques sufficient to identify the Fe-bound P pool accurately?

2 Materials and Methods

Study sites were chosen based on their potential to allow new insights into processes controlling P burial in eutrophic, methane-rich coastal sediments. In total, three sites were studied; two located in the Chesapeake Bay (CB2.2 & ET5.1), USA, while the third site (Strömmen) is situated in the inner Stockholm Archipelago (Baltic Sea). Both coastal systems have been well studied, are considered enriched in nutrients, have comparable sediment P concentrations, and seasonally experience hypoxia (Diaz and Rosenberg, 2008; Puttonen et al., 2014; Almroth-Rosell et al., 2016; Hartzell et al., 2017). Strömmen was selected as a study site, since two modeling studies identified the inner part of the Stockholm Archipelago as an efficient coastal nutrient filter (Almroth-Rosell et al., 2016; Karlsson et al., 2010). The sedimentary processes leading to this high P retention were not identified, making Strömmen an ideal study site to assess the importance of Fe-bound P as a permanent P sink in coastal areas.

Chesapeake Bay subestuaries are considered to be unusually efficient in P retention in comparison to other estuaries (Nixon et al., 1996). Hartzell et al. (2017) reported a strong coupling between P and Fe in the sediment of four subestuaries. The coupling was especially strong at oligohaline sites (<5) and is probably responsible for the high P burial. One of their study sites was ET5.1 (referred to as Choptank 1 in Hartzell et al. (2017)). Despite demonstrating a strong coupling, the authors were unable to reveal the nature of minerals responsible for efficient P burial. Lastly, CB2.2 was selected due to porewater profiles indicating a possible connection between P burial and Fe dynamics (S. Y. Malkin, personal communication).

Overall, the three sites share similarities in terms of proximity to land, nutrient status, and high CH₄ concentrations. At the same time, they spanned a range in salinity from 0.2 to 9.0, allowing an opportunity to investigate the interactive relationships between Fe, P, and S dynamics in determining the P burial. To determine in which form P is buried, different analytical methods were applied. From all three sites, sediment cores were retrieved, followed by porewater analyses, sequential solid phase extractions and visual identification of the mineral structure by scanned electron microscopy (SEM) coupled to an energy dispersive X-ray spectroscopy (EDS) and micro X-ray fluorescence spectrometer (μ XRF)- analyses. Thermodynamic saturation calculations were performed for the porewater, while the solid phase extraction data was used to quantify P burial and various ratios allowing insights into possible inorganic P forms. The applied methodology is discussed in depth in the following section.

2.1 Study sites

2.1.1 Chesapeake Bay

The Chesapeake Bay is the largest estuary in the United States with a surface area of 11,100 km², extending 300 km from the mouth of the Susquehanna River to the Atlantic Ocean with an average width of 20 km, and a mean water depth of 8 m (Gelesh et al., 2016). It is a partially stratified estuary, encompassing a watershed of 172,000 km² (Hagy et al., 2004). The Chesapeake Bay is considered to be highly eutrophic and seasonal deep-water hypoxia during the summer/fall has

been recorded since the 1950s (Kemp et al., 2005; Hagy et al., 2004; Testa and Kemp, 2014).

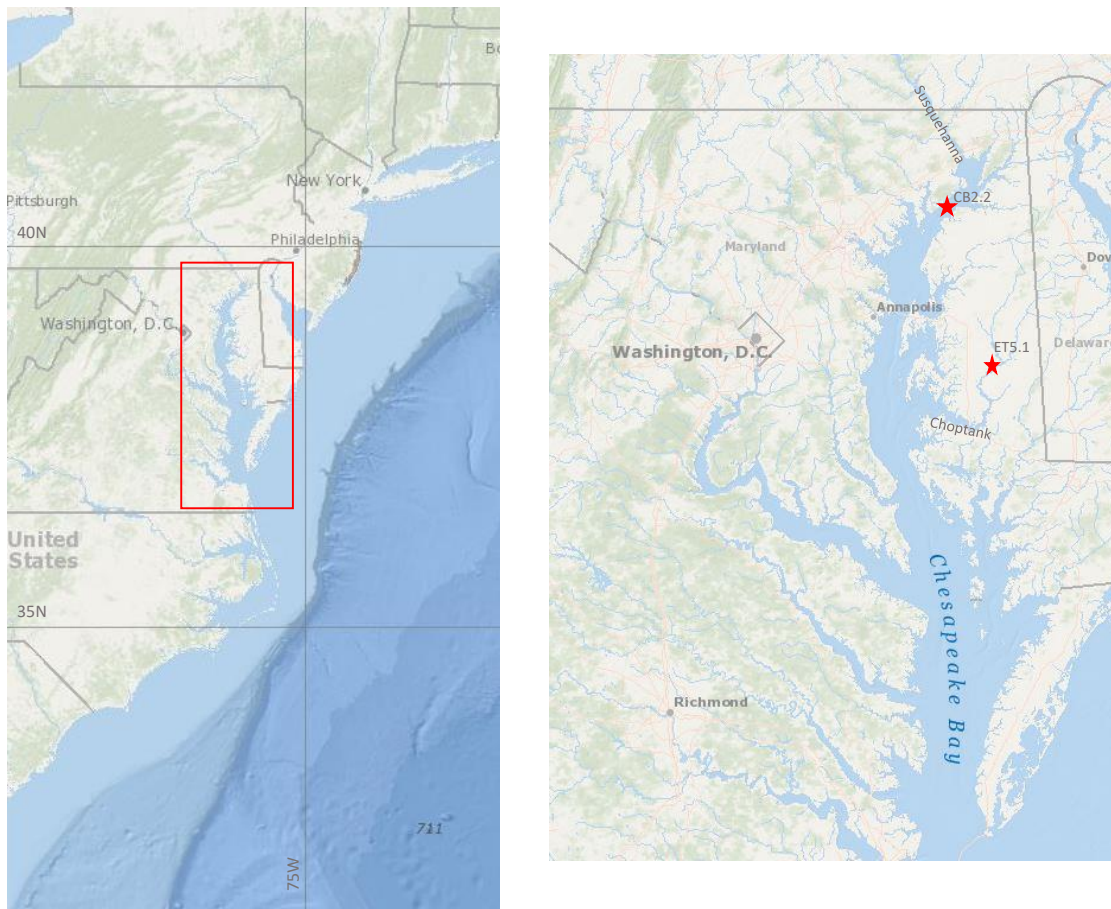


Figure 3: Study sites ET5.1 & CB2.2 in the Chesapeake Bay, USA. Maps from National Oceanic and Atmospheric Administration (Accessed April 2018)

Study site CB2.2 (nomenclature used from the Chesapeake Bay Program) is located in the main channel of the Chesapeake Bay, while ET5.1 is located in the upper Choptank River (see Figure 3). The Choptank River is the largest tributary of the eastern shore of the Chesapeake Bay with an estuarine surface area of 366 km². Generally, it is a well-mixed, shallow estuary. The physical characteristics of the Choptank River make it less vulnerable to hypoxic conditions (Staver et al., 1996; Fisher et al., 2006). The watershed is located in the coastal plain physiography and 66% of the watershed's area is used by agriculture (Hartzell et al., 2017; Staver et al., 1996). It is considered to be eutrophic for the last 50 to 100 years, and P inputs are 4 to 20 times higher than under forested conditions 350 years ago. Agricultural inputs dominate the total P loading of the Choptank River. Current efforts appear to be failing to improve significantly the water quality and trends indicate rising P loading (Fisher et al., 2006). Therefore, it is crucial to understand how the sediments of the Choptank River retain and efficiently bury P. Study site ET5.1 is situated downstream of the confluence of the Tuckahoe Creek into the Choptank River, located close to the fresh end member of the estuary. Based on long-term monitoring data (1984 to present) ET5.1 does not experience hypoxia and has usually a salinity range of 0 to 2. Bottom water salinity could be as high as 4 in fall. HPO_4^{2-} concentrations have increased since 1984. In summer, HPO_4^{2-} concentrations in bottom and surface water are generally 0.25 μM higher than in winter (Appendix G). Table 1 summarizes

general physical & chemical information of ET5.1 on the sampling day.

CB2.2 is located in the oligohaline part of the upper Chesapeake Bay. The site is approximately 30 km downstream of the Susquehanna River mouth (Helz et al., 1985). Subsequently, most of the freshwater, as well as suspended sediment, originates from the Susquehanna watershed. The tributary drains 72,000 km². Most of the watershed's area is forested, followed by agricultural usage (Ko and Baker, 2004; Hagy et al., 2004). The flow of the Susquehanna into the Chesapeake Bay is significantly impacted by three hydroelectric dams close to the Susquehanna river mouth. The Safe Harbor dam, the Holtwood dam and the Conowingo dam are located 53, 30, and 16 km upstream of the river's mouth. The Conowingo dam is one of the largest dams in the United States (Williams and Reed, 1972). Several studies reported that especially the sediment deposition of the upper bay, where CB2.2 is located, is altered by these dams and associated flooding events (Gross et al., 1978; Williams and Reed, 1972; Hirschberg and Schubel, 1979). Also, the nutrient loading to the Chesapeake Bay is significantly altered by the presence of the dams. Despite a reduction in nutrient loading in the upper part of the Susquehanna, an increase in particulate P discharge from the Conowingo dam to the Chesapeake Bay is reported since the mid 1990s, indicating that the system gradually loses its sediment storage capacity. It is expected that P loading to the upper Chesapeake Bay will increase in the future (Zhang et al., 2013). Consequently, it is important to gain information how efficient the P burial is in the upper Chesapeake Bay. Chesapeake Bay Program data reveals that oxic water conditions are generally persistent at CB2.2. Salinity ranges usually from 1 to 9 in the bottom water. Summer salinities are lower ranging from 1 to 4, while winter salinities have a higher range (Appendix G). Also at CB2.2, HPO₄²⁻ concentrations have increased since 1984. Bottom water and surface water HPO₄²⁻ concentrations are generally 0.5 μ M higher during summer/fall than during winter and spring.

CB2.2 was sampled with the *R/V Rachel Carson* and general conditions are provided in Table 1.

Table 1: Key characteristics of study sites on sampling day

Site	Coordinates	Sampling day	Water depth [m]	BW oxygen [μ mol/l]	O ₂ saturation [%]	pH	Temperature [°C]	Salinity
ET5.1	38°48.36'N 75°54.66'W	28.08.2017	4.0	162.5	64.9	7.06	27.0	0.2
CB2.2	39°20.92'N 76°10.59'W	04.09.2017	10.0	218.8	82.9	7.69	22.2	6.1
Strömmen	59°19.15'N 18°7.15'E	22.03.2017	30	339.1	79.3		1.5	5.2

2.1.2 Stockholm Archipelago

The third site, Strömmen, is located in the inner part of the brackish Stockholm Archipelago (Figure 4). The archipelago is the largest in Sweden and the second largest in the Baltic Sea. The river Norrström with an average discharge of about 160 m³ s⁻¹ feeds the archipelago with freshwater. About 2600 t of N and 120 t of P are transported annually by the river to the coastal

basin "Strömmen" in the inner archipelago. The largest point source of nutrients to the inner archipelago are several waste-water treatment facilities of Stockholm. Since the 1970s, the Stockholm Archipelago is classified as a highly eutrophic system (Almroth-Rosell et al., 2016). Despite a reduction in nutrient loading, Strömmen still experiences seasonal hypoxia based on long-term data (1965-present), provided by the Swedish National Oceanographic Data Center/SHARK at the Swedish Meteorological and Hydrological Institute (SMHI). Several islands form a natural boundary between the inner and intermediate Stockholm archipelago limiting the exchange of water, and consequently, enhancing the likelihood of seasonal hypoxia (Karlsson et al., 2010; Almroth-Rosell et al., 2016). For this study, Strömmen was sampled with the *R/V Electra* and general water properties of the sampling day are summarized in Table 1.

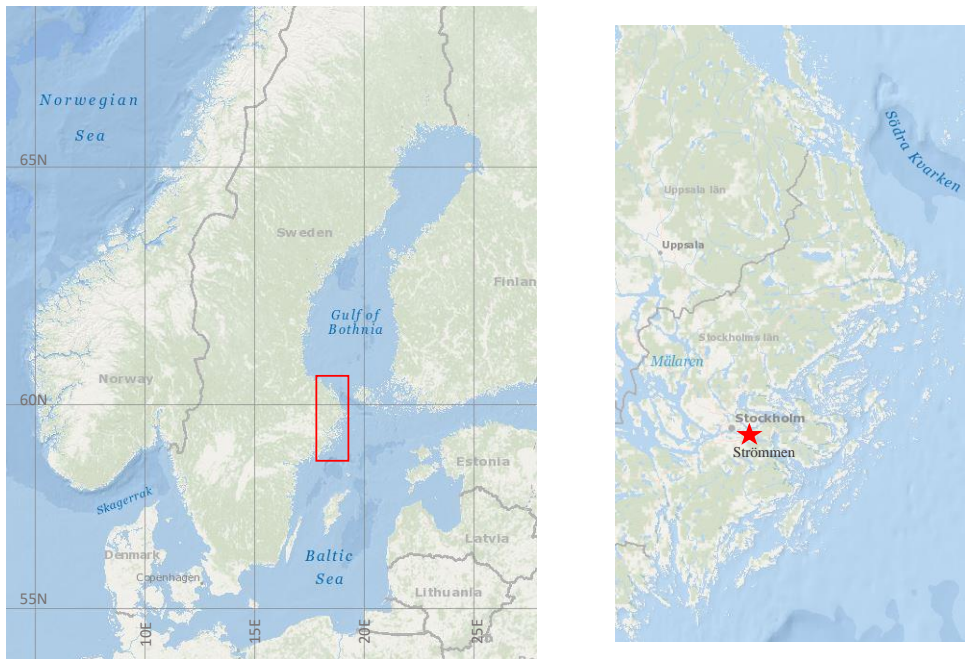


Figure 4: Location of study site Strömmen, Stockholm Archipelago, Sweden. Maps from National Oceanic and Atmospheric Administration (Accessed April 2018)

2.2 Sample collection

2.2.1 Chesapeake Bay

Oxygen concentration, salinity, and temperature of the bottom water were measured on deck with a conductivity/temperature probe and an oxygen probe at both sites. Coring at CB2.2 was performed from the *R/V Rachel Carson* (Maryland, USA) using a gravity corer (Model GC-150; Mooring Systems, Inc; Cataumet, MA). Core liners were made of cellulose acetate butyrate, with an inner diameter of 6.7 cm. Coring at ET5.1 was performed from a small vessel using a gravity corer (Uwitec, Austria; core catcher removed). Core liners with an inner diameter of 8.6 cm were made of clear PVC. Once retrieved, sediment cores were inspected for an undisturbed sediment-water interface and sufficient overlying water (>10 cm), only high quality cores were capped. Sediment

cores for anoxic porewater and solid-phase analyses, as well as ^{210}Pb dating and vivianite sieving were returned to the laboratory and sectioned within 24 hours. After processing the cores, the samples were stored at -20°C in N_2 -purged airtight aluminum bags.

2.2.2 Stockholm Archipelago

A CTD (conductivity, temperature and depth) system was used to measure the physical parameters at Strömmen. The oxygen concentration was measured by an oxygen probe. The sediment cores (at least 50 cm of sediment and 10 cm of overlying water) were recovered using GEMAX corer tubes with an inner diameter of 10 cm. Cores were taken for anoxic porewater and solid-phase analyses, CH_4 sampling, and oxic sampling (porosity). The cores were processed directly on deck after recovery. Processed sediment samples were stored -20°C in N_2 -purged airtight aluminum bags.

2.3 Porewater subsampling

The process to collect porewater and its analyses differs between Strömmen and the Chesapeake Bay sites. The Chesapeake Bay porewater cores (both sites) were processed in the laboratory under a N_2 atmosphere. Before slicing the core, bottom water was sampled with a syringe. Afterwards, the core was sliced with a 0.5 cm, 1 cm, and 2 cm resolution from 0-5 cm, 5-10 cm, and from 10 cm to the bottom of the core respectively. Each sediment interval was put into a 50 ml centrifuge tube. To separate the sediment from the porewater, the centrifuge tubes were centrifuged at 3000 rpm for 10 minutes. The supernatant was separated and filtered through a $0.2\ \mu\text{m}$ Target2 syringe filter into a clean HDPE vial from which subsamples were dispensed for subsequent analyses.

In the case of Strömmen, the core for porewater was sliced in a N_2 -filled glovebag. With a syringe, two bottom water samples were taken and the rest of the bottom water was discarded. The core was sliced at a 0.5 cm, 2 cm, and 4 cm resolution from 0-10 cm, 10-20 cm, and 20-40 cm sediment depth respectively. The 50 ml centrifuge tubes filled with sediments were centrifuged at 3500 rpm for 20 minutes to extract porewater. After centrifugation, the samples were brought back into a N_2 -filled glovebag. The porewater and bottom water samples were filtered through $0.45\ \mu\text{m}$ Teflon filters under a N_2 atmosphere. Table 5 provides an overview over the porewater sub-sampling processes and analyses.

Table 2: Sub-sampling and analyses of the porewater

	Variable	Pre-treatment	Volume of porewater [ml]	Method for analysis	Detection limit
Chesapeake Bay ¹ Strömmen	HS ⁻	Addition of 200 μ l of 20% zinc (Zn) acetate Addition of 2 ml of 2% Zn acetate	1 0.5	Spectrophotometrically (Cline, 1969)	3 μ M
Chesapeake Bay Strömmen	DIC ²	Crimped sealed vial, stored in the dark at 4°C, analyzed within 48 hours Poisoned with HgCl ₂ , stored at 4°C	1 5	Conversion to CO ₂ by addition of 0.5 N H ₂ SO ₄ , gas chromatography AS-C3 analyzer ³	
Chesapeake Bay Strömmen	Major cations ⁴	Addition of 10 μ l HNO ₃ to achieve pH less than 1 ⁵ 10 μ l 30% suprapure HCl per ml of sample	1 1-2 ml	ICP-OES ⁶	⁷
Chesapeake Bay Strömmen	NH ₄ ⁺	Stored at -20°C	2 1	Colorimetrically, indophenol blue method (Timothy et al., 1984) Colorimetrically at 630 nm (Helder and De Vries, 1979)	
Chesapeake Bay Strömmen	SO ₄ ²⁻ & Cl ⁻	Diluted 5-fold	0.5	Suppressed anion exchange chromatography ⁸ Ion chromatography	<75 μ mol l ⁻¹
Chesapeake Bay	Si	Storage -20°C, 10 or 50 fold dilution	2	Standard colorimetric method by segmented flow analyses	
Chesapeake Bay	HPO ₄ ²⁻		2	Colorimetrically using molybdate blue method (Strickland and Parsons, 1972)	

¹ Label Chesapeake Bay applies to both sites: CB2.2 & ET5.1.² Dissolved Inorganic Carbon³ AS-C3 analyzer (Apollo Sci-Tech), which consists of an acidification and purging unit in combination with a LICOR-7000 CO₂/H₂O Gas Analyzer.⁴ Major cations include Na⁺, Mn²⁺, Mg²⁺, Ca²⁺, K⁺, Fe²⁺, and for Strömmen as well the anions Si and HPO₄²⁻. The porewater concentration of dissolved Fe²⁺ (<0.45 μ M) is only an indication of the truly dissolved fraction, since this fraction consists most likely of a mixture of truly dissolved (ionic), organically complexed, colloidal and nanoparticulate Fe (Raiswell and Canfield, 2012).⁵ An internal Yttrium standard (1 ppm) was added to standards and samples to track performance. Accuracy and precision of the analyses were controlled by replicate measurements of reference standards.⁶ Inductively Coupled Plasma-Optical Emission Spectrometry (ICP-OES; Spectra Arcos)⁷ Detection limits are as followed: Ca²⁺ – 2.18 μ M; Fe²⁺ – 0.03 μ M; K⁺ – 0.6 μ M; Mg²⁺ – 8.7 μ M; Mn²⁺ – 0.01 μ M; Na⁺ – 33.12 μ M⁸ Dionex ICS-2000, Dionex AS11-HC column

2.3.1 Methane sampling & analysis

Chesapeake Bay

CH₄ was sampled directly after core recovery from pre-drilled holes in the core liners with a 2 cm resolution for CB2.2 and 2.5 cm for ET5.1. Using a cut-off syringe, 3 ml of sediment sample was collected through the pre-drilled holes. Sediment was transferred immediately to 40 ml serum vials, preserved with 6 ml of 2.5 % NaOH, crimped sealed, shaken vigorously, and stored upside-down at -20°C until analysis. CH₄ concentrations were analyzed by GC-FID and $\delta^{13}\text{C-CH}_4$ was measured by cavity ring-down spectroscopy, using certified reference standards (CRDS; Picarro, in the lab of Laura Lapham, UMCES). The calculated CH₄ concentrations were corrected for porosity.

Stockholm Archipelago

The GEMAX tube that was used to collect the core for CH₄ sampling, had taped pre-drilled holes at a 2.5 cm depth-spacing. CH₄ was sampled directly after core recovery on board. Exactly 10 ml of a sediment sample was taken with cutoff syringes from each hole and immediately transferred to a 65 ml glass bottle filled with saturated NaCl solution. The bottles were stoppered, capped, and stored upside down until further analyses.

Prior to CH₄ measurements, a 10 ml N₂ headspace was injected into the bottle. Subsequently, the CH₄ concentrations in the headspace were determined by the injection of 50 to 200 μl of subsample into a Thermo Finnigan Trace GC gas chromatograph (Flame Ionization Detector). The calculated CH₄ concentrations were corrected for porosity.

2.4 Solid-phase analyses

The solid-phase analyses was the same for the three study sites. Sediments were freeze-dried and ground in an agate mortar in an argon (Ar) atmosphere. Oxic and anoxic splits were made for different analyses.

To avoid any oxidation artifacts in the P, Fe, and S sequential extractions, anoxic sediment splits were used. Additionally, the first step of all extractions was performed inside an Ar-purged glovebox, while the other steps were carried out under a N₂-gas line (Kraal et al., 2009; Kraal and Slomp, 2014).

2.4.1 Total elemental composition and organic carbon

Sediment subsamples of the oxic splits (~ 0.125 g) were digested overnight at 90 °C in a mixture of 2.5 ml of HClO₄ and HNO₃ (ratio 3:2) and 2.5 ml HF in a Teflon vessel. Afterwards, the acids were evaporated at 140 °C until a gel was formed. Subsequently, this gel was dissolved in 25 ml of 4.5 % HNO₃ at 90 °C overnight. With the ICP-OES total elemental concentrations of Al, Ca, Fe, Mn, Mg, P, and S in 4.5 % HNO₃ were determined, from which total elemental concentrations in the sediment samples were calculated. The total Ca concentration was used to calculate the maximum possible CaCO₃ concentration. Based on duplicates the general percentage error was less than 3 %.

Furthermore, other subsamples of the oxic split (~ 0.3 g) were decalcified by two washes with 1 M HCl (4 and 12 hours, respectively) and a final rinse with UHQ water (Van Santvoort et al., 2002). Subsequently, the decalcified samples were dried at 50°C and analyzed with CN analyzer (Fisons Instruments Na 1500) to determine organic carbon content. Based on laboratory reference materials, the relative error was generally less than 3 %.

2.4.2 Porosity and Grain Size

Chesapeake Bay

Sediment samples were prepared for grain size analyses by disaggregation in a sodium metaphosphate solution and gentle sonication. Samples were wet-sieved (64 μm) to separate the mud from sand fractions, and the grain size distribution of the mud fraction was measured by X-ray sedimentation (Micromeritics Sedigraph 5100). Porosity was determined from water loss upon drying at 60°C until a constant weight was reached and assuming a dry sediment density of 2.65 g cm^{-3} .

Strömmen

Porosity was determined by freeze-drying an oxic split of the bulk sediments' intervals and assuming as well a dry sediment density of 2.65 g cm^{-3} . In case of Strömmen, no grain size distribution was determined.

2.4.3 ^{210}Pb dating

Chesapeake Bay

For determination of ^{210}Pb activity, the activity of its granddaughter isotope, ^{210}Po , was measured by alpha-spectrometry (Canberra Alpha Analyst), following Palinkas and Nittrouer (2007). Approximately 3 g of dry sediment samples were spiked with a known quantity of reactor-produced ^{209}Po and digested in concentrated HNO_3 and HCl. ^{209}Po and ^{210}Po were subsequently electroplated onto silver planchets and their activity was counted for 24 hr and decay-corrected to the time of sample collection. Since ^{210}Pb preferentially adsorbs to fine particles (Goodbred Jr and Kuehl, 1998), the effect of grain-size variations was corrected by normalizing the activity to the corresponding mud (silt+clay).

Rates of sediment deposition were estimated by applying a constant flux/constant sedimentation model (Appleby and Oldfield, 1978), and accounting for mixing in the upper sediment layer. ^{226}Ra -supported activity was assumed to be equal to the activity at the bottom of CB2.2's core, where low uniform activities prevail. The distribution of excess ^{210}Pb below the mixing zone was modeled as:

$$A(z) = A(o)\exp[-(\lambda/S)z] \quad (1)$$

where $A(z)$ is the excess activity at depth z , $A(o)$ is the excess activity at the top of the mixing zone, S is the sedimentation rate, and λ is the ^{210}Pb radioactive decay constant (0.031 yr^{-1}). In the CFCS model, $S = -\lambda/m$ where m is the slope of the line fitted by linear regression to the decrease in the natural log of excess ^{210}Pb activity against z . Depth-integrated inventories were calculated using

the corresponding sediment porosity.

No sediment dating of Strömmen is available, yet.

2.4.4 Sulfur extraction

To distinguish between two different S fractions, the sequential S extraction developed by Burton et al. (2008, 2011) was applied to ~ 50 mg of freeze-dried, anoxic sediment subsamples. In the first step, acid volatile sulfide (AVS) was dissolved in a 6 M HCl/0.1 M ascorbic acid solution overnight. The released HS^- was trapped into a 10 ml vial filled with 7 ml Zn-acetate (20% Zn-acetate/2 M NaOH). Secondly, elemental S was dissolved in 25 ml of methanol overnight. Afterwards, chromium reducible sulfur (CRS) was extracted for 48 hours with an acidic chromium solution. The released HS^- was trapped in the same way as during step 1. The trapped HS^- concentrations were determined by iodometric titration (APHA, 2005). AVS is assumed to represent the FeS pool, while the CRS fraction represents FeS_2 . The relative standard deviation is generally below 6% and 7% for AVS and CRS respectively based on replicates.

2.4.5 Iron sequential extraction

The Fe sequential extraction was applied to an anoxic, freeze-dried sub-sample of ~ 50 mg. The method applied is a combination of Poulton and Canfield (2005) & Claff et al. (2010) as presented in Kraal et al. (2017). Table 3 provides an overview of the extraction steps.

All total Fe concentrations were determined with the colorimetric phenanthroline method, adding hydroxylamine-hydrochloride as a reducing agent to convert all ferric iron into Fe^{2+} (APHA, 2005). Only for Step 1 the absorbance before and after adding the reducing agent were measured, to assess the concentrations of Fe^{2+} and ferric iron. The ferric iron concentration was calculated as the difference between total Fe and Fe^{2+} . The sum of the extracted Fe phases is named highly reactive Fe (Fe_{HR}). This pool represents the Fe that has already reacted with HS^- or is likely to do so on geologically short timescales (Berner, 1970; Canfield et al., 1992; Raiswell and Canfield, 1998). The Fe_{HR} was calculated twice, once applying the pyrite concentration determined via the Fe-extraction and a second time using the CRS concentration of the S-extraction. The poorly reactive Fe pool (mainly clay minerals) is determined by subtracting Fe_{HR} from the total Fe pool measured by total digestion (Section 2.4.1).

2.4.6 Phosphorus extraction

Applying the SEDEX method developed by Ruttenberg (1992), and modified by Slomp et al. (1996) including the exchangeable P step, the P fractions of ~ 100 mg of ground anoxic sediment subsamples were investigated. Table 4 shows an overview of the five sequential extraction steps. All P concentrations were determined colorimetrically by the molybdenum blue method (Strickland and Parsons, 1972). Only the P concentration in the citrate-dithionite-bicarbonate (CDB) solution was measured by the ICP-OES.

Table 3: Solvents and targeted Fe phases of the Fe sequential extraction procedure, as presented by Kraal et al. (2017)

Step	Extractant (extraction time)	Target phase	Term	Reference	Standard error based on duplicates [%]
1	1 M HCl, pH 0, (4 h)	Poorly ordered/ pH sensitive Fe(II) and Fe(III) minerals, such as ferrihydrite, Fe- carbonate and monosulfides	HCl-Fe(II) and HCl-Fe(III) ¹	Claff et al. (2010)	14
2	0.35 M acetic acid/ 0.2 M Na ₃ -citrate/ 50 g l ⁻¹ Na dithionite, pH 4.8 (4h)	Crystalline oxide minerals (goethite, hematite)	CDB-Fe ¹ ;	Poulton and Canfield (2005) Claff et al. (2010)	3
3	0.17 M NH ₄ oxalate/ 0.2 M oxalic acid, pH 3.2 (6h)	Recalcitrant oxide minerals (magnetite) ²	oxalate-Fe;	Poulton and Canfield (2005)	9
4	65% HNO ₃ (2h)	Pyrite	HNO ₃ -Fe	Claff et al. (2010)	7

¹ The sum of the HCl-Fe(III) and CDB-Fe represents the Fe-oxide pool.

² This represents probably the magnetite fraction most recalcitrant due to an expected partial dissolution of magnetite in 1 M HCl (Poulton and Canfield, 2005) and CDB-solution (Claff et al., 2010).

Table 4: Solvents, targeted phases and abbreviations of the SEDEX (Ruttenberg, 1992), including the alterations by Slomp et al. (1996).

Step	Extractant	Time	Target phase	Abbreviation	Standard error based on duplicates [%]
1	1 M MgCl ₂ (pH 8)	0.5 h	Exchangeable P	Ex-P	7
2 _a	0.3 M Na ₃ citrate / 25 $\frac{g}{l}$ Na diathionite / 1 M NaHCO ₃ (pH 7.6)	8 h	Fe-bound P	CDB-P ^{1,2}	8
2 _b	1 M MgCl ₂ (pH 8)	0.5 h	Washing step		
3 _a	1 M Na acetate buffered to pH 4 with acetic acid	6 h	Authigenic P	Authi Ca-P	10
3 _b	1 M MgCl ₂ (pH 8)	0.5 h	Washing step		
4	1 M HCl	24 h	Detrital apatite	Detr-P	5
5	Combustion at 550 °C 1 M HCl	2 h 24 h	Organic P	Org-P	10

¹ Since the CDB-solution likely extracts not only the Fe-P phase, it is referred to as CDB-P.

² Ferrous phosphates such as vivianite are also likely to be dissolved in the CDB solution, as shown by (Dijkstra et al., 2016) and (Nembrini et al., 1983).

2.5 Identification of Fe(II)-phosphates

Porewater profiles and sequential extractions only provide indirect evidence regarding certain forms of P burial such, as the presence of ferrous phosphates (e.g. Dijkstra et al., 2016). Therefore,

intervals of all sites were further investigated for visual detection of mineral phases by SEM and μ XRF.

2.5.1 Scanning electron microscopy (SEM)

Wet bulk sediments of three different depths (shallow, intermediate and deep) of the study sites (Table 5) were sieved through a 38 μ m sieve with oxygen-free UHQ water. Sediment intervals were chosen to capture different features in Fe-P-S interactions as revealed by the solid phase analyses and porewater data. For instance, the shallow sediment intervals are located directly below the SMTZ. The samples were sieved to remove small particles such as clays and hence to

Table 5: Investigated depth intervals by the SEM of study sites

	Strömmen	ET5.1	CB2.2
Depth 1 (cm)	3.5 -4	5-6	6-7
Depth 2 (cm)	14-16	10-12	22-24
Depth 3 (cm)	28-32	32-34	44-46

enrich the sediment in mineral phases important for P burial. Furthermore, to remove organics attached to the minerals the samples were washed with deoxygenated UHQ water multiple times for 4 minutes in a sonic bath until the supernatant was clear. In case of ET5.1 and CB2.2, five washes were required, while the samples from Strömmen were washed 25 times due to the presence of oil-like contamination. Afterwards, the samples were dried in an Ar-filled glovebox at room temperature. Aliquots of the sieved and dried samples were put on an aluminum sample holder using double-sided carbon tape. Subsequently, the samples were carbon coated. The SEM-energy dispersive X-ray spectroscopy (EDS; JCM 6000PLUS NeoScope Benchtop SEM) with 15 kV accelerating voltage, Si/Li detector in backscatter mode imaging (BEI) was used to analyze the samples. To quantify the elemental composition of certain particles, EDS analysis was carried out in the 0-20 keV energy range (probe current: 1 nA, acquisition time: 50 s (live time)), allowing to determine the relative molar ratios of major elements.

2.5.2 μ XRF mapping

Due to difficulties identifying the nature of Fe-rich particles from Strömmen, certain sediment-intervals of interest were further investigated with the Desktop μ XRF. In total three sediment intervals from 20-24 cm, 28-32 cm, and 32-36 cm were analyzed. To investigate the Fe-P-Mn interactions at ET5.1 further, one sediment interval (10-12 cm) was analyzed. For the analyses, freeze-dried, ground, anoxic aliquots were mounted on double-sided carbon tape. Elemental maps of the aliquots were then collected using a Desktop EDAX Orbis μ XRF analyzer (Rh tube at 30 kV, 500 μ A, no filter, 300 ms dwell time, poly-capillary lens providing a 30 μ m spot size).

2.6 Data processing

2.6.1 Calculations based on solid phase analyses

Degree of pyritization

In order to quantify how much of the Fe_{HR} is scavenged by S at depth, the degree of pyritization (DOP) was determined. Defined as:

$$DOP = \text{pyrite} / Fe_{HR} \quad (2)$$

The equation is slightly modified from the formulation proposed in the literature where:

$DOP = \text{pyrite} / (\text{pyrite-Fe} + \text{acid-soluble Fe})$ (Berner, 1970; Raiswell et al., 1988).

A modification was applied since the authors determined their reactive Fe pool differently. As the pyrite pool was determined via two methods, the DOP was calculated for both pyrite concentrations (determined via Fe- and S-extraction).

SEDEX ratio

The mineralogy of the CDB fraction was used to estimate the feasibility of vivianite formation. Theoretically, the ratio of Fe to P in vivianite is 3 to 2. A ratio greater than 1.5 in the CDB extracts is an indication that the extracted P could be bound in the form of vivianite. In such cases, these sediments were further explored, to analyze the enrichment of Mn in vivianite. The calculations were repeated, assuming again a ratio of 3 to 2 for Mn to P.

Total S/reactive-Fe

Rothe et al. (2015) hypothesized that the ratio of total S to reactive Fe provides an indication of possible vivianite formation. They observed that vivianite is only present in systems where the ratio is below 1.5 (stricter limit of 1.1). In such systems, sufficient Fe is available to potentially react with P. Here the reactive Fe is defined as total Fe of Step 2 and ferric iron of Step 1 of the Fe-extraction, as these are the Fe phases likely to react with P.

Total P burial

To investigate the efficiency of the coastal sites to retain P, total P burial rates were calculated (reported in $g\ P\ m^{-2}\ y^{-1}$). Normally, the total P concentration (determined via total digestion) stabilizes with depth (called stabilization depth, see Rydin et al. (2011) for more information). To calculate the permanent P burial rate, the average P concentration below the stabilization depth is used. Therefore, the total P burial rate was calculated by multiplying the average P concentration by the sediment accumulation rate and solid-phase volume.

2.6.2 Saturation calculations

Porewater data was used to calculate the saturation state of vivianite, hydroxylapatite, struvite and MnHPO_4 . These minerals might be significant inorganic phases with which P is removed from the porewater and permanently buried. The saturation indices were calculated by Visual MINTEQ using following equilibrium constants: $10^{-37.76}$, $10^{-44.33}$, $10^{-13.26}$, and $10^{-25.4}$ for the mineral forms respectively. These constants were corrected for bottom water temperature. It is worthwhile to consider that saturation indices only show that certain minerals are over/under-saturated thermodynamically in the system. These indices do not provide any evidence that the specific mineral form precipitates out due to supersaturation since possible precipitation is not solely controlled by thermodynamics (Rothe et al., 2016).

3 Results

3.1 General characteristics

Strömmen had the highest organic carbon content ranging from 7 to 10 wt% among the three study sites (Figure 5). Porosity did not show a clear pattern, but was generally above $0.9 \text{ cm}^3 \text{ cm}^{-3}$. The CaCO_3 concentration was low for all study sites ($<1 \text{ wt } \%$).

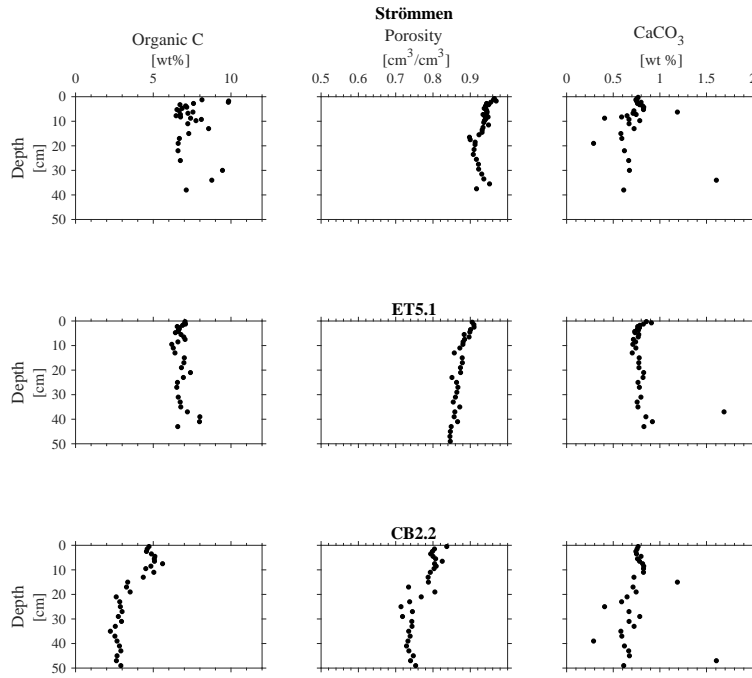


Figure 5: Depth profiles of organic carbon, porosity and CaCO_3

At ET5.1, sedimentation appeared to be relatively constant over time, resulting in a near-linear decline in porosity associated with sediment compaction, and a relatively constant organic carbon content ranging between 6 and 8 wt% (Figure 5). The ^{210}Pb activity declined with depth and the mud/sand distribution was relatively constant. The sand fraction increased slightly with depth, but the change was gradual (Appendix A). Based on the excess ^{210}Pb activity a sedimentation rate of 0.49 cm yr^{-1} and a sediment accumulation rate of $0.62 \text{ g cm}^{-2} \text{ yr}^{-1}$ was derived (see Section 2.4.3).

Organic carbon was generally below 5 wt% at CB22. Below 20 cm the organic carbon content stabilized and was approximately 2.5 wt% (Figure 5). Overall, porosity declined nearly linearly with depth, reflecting sediment compaction. However, between 20 and 30 cm sediment depth, the porosity varied and did not have a distinct trend (Figure 5). The variation in porosity matches an enrichment in sand to above 20 % between 15 to 20 cm (Figure 6). Otherwise, the distribution of sand to mud fraction was relatively constant. The ^{210}Pb activity in the upper 20 cm ranged from 4

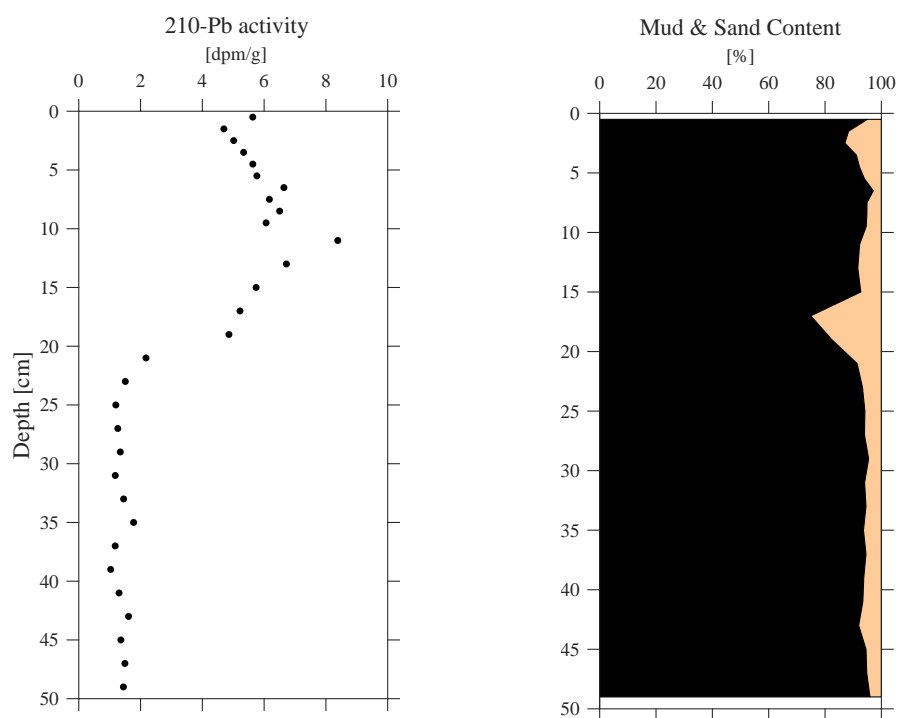


Figure 6: ^{210}Pb depth profile and sedimentary composition at CB2.2; the mud fraction is presented in black and the sand fraction in orange

to 8 ppm, while below 20 cm, background levels of approximately 1 ppm were present. Within the surface layer, peak values were reached at 11 cm (Figure 6). Using excess ^{210}Pb activity from 11 to 20 cm a sedimentation rate of 0.45 cm yr^{-1} and a sediment accumulation rate of $0.62 \text{ g cm}^{-2} \text{ yr}^{-1}$ were derived.

3.2 Porewater profiles

Porewater species are presented in Figure 7. Each species is plotted on the same scale for all three sites. Some trends, especially for Strömmen, become less visible since concentrations are a 10th of ET5.1's concentrations. Therefore, zoomed-in porewater profiles for some species of Strömmen are added in Appendix B.

At Strömmen, SO_4^{2-} concentrations declined rapidly from 4.2 mM in the bottom water to below detection limits at 8 cm. CH_4 concentrations increased with depth from $2 \mu\text{M}$ in the bottom water to $\sim 2860 \mu\text{M}$ at 29 cm depth. Strömmen is the only site where HS^- was detectable in the upper 20 cm with a maximum concentration of $457 \mu\text{M}$ at 3.75 cm depth. While HS^- was present, Fe^{2+} concentrations remained low ($<10 \mu\text{M}$) in the porewater. With a depletion in HS^- , ferrous iron concentrations increased up to $50 \mu\text{M}$. The entire sediment core contains Mn^{2+} (15 to $30 \mu\text{M}$).

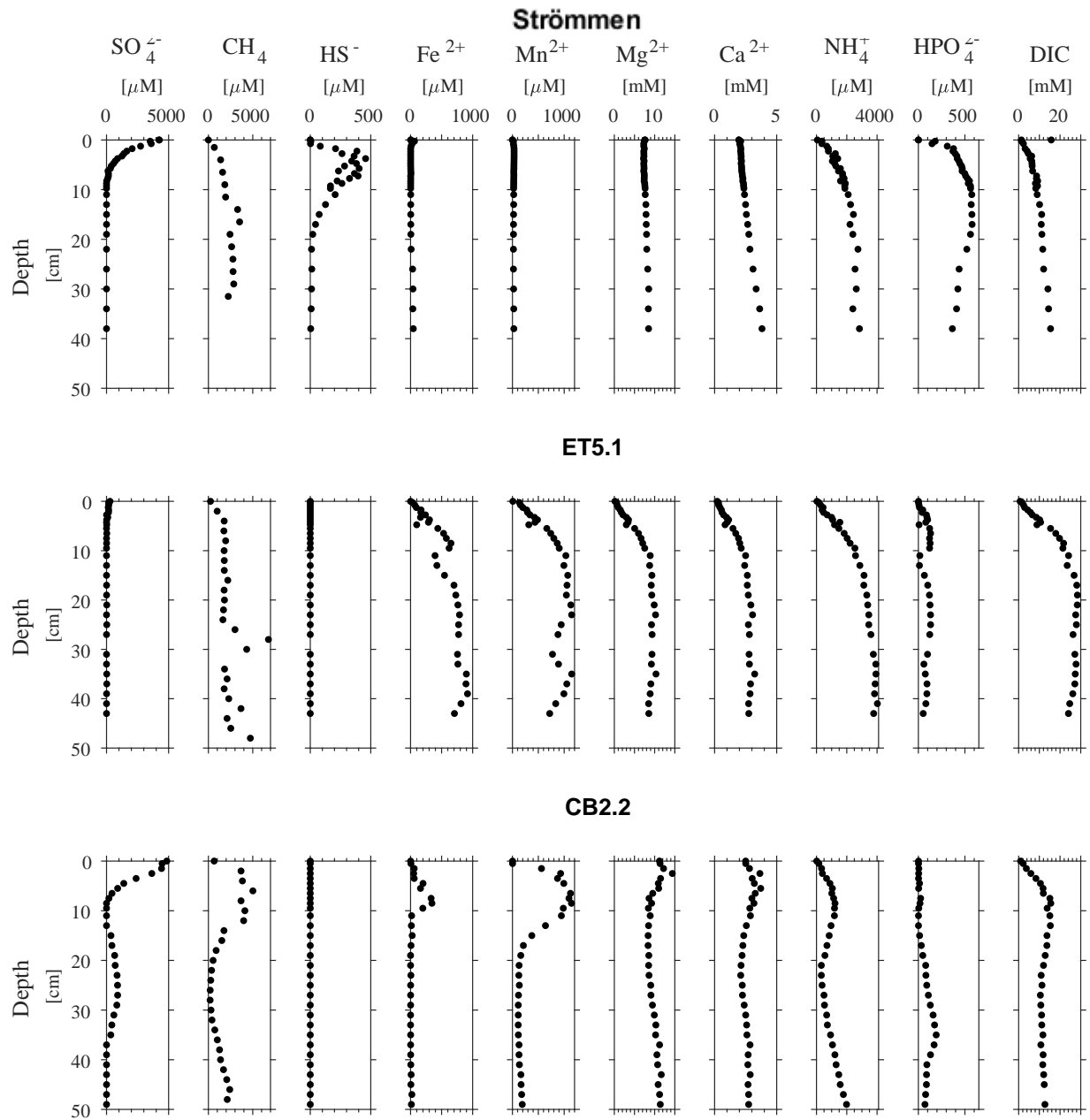


Figure 7: Porewater profiles (from left to right: methane, sulphate, ferrous iron, phosphate, manganese, ammonium, DIC, and magnesium) of Strömmen (top), ET5.1 (middle) and CB2.2 (bottom)

Ammonium (NH_4^+), DIC and HPO_4^{2-} increased exponentially with depth. In contrast to DIC and NH_4^+ , HPO_4^{2-} concentrations declined from 598 μM to 438 μM between 19 and 38 cm, coinciding with increases in Fe^{2+} and Mn^{2+} . The saturation calculations based on the porewater data showed supersaturation for MnHPO_4 and hydroxylapatite for all sediment intervals, while vivianite was only supersaturated below 22 cm (Appendix, Table 6). Struvite was for all sediment intervals undersaturated.

At ET5.1, the bottom water SO_4^{2-} concentration was the lowest of all three sites with 0.279 mM. Below 4.25 cm depth, SO_4^{2-} became negligible. All other porewater species except HPO_4^{2-} increased exponentially with depth. DIC and NH_4^+ concentrations were about twice as much as the ones detected at Strömmen (maximum 28 mM and 4 mM respectively), while Fe^{2+} and Mn^{2+} concentrations are ten times higher. Initially, HPO_4^{2-} increased. Concentrations were mostly between 50 and 130 μM , except at 4.75, 11 and 30 cm, where concentrations dropped suddenly to below 20 μM . These minima correlated to minima in Fe^{2+} and Mn^{2+} , indicating a potential coupling between these species. Vivianite and MnHPO_4 were supersaturated for all sediment intervals (Appendix, Table 6). Hydroxylapatite was supersaturated below 0.75 cm depth, while struvite was undersaturated through the whole sediment core.

The porewater profiles at CB2.2 show signs of lateral porewater advection, resulting in porewater profiles contrasting strongly to the other two sites. SO_4^{2-} concentrations declined rapidly from 4.85 mM, reaching detection limits by 8.5 cm depth. In the upper 10 cm, CH_4 , NH_4^+ , DIC, Fe^{2+} , Mn^{2+} and Ca^{2+} steadily increased, while HPO_4^{2-} concentrations did not show any increasing trend and remained low (<25 μM). Below 15 cm, however, SO_4^{2-} concentrations started to increase again, reaching its maximum of 0.9 mM for this part of the sediment at 25 cm depth. In contrast, CH_4 , DIC, Mg^{2+} , and NH_4^+ concentrations declined between 10 and 25 cm, and only increased below 25 cm depth. While the first 15 cm of CB2.2 were enriched in Mn^{2+} (maximum concentration of 1220 μM), the rest of the sediment had low concentrations ranging from 100 to 200 μM . Furthermore, Fe^{2+} concentrations remained low below 10 cm with a maximum concentration of 20 μM . Phosphate concentrations increased linearly below 20 cm, reaching its maximum concentration at 35 cm with 191 μM , followed by a decline to approximately 80 μM below 40 cm. The decline in HPO_4^{2-} corresponded to the depth of SO_4^{2-} depletion. No obvious link between Fe^{2+} , Mn^{2+} and HPO_4^{2-} was visible at CB2.2 in comparison to the other two sites. Hydroxylapatite and MnHPO_4 were supersaturated through whole sediment core, while vivianite was only supersaturated between 2.5 and 9.5 cm (Appendix B, Table 8), coinciding with high Fe^{2+} and low HPO_4^{2-} concentrations in the porewater.

3.3 Solid phase profiles

Strömmen had the highest total S and Fe content among the three stations with concentrations between 500 and 1300 $\mu\text{mol/g}$ and between 800 and 1100 $\mu\text{mol/g}$ respectively (Figure 8). A compositional change was observed below 30 cm. This was indicated by a change in Fe/Al and

S/Al ratios (Appendix C) and as an enrichment in total S and Fe (Figure 8). Total P was strongly enriched in the upper 2 cm (to 161 μM), stabilizing to an average of 40 $\mu\text{mol/g}$ below. Strömmen had the lowest total Mn concentration of the three study sites at around 10 $\mu\text{mol/g}$ and the highest total Mg concentration (400 to 500 $\mu\text{mol/g}$).

All total elemental concentrations were relatively stable with depth at ET5.1. Total S was low with concentrations below 140 $\mu\text{mol/g}$, and total Fe was around 750 $\mu\text{mol/g}$. The total P concentration was ~ 50 $\mu\text{mol/g}$ and the highest concentration among the three study sites. ET5.1 had the highest total Mn concentration, exceeding 60 $\mu\text{mol/g}$ at most depths. Concentrations were around 250 $\mu\text{mol/g}$ for Mg.

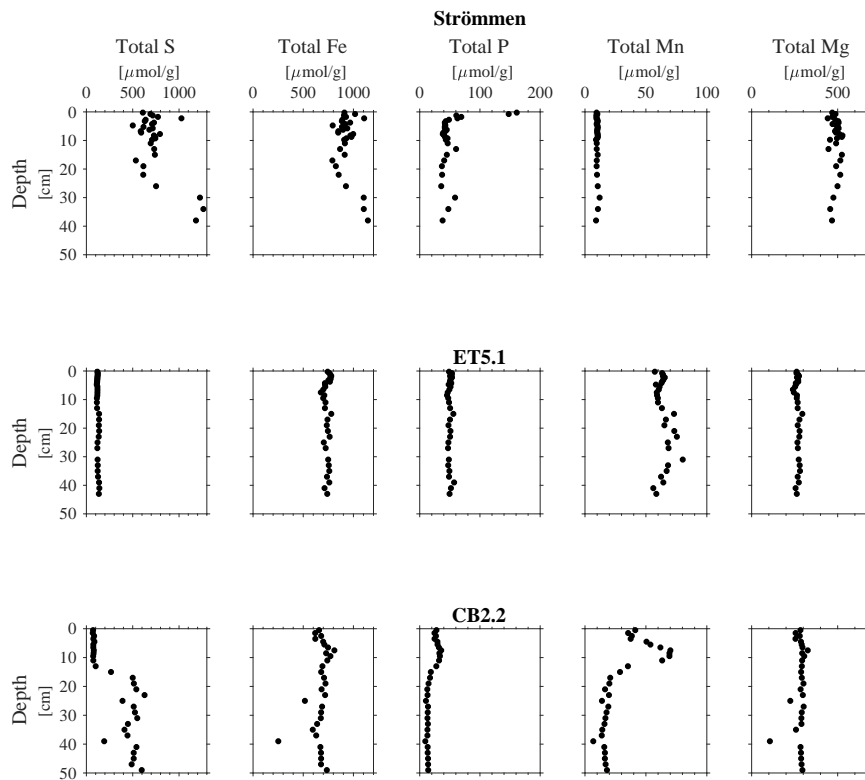


Figure 8: Depth profiles of total S, Fe, P, Mn, and Mg concentrations at the three study sites

Total Mn and total S had a distinct pattern at CB2.2. The upper 13 cm of sediment was depleted in S with concentrations below 100 $\mu\text{mol/g}$, while below 13 cm concentrations were within the order of 500 $\mu\text{mol/g}$. In contrast, total Mn was enriched in the upper 11 cm with concentrations between 35 to 70 $\mu\text{mol/g}$, whereas in the deeper sediment total Mn concentrations did not exceed 20 $\mu\text{mol/g}$. Total P concentrations showed a similar pattern to Mn. In the upper 13 cm, concentrations ranged from 24 to 35 $\mu\text{mol/g}$, while the deeper sediment was depleted in P with concentrations generally below 15 $\mu\text{mol/g}$. Total concentrations of Mg and Fe were comparable to ET5.1.

Calculated P burial rates can be found in the Appendix D.

In case of the Fe-extraction, the sum of the HCl-Fe(III) (Step1) and CDB-Fe (Step 2) is collectively referred to as the Fe-oxide pool. The difference between the total Fe concentration determined via total digestion and the total Fe concentration based on the Fe-extraction/S-extraction represents the unreactive Fe pool such as clays. At all three sites, $\sim 40\%$ of the total Fe was unreactive.

Strömmen did not have a distinct pattern with regard to its Fe-oxide pool. On average, 20% ($120\mu\text{mol/g}$) of the reactive Fe was bound in the form of Fe-oxides. Pyrite was percentage wise the largest fraction of the reactive-Fe pool, while magnetite was the smallest (Figure 9). Pyrite concentrations increased with depth (~ 90 to $500\mu\text{mol/g}$). The difference in pyrite determined by the two different methods increased also with depth. The difference between the variation in the pyrite pool was also revealed by DOP (Figure 10). Strömmen had a high DOP value increasing with depth (from 20 to 50 % and from 33 to 66% using the pyrite of the Fe-extraction and S-extraction respectively).

The majority of reactive Fe (on average 54%, $\sim 250\mu\text{mol/g}$) was bound in the form of Fe-oxides at ET5.1. The DOP value was very low with approximately 10% (Figure 10) in the entire sediment core. In addition, there was no significant difference between the DOP derived based on Fe-extraction and S-extraction. No AVS was detectable at ET5.1.

At CB2.2, a change in all Fe pools was detectable at 15 cm depth. The upper 13 cm were characterized by high Fe-oxide concentrations ($\sim 220\mu\text{mol/g}$) and low concentrations of pyrite and a low DOP value (lower than 15%, $<50\mu\text{mol/g}$). At a depth of 13 to 15 cm, the DOP jumped to over 40%. Below 15 cm, the DOP stabilized (60% based on Fe-extraction, 70% based on S-extraction), which was comparable to Strömmen's DOP values. The difference between the two pyrite pools also increased at CB2.2 coinciding with increasing total S concentrations with depth. Consequently, most of the reactive Fe was bound to S at depth, while the majority of Fe was present as Fe (II) or Fe-oxides in the upper 15 cm.

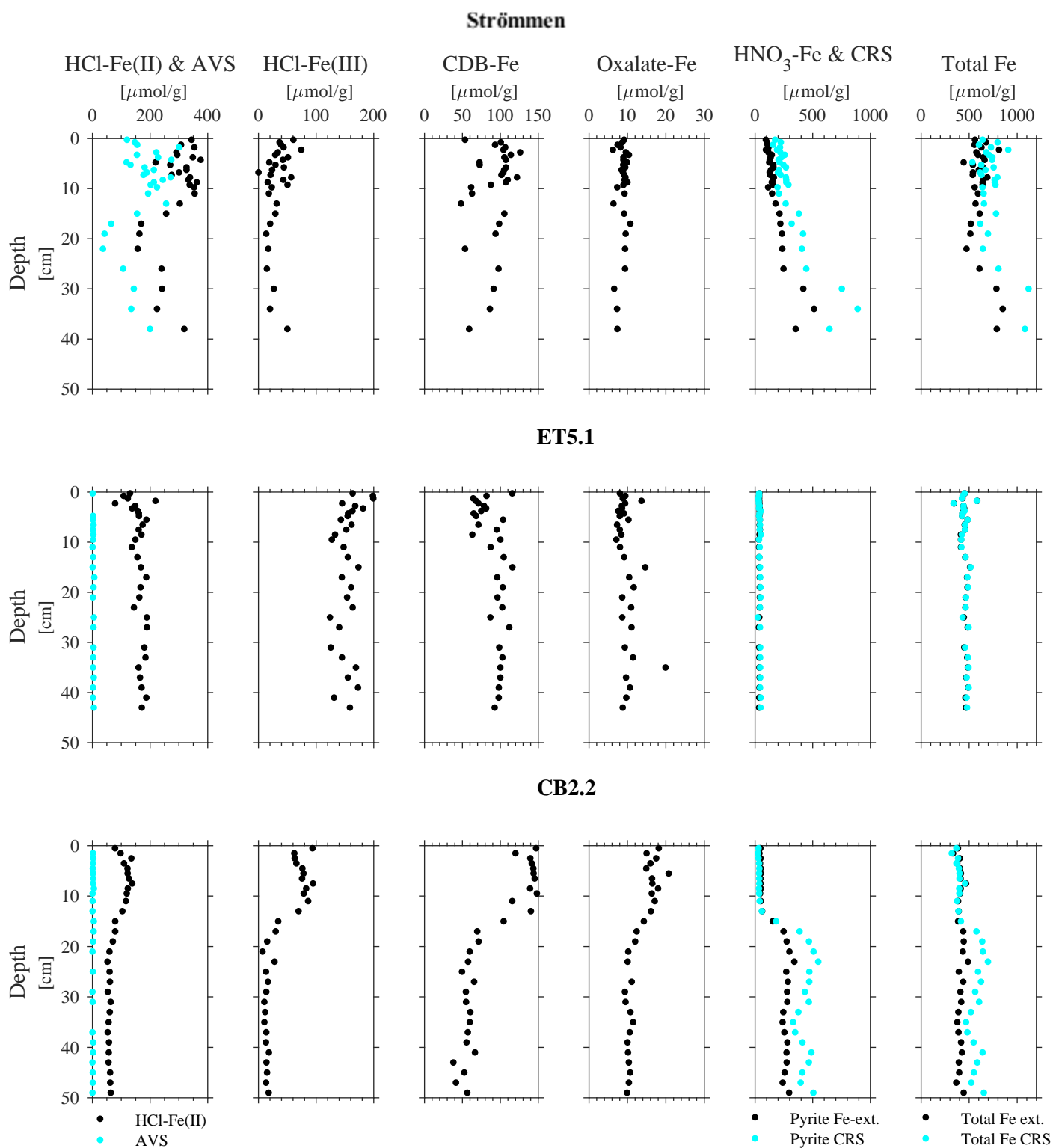


Figure 9: Depth profiles of S and Fe pool distribution: Results of the Fe-extraction are presented in black, S-extraction data in cyan. The sum of HCl-Fe(III) and CDB-Fe is the Fe-oxide pool, while the oxalate-Fe(III) is considered to be magnetite. HNO_3 -Fe is supposed to represent the pyrite.

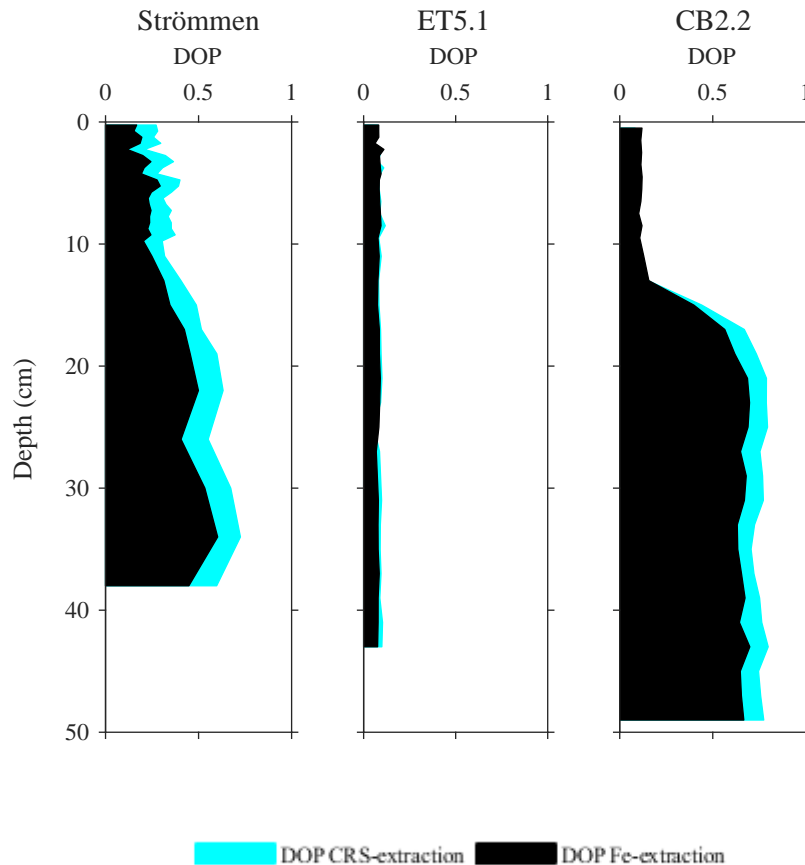


Figure 10: Comparison of the degree of pyritization between pyrite determined based on S and Fe extractions for all three study sites.

At all three study sites, most of the particulate P was associated with the CDB-pool, followed by the organic pool. However, the amount of particulate P differed significantly and subsequently, the size of the different P pools (Figure 11).

The top cm at Strömmen was enriched in P (Figure 7, 11), with concentrations three times as high as for the rest of the core. 74 % of the total 160 $\mu\text{mol/g}$ particulate P was associated to the CDB-P pool in the top cm. For the remaining sediment, the size of the different P-pools was relatively stable. Generally, 12.4 $\mu\text{mol/g}$ of the 48 $\mu\text{mol/g}$ total P was bound as organic P. Authigenic and detrital P contributed with 6.6 and 8.2 $\mu\text{mol/g}$ to the total P pool. The exchangeable P pool was very small with a mean contribution of 1.8 $\mu\text{mol/g}$. The CDB-P pool was the largest pool with approximately 18.9 $\mu\text{mol/g}$, however, also showed the greatest variation in depth. Despite extracting significant amounts of P in the CDB-step, the Fe concentrations in the CDB-solution were generally below 50 $\mu\text{mol/g}$ below 1 cm depth (Appendix C). No Mn^{2+} was detectable. Silica concentrations were comparable to Fe in the CDB solution, followed by Al and Ca. The detected Mg in the CDB-solution was higher than at the other two sites.

ET5.1 had the largest CDB-P pool of all sites. On average, 80 % (40-50 $\mu\text{mol/g}$) of the particulate P were extracted in the CDB step. High concentrations of Fe (between 200 to 300 $\mu\text{mol/g}$) and Mn (20 to 40 $\mu\text{mol/g}$) were detected in the CDB solution (Appendix C). 15% of the particulate P was associated with organics, leading to very small pools of detrital, authigenic and exchangeable P.

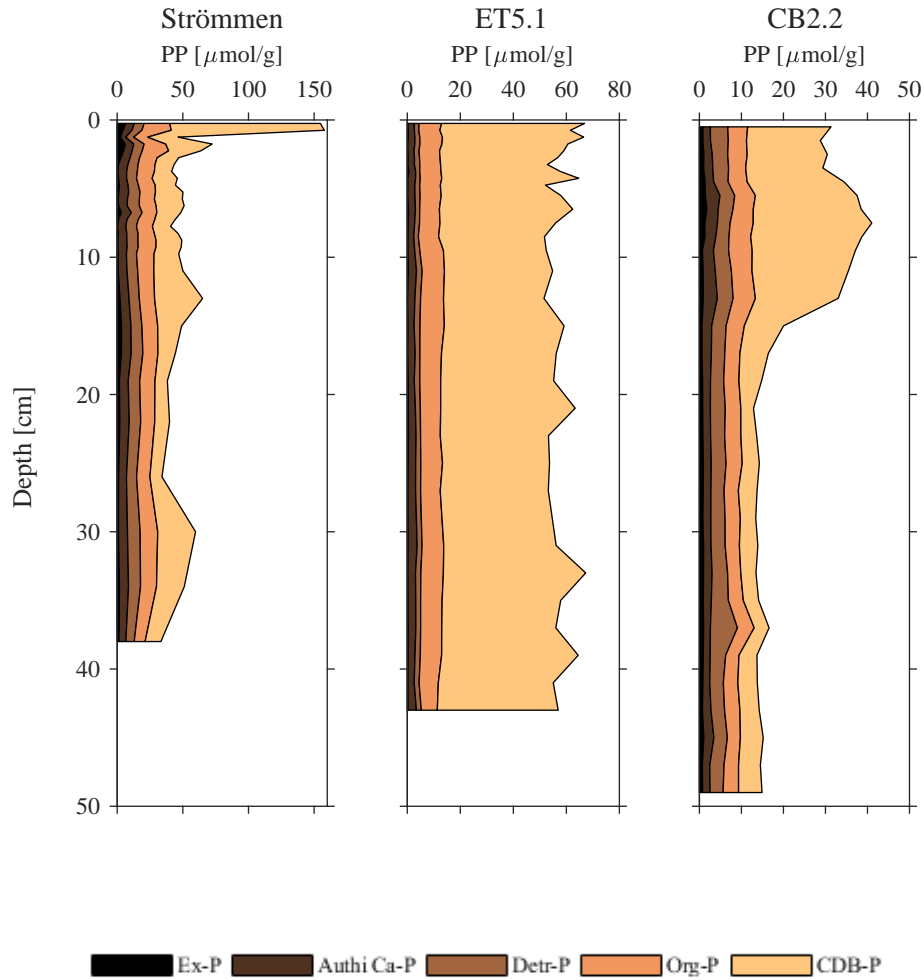


Figure 11: Depth profile of particulate phosphorus (PP) pool distribution

Throughout the sediment core at CB2.2, approximately $0.9 \mu\text{mol/g}$, $2.2 \mu\text{mol/g}$, $3.5 \mu\text{mol/g}$, and $4 \mu\text{mol/g}$ were bound respectively as exchangeable, authigenic, detrital and organic P. The CDB-P pool was in the upper 15 cm the most significant pool, with concentrations ranging from 17 to $29 \mu\text{mol/g}$, while in the deeper sediment only $4.7 \mu\text{mol/g}$ was dissolved by the CDB. Consequently, the organic and CDB associated P pools were comparable at depth. Nearly no Fe was dissolved in the CDB between 20 and 40 cm. In this sediment interval only Al, Ca and Si were detectable in the CDB. The dissolved Fe concentration increased below 40 cm depth (Appendix C).

The results of the Fe and P extraction were combined to calculate the feasible forms of Fe-associated P burial. The different ratios (see Section 2.6 for explanation) are presented in Figure 12. At Strömmen the ratio of CDB Fe/P was generally below 1.5, while the ratio of Fe-oxides to CDB-P ranged between 1.5 and 10. Total S to reactive Fe was increasing with depth from 5 to 12, highlighting the increase in total S with depth.

Ratios of CDB Fe (+Mn) / P, and Fe-oxides to CDB-P were above 1.5 at ET5.1. Total S to reactive Fe ratios were stable with a value of ~ 0.5 , indicating a depletion in S.

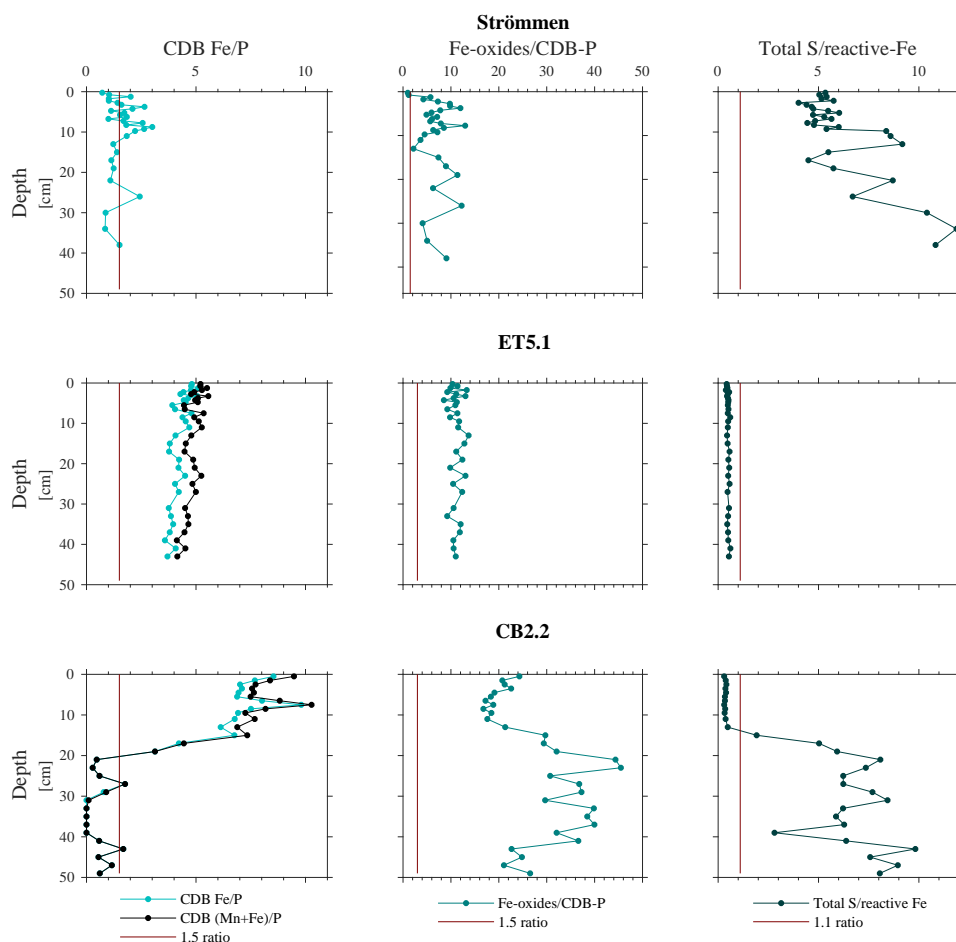


Figure 12: Ratios used to assess the likelihood for the presence of vivianite. CDB Fe/P and Fe-oxides to CDB-P ratios above 1.5 indicate that vivianite formation might be feasible (Dijkstra et al., 2016), while total S to reactive Fe ratios below 1.1 suggest potential vivianite formation (Rothe et al., 2015).

At CB2.2, CDB Fe/ P were in the upper 20 cm above 1.5, while the deeper sediment was depleted in Fe. Fe-oxides to CDB-P ratios ranged from 20 to 45, indicating a depletion in P in contrast to Fe-oxides. Matching to the total S trend, the upper 13 cm had a small total S to reactive Fe ratio (< 1.1), while the deeper sediment had ratios generally above 5.

3.4 Assessment of the relationship between Fe-P-Mg in sediment burial

3.4.1 SEM-EDS

For all three sites, three sediment intervals were analyzed by the SEM-EDS in order to gain insight into possible inorganic forms enriched in Fe and P.

Crystals resembling vivianite were not found at CB2.2 nor Strömmen. An overview image of a general composition found at 30 cm depth at Strömmen is shown in Appendix E.1. Pyrite-like

structures were very common and match the high DOP values at depth. However, crystals with a very distinct flat structure were visible. These were either enriched in Fe and Mg (see Appendix E.1) or slightly enriched in Mg and P as presented by the EDS spot analyses in Figure 13. The crystal shape could resemble the crystal structure seen in the vivianite mineral family, which includes baricite, reported by Dijkstra et al. (2018) or amorphous magnesium phosphates such as struvite and newberyite (Graeser et al., 2008; Rahman et al., 2014; Qi et al., 2015; Babaie et al., 2016).

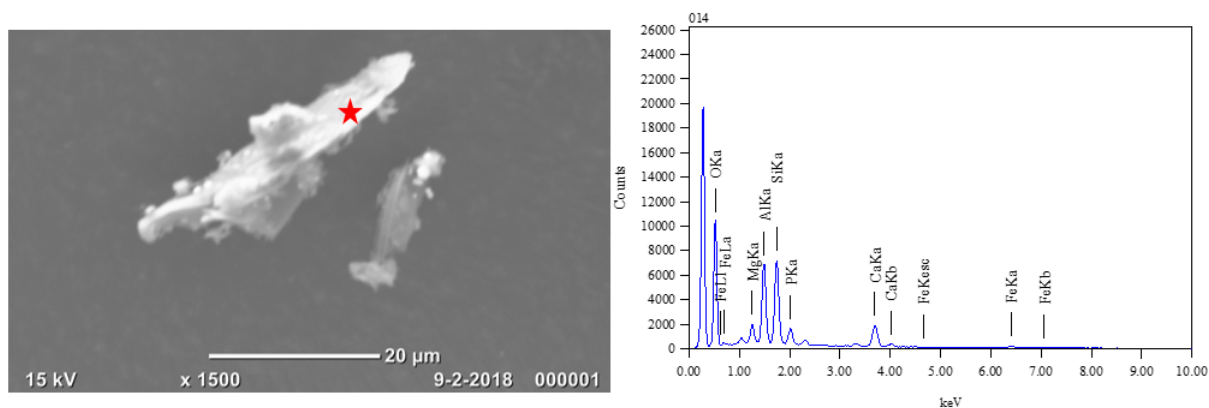


Figure 13: Crystal enriched in Mg and P at 30 cm depth, Strömmen

In all of ET5.1's intervals, crystals resembling vivianite were observed (Figure 14 and for more examples Appendix E.2). These crystals were similar in appearance to those from the deepest part of the Bothnian Sea (site US5B) (Egger et al., 2015), and at 1.6 mbsf at Landsort Deep (Dijkstra et al., 2016). Quantitative analyses (spot analyses and area mapping) with the EDS (Figure 14) revealed relative molar Fe (+Mn) to P ratios in the range of 1.5 to 3.4 (2.4 to 4.6) (Table 10 in Appendix E.2). All vivianite-like crystals found at ET5.1 were significantly enriched in Mn. Additionally, further inspection with the light microscope showed that the crystals had a blue color gradient and resembled reflected-light microscope images as reported for vivianite by Rothe et al. (2016).

In Appendix E.3 an overview image of the sediment interval at 29 cm depth of CB2.2 can be found. The figure displays an enrichment in pyrite. Moreover, at the edge of the image, a crystal enriched in Ca and P is observed.

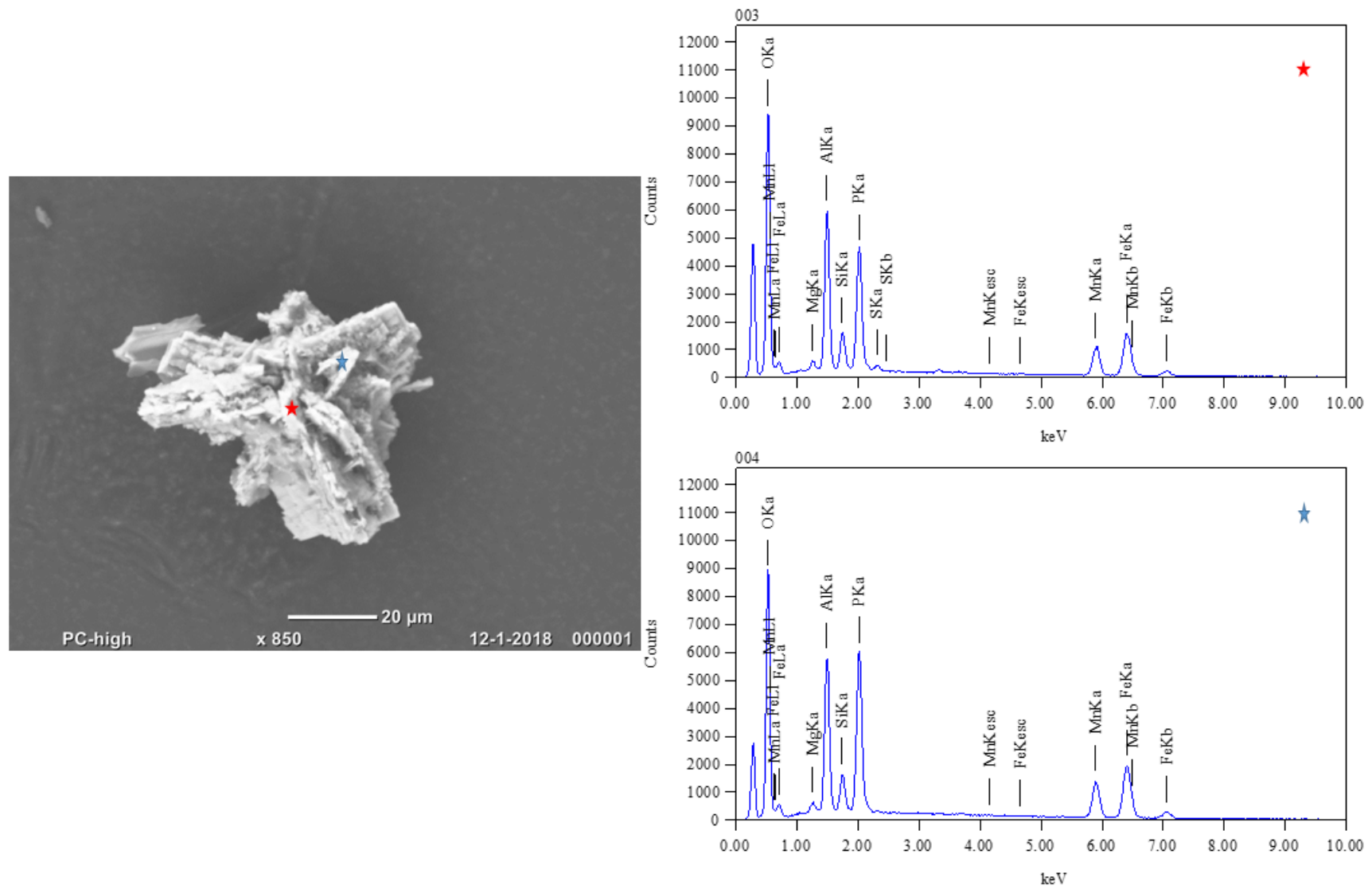


Figure 14: Vivianite like crystal found at 11 cm depth at ET5.1

3.4.2 μ XRF

μ XRF measurements were carried out to further investigate the elemental relationship between the crystals identified at ET5.1 and Strömmen.

For Strömmen, as already expected due to the high DOP value, a correlated enrichment of Fe and S was visible in the elemental maps (Figure 15). Additionally, Ca and P were enriched simultaneously (Figure 15, Appendix F, Figure 28a). Furthermore, P was correlated with Fe + Mg with a ratio between 5.2 and 11.8 (Figure 16; Appendix F Figure 28 b & d). A strong correlation of P to Mg was detected at 22 and 30 cm depth (Figure 28 d, Appendix F). The coinciding enrichment in Mg, P and Fe was also supported by the SEM images (see Section 3.4.1). Furthermore, P distribution appears to be randomly associated to Cu (Figure 29, Appendix C). Overall, these results support the finding of the SEDEX that Fe and Ca-species play a role in P burial at Strömmen.

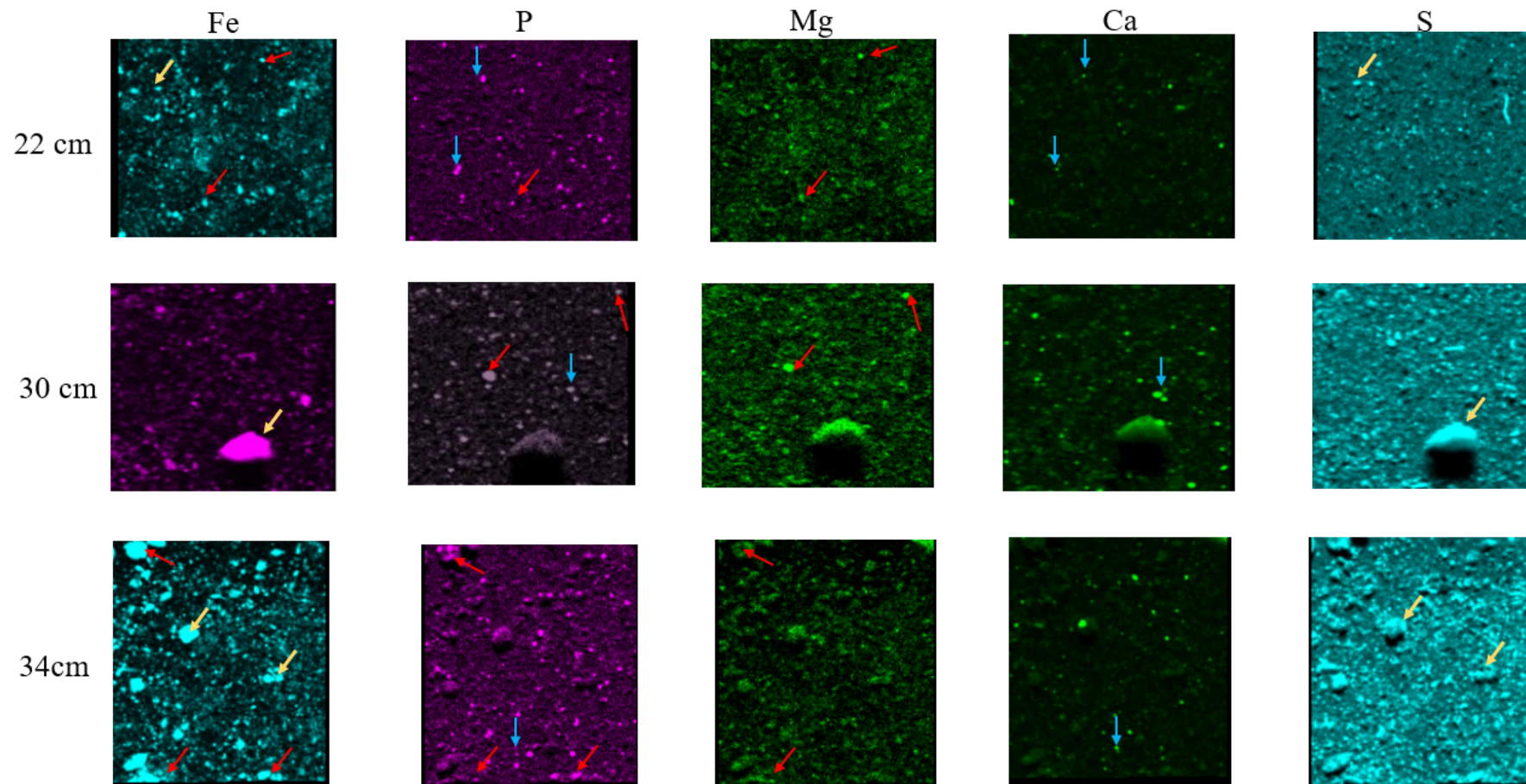


Figure 15: Elemental μ XRF maps of Fe, P, Mg, Ca and S of Strömmen for depths below calculated supersaturation of vivianite in the porewater (22, 30, and 34 cm). Enrichments in Fe, P and Mg are indicated by red arrows, yellow arrows indicate an enrichment in Fe and S, while blue arrows illustrate enrichments in Ca and P

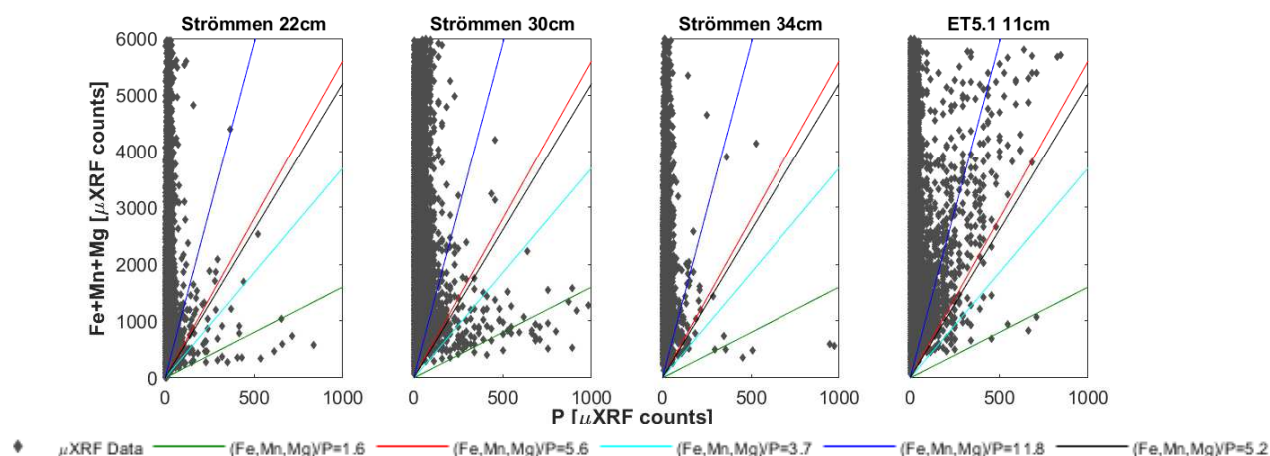


Figure 16: Correlation between Fe+ Mn+ Mg to P intensity counts based on the μ XRF; Reference lines with slopes of 1.6, 3.7, 5.2 and 11.8 are ratios reported for vivianite minerals by Dijkstra et al. (2016), while the ratio of 5.6 is based on the elemental ratio detected for vivianite-like crystals by the SEM-EDS for ET5.1 at 11 cm depth (Table 10 in Appendix E.2)

The measurement of ET5.1 at 11 cm shows that many crystals are enriched in Mn, Fe, and P (see Figure 17). Furthermore, correlating the sum of the μ XRF counts of Mn, Mg, and Fe to the counts of P, a correlation pattern with a ratio between 1.5 to higher than 11.8 is seen (Figure 16). These are elemental ratios found for vivianite at Landsort Deep (Dijkstra et al., 2016). The found correlation between Mn, Mg, Fe to P was significantly stronger than between Ca and P (see Appendix F, Figure 28a). In summary, these results strongly support the finding that at ET5.1, P burial is linked to Fe and Mn (ferrous/manganese phosphates) and is not linked significantly with Ca (apatite). Additionally, more coinciding enrichments in Fe and P were detected for ET5.1 than for Strömmen.

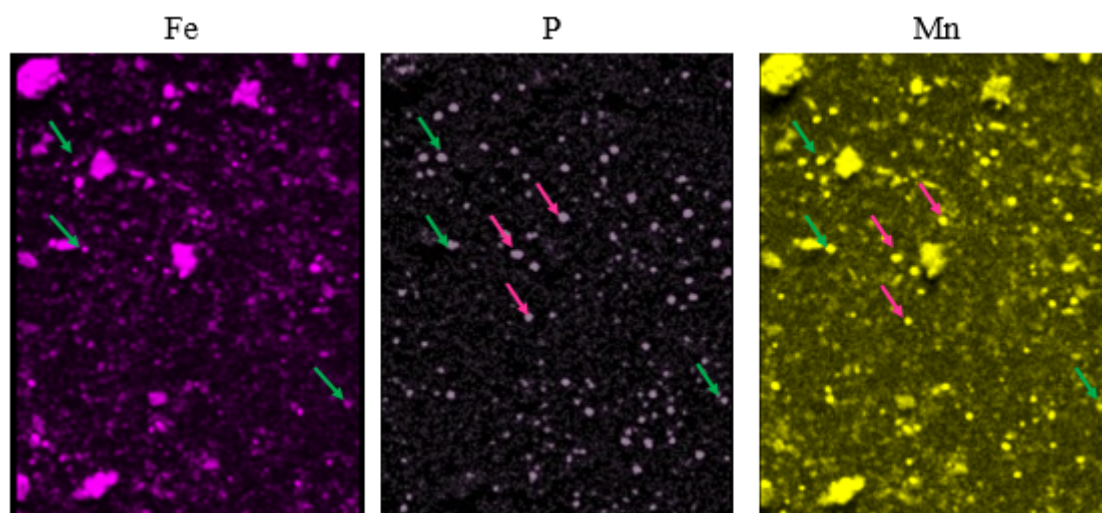


Figure 17: Elemental maps of ET5.1 at 11 cm depth. Green arrows indicate coinciding enrichment in Fe, Mn and P, while pink arrows show simultaneous enrichment in Mn and P.

4 Discussion

First, the depositional history and its effect on the diagenetic regime of each site is briefly discussed (Section 4.1). In Section 4.2, the influence of Fe to S dynamics for permanent P burial is reviewed. Section 4.3 discusses the nature of the CDB-P pool, followed by the analysis of the coastal nutrient filter function with regard to salinity in Section 4.4.

4.1 Steadily versus non-steadily accumulating sedimentary systems

4.1.1 Strömmen

No ^{210}Pb data for Strömmen is available yet, making it difficult to assess if the system is steadily accumulating. Nevertheless, stable total Mn and Mg concentrations propose a steady deposition (Figure 8). In contrast to Mn and Mg, Fe and S are enriched in the lower 10 cm of the sediment (Figure 8 & 23). This corresponding enrichment does not necessarily need to be caused by changes in deposition. For instance, persistent low oxygen conditions leading to highly reducing conditions could have favored formation of iron sulfides, resulting in simultaneous enrichment. Also the porewater data does not show signs of disturbance, so that a steadily accumulating diagenetic regime is assumed for further interpretation (Aller, 2014).

4.1.2 ET5.1

The sediment at ET5.1 appears to accumulate steadily, resulting in a stable total elemental composition, steady mud/sand distribution, and a constant decline in ^{210}Pb (Figure 8 and Appendix A). The derived sedimentation rate of 0.49 cm yr^{-1} is in the range typically reported for the Chesapeake Bay (Brush et al., 1982; Arnold et al., 2000; Palinkas et al., 2017).

4.1.3 CB2.2

In this section, the depositional history of CB2.2 will be reviewed, aiming to explain the unusual sediment profiles described in Section 3.

Significant changes in organic carbon, mud/sand distribution and unusual trends in the ^{210}Pb activity suggest that the sediment is not steadily accumulated (Figures 5, 6). The sediment is likely subject to reoccurring resuspension and erosion during large storms, and experiences high rates of deposition from the Susquehanna loading (Williams and Reed, 1972; Hirschberg and Schubel, 1979; Sanford, 1994; Palinkas et al., 2014). For instance, the upper ^{210}Pb profile points towards resuspension. During flooding conditions, the most recently deposited river sediment is eroded first and transported to the upper bay. With continuous flooding, older sediment depleted in ^{210}Pb settles on top of the new sediment, explaining likely the increase in ^{210}Pb from the water-sediment interface to 11 cm depth (Figure 6) (Hirschberg and Schubel, 1979). The enrichment in sand between 15 and 20 cm strongly indicates a major erosional event (Palinkas et al., 2014). Below 20 cm, the deposition is older as indicated by low ^{210}Pb activity.

Besides the dynamic depositional history, the porewater data suggest a complex lateral advection flow. This advection flow might be enhanced by the presence of the sand layer, but certainly relates to the small scale geography of groundwater discharge. The Cl^- profile (Figure 21, Appendix B) shows a source of fresh water below 10 cm. Saline water re-intrudes below this fresher water, indicated by the increase in SO_4^{2-} (Figure 7).

Taken together the unusual sediment profiles probably result from a complex interaction between lateral advection flow and non-steadily accumulating depositional history. The influence of these processes on the P dynamics will be elaborated in Section 4.2.2.

4.2 Fe-S-P dynamics

This section will mainly address the research question if authigenic ferrous phosphate is found in other coastal sites besides the Bothnian Sea. The sedimentary dynamics at CB2.2 differ strongly from ET5.1 and Strömmen (Section 4.1). Therefore, first the P-dynamics at ET5.1 and Strömmen are elaborated, followed by a discussion of the influence of the lateral advection flow on P dynamics at CB2.2.

4.2.1 Role of vivianite-type minerals in P burial

High porewater concentrations of HPO_4^{2-} and Fe^{2+} and low levels of HS^- facilitate possible authigenic ferrous phosphate formation in aquatic sediments (Nriagu, 1972). At Strömmen and ET5.1, HPO_4^{2-} appears to be removed with depth in the presence of Fe^{2+} (Figure 7). However, there are certain differences in the removal mechanism. At Strömmen, HS^- generated likely by microbial SO_4^{2-} reduction removes Fe^{2+} from the porewater; thus limiting potential authigenic vivianite formation above 22 cm depth (Ruttenberg, 2003). In contrast, at ET5.1 no HS^- was detectable and bottom water SO_4^{2-} concentration was very low (Figure 7). High Fe^{2+} and Mn^{2+} concentrations reflect no significant scavenging by HS^- . Therefore, it seems feasible that authigenic vivianite formation occurs nearly through the whole sediment core. This would further explain the relatively low HPO_4^{2-} concentrations in comparison to elevated DIC and NH_4 concentrations at ET5.1.

The results of the saturation calculations support that at Strömmen only below 22 cm vivianite formation is thermodynamically feasible, while at ET5.1 all sediment intervals are supersaturated (Table 6 & 7, Appendix B).

At Strömmen, the trends of the sediment extraction data do not offer a straightforward interpretation for possible vivianite formation.

The steadily increasing and high DOP and pyrite concentrations imply that Fe is limited for any reactions besides HS^- with depth (Figure 9 & 10) (Ruttenberg, 2003). Additionally, the ratio between total S to reactive Fe shows that available Fe is limited in the sediment (Figure 12), (Rothe et al., 2015). Based on this, most reactive Fe is scavenged by HS^- at Strömmen. This data, hence would speak against authigenic vivianite formation.

The SEDEX data shows that at depth apatite (Authi Ca-P and Detr-P) and organic-P are important P burial pools as expected for the Baltic area (Jensen et al., 1995; Mort et al., 2010; Rydin et al., 2011) (Figure 11). This is also supported by the μXRF data showing a strong correlation between

Ca and P, indicating potentially the presence of apatite in all investigated sediment intervals (Figure 15 & 28, Appendix E.3). Significant association of P to CaCO_3 , as reported by Kraal et al. (2017), can be excluded due to extremely low CaCO_3 content (Figure 5).

On the other hand, 40 % of the particulate P was dissolved in the CDB step (Figure 11), suggesting P burial associated with Fe at depth. Regarding the ratio of dissolved Fe to P in the CDB solution (Figure 12), not sufficient Fe is available to have the dissolved P in the form of vivianite (Figure 22, Appendix C) (Dijkstra et al., 2016). Besides Fe, also Ca, Al and Si species were dissolved (Figure 22, Appendix C). This potentially implies that not all P extracted in the CDB-step is associated with Fe. This limitation is discussed further in Section 4.3.1.

The μXRF data show a coinciding enrichment in Fe and P below 22 cm, also associated to a simultaneous enrichment in Mg (Figure 15). At 30 cm depth, enrichments in P were actually only coinciding with enrichments in Mg (Figure 15). Additionally, the correlation plots between Mg+Fe+Mn to P (Figure 16) show a clear correlation in intensity counts. This correlation is weaker if only Fe to P or Mg to P is regarded (Figure 28, Appendix E.3). The ratio of Fe + Mn + Mg to P lies mostly between 5.2 and 11.8 (Figure 16). These ratios corresponds to reported ratios for vivianite at Landsort Deep (Dijkstra et al., 2016). This would argue in favor of authigenic ferrous phosphate formation at Strömmen.

As already stated prior, the dissolved Fe in the CDB step is not sufficient for vivianite formation. Based on the μXRF data, especially at 22 and 30 cm, a strong link between Mg and P is visible (Figure 15 & 28, Appendix E.3). Subsequently, it may be hypothesized that Mg significantly substitutes Fe in the formation of an authigenic phosphate mineral. This would further explain why crystals identified by the SEM resemble more Mg-enriched vivianite minerals (Dijkstra et al., 2018).

Another phosphate mineral enriched in Mg is struvite. However, based on saturation calculations struvite is not supersaturated (Table 6, Appendix B). Moreover, additional conditions required for struvite formation are not met at Strömmen (Dijkstra et al., 2018, and references therein).

The data, thus, suggests that a Mg-enriched mineral of the vivianite group is responsible for the removal of HPO_4^{2-} from the porewater below 22 cm. Why Mg plays a significant role in vivianite formation at Strömmen and not at other coastal sites will be elaborated in Section 4.3.2.

In comparison to Strömmen, the solid phase data complement well the hypothesis of authigenic ferrous phosphate formation based on the porewater data at ET5.1. High Fe-oxide concentrations and a low DOP value imply that most Fe is theoretically available for reactions with P (Figure 9 & 10). Indeed, the majority (about 80%) of particulate P is associated with Fe (Figure 11). Only 15% of particulate P is in the form of organics. These results agree well with the data presented by Hartzell et al. (2017) for the same study site.

The ratio of Fe to P in the CDB solution is above 1.5 and total S to reactive Fe is below 1.1. Both these ratios suggest consequently that vivianite formation may be feasible (Dijkstra et al., 2016; Rothe et al., 2015). Vivianite dissolves in the first two steps of the Fe-extraction and the CDB step of the SEDEX (Nembrini et al., 1983; Dijkstra et al., 2014). Consequently, both fractions consist of a combination of Fe and P associated with Fe-oxides and vivianite. A set of equations (Appendix H) is used to estimate the proportion of Fe-bound P that could be vivianite (Egger et al., 2015).

Based on this calculation, $\sim 52\%$ could possibly be vivianite for the whole sediment core. This estimate is similar to the estimate of Egger et al. (2015) for the Bothnian Sea.

The SEM images and μ XRF data provide further evidence for the presence of vivianite. Visually the vivianite was identified based on its platy and needle-shaped crystals (Figure 14 & 26, Appendix E.2) (Egger et al., 2015; Rothe et al., 2016). Furthermore, spot-analyses revealed a concurrent enrichment in Fe, P, and also Mn (Figure 14 & 26, Appendix E.2). The ratio between Fe/P ranged from 1.49 to 3.4, while the Mn/P ratio was slightly lower with 0.87 to 2.1 (Table 10 in Appendix E). These ratios are within the range of reported ratios for vivianite in marine settings (Dijkstra et al., 2016, 2018). At ET5.1, Mn appears to play quantitatively a similar role in vivianite formation as Fe. Substitution of Fe^{2+} by Mn^{2+} has been mainly reported for freshwater sediments (Fagel et al., 2005; Sapota et al., 2006), but also for brackish sites in the Bothnian Sea (Egger et al., 2015; Lenstra et al., in prep.).

Besides vivianite formation, the μ XRF and saturation calculation results conceivably indicate manganese phosphate formation (simultaneous enrichment in Mn and P) (Figure 17). This could only be identified by further analyses, for instance with the synchrotron.

Comparing Strömmen and ET5.1 reveals that SO_4^{2-} dynamics influence authigenic ferrous phosphate formation. An authigenic ferrous phosphate mineral formation occurs at both sites. Due to the shallow position of the SMTZ and non-detectable HS^- vivianite precipitation occurs throughout the whole sediment core at ET5.1, whereas high concentrations in HS^- inhibit authigenic ferrous phosphate formation above 22 cm depth at Strömmen. Based on these two sites, the amount of P buried in vivianite depends significantly on the scavenging capacity of HS^- for Fe. Consequently, increasing salinity seems to lead to smaller vivianite pools. Furthermore, as more reactive Fe is bound to HS^- , other P burial fluxes become important. This will be further elaborated in Section 4.4. Another apparent feature at ET5.1 and Strömmen is the influence of the local geochemistry on the composition of the precipitating ferrous phosphate (significant participation of Mn and Mg respectively).

4.2.2 Influence of lateral intrusion on P dynamics: CB2.2

A complex diagenetic regime is present due to the lateral intrusion of fresher groundwater and saline water at depth, possibly enhanced by the presence of sediment enriched in sand at CB2.2 (Huettel et al., 1998; Huettel and Webster, 2001). Fresher groundwater flows in at around 10 cm depth, indicated by a decline in Cl^- (Figure 21, Appendix B), while the recharge of saline water is indicated by an increase in SO_4^{2-} between 20 and 30 cm (Figure 7). This resembles features of a subestuarine flow (Charette et al., 2005). The influence of these dynamics on the P burial are elaborated in the following paragraph.

In the younger, upper 10 cm of sediment, OM degradation leads to a concave increase in NH_4^+ and DIC (Figure 7), (Libes, 2011; Schulz and Zabel, 2006). Despite mineralization, HPO_4^{2-} concentrations remain low, pointing to an immediate removal of HPO_4^{2-} either by sorption or authigenic

mineral formation (Figure 1), (Ruttenberg, 2014). The rapid increase in Fe^{2+} implies that reductive dissolution of Fe-oxides surpasses the removal capacity of HS^- . Consequently, the removal of HPO_4^{2-} could be related to high Fe^{2+} concentrations. Since no HS^- was detectable, even authigenic vivianite formation would be feasible (Nriagu, 1972). This is also indicated by supersaturation of vivianite between 2.5 and 9.5 cm depth (Table 8, Appendix B).

The solid phase data support the hypothesis that the drawdown of HPO_4^{2-} is related to Fe. On average, 21 $\mu\text{mol/g}$ of particulate P is dissolved in the CDB-step (65% of all particulate P at that depth). The ratio of Fe to P extracted in the CDB step lies between 7 to 10 (Figure 12) and is within the typical range of ratios of Fe-oxides to P in the marine environment (Savenko, 1995; Slomp et al., 1996; Anschutz et al., 1998; Gunnars et al., 2002). Based on the saturation calculations and total S to reactive Fe ratios, authigenic vivianite might also be feasible (Figure 12, Table 8) (Rothe et al., 2015). Applying the same set of equations as in Section 4.2.1, 5 to 15% of the Fe-bound P could potentially be in the form of vivianite at 5 to 10 cm depth. This suggests that the majority of HPO_4^{2-} is bound directly to Fe-oxides, matching the visual inspection carried out with the SEM, in which no ferrous phosphates were found. As the percentage of expected vivianite is very low, it is likely that crystals might have been missed by the SEM or were too small in order to be identified (Jilbert and Slomp, 2013).

At the depth of the groundwater intrusion and saline water recharge, HPO_4^{2-} concentrations in the PW increase (Figure 7) indicating that the sediment loses its P binding capacity. Likely, Fe-oxides are scavenged by HS^- , leading to a decline in Fe-oxides and increase in pyrite and DOP at depth (Figure 9 & 10). As the Fe-oxides are reduced, the associated HPO_4^{2-} is released to the porewater. One portion diffuses down, leading to an increase in HPO_4^{2-} at depth, while another part is probably reabsorbed by Fe-oxides and Mn-oxides in the surface sediments (Middelburg and Levin, 2009, and references therein). The loss in Fe-bound P at depth is also indicated by the SEDEX data, where the CDB-P pool declined in comparison to the upper sediment by 80%. Additionally, the total particulate P concentration declined by half, highlighting the loss of P burial efficiency in the sediment at depth. The majority of buried P is associated with organics and apatite as commonly expected for coastal systems (Ruttenberg, 2003; Mort et al., 2010). Only 20 % of particulate P is dissolved in the CDB-P step. However, dissolved Fe and Mn concentrations in the CDB solution were very low, making it questionable if the CDB-P pool is truly an Fe-bound P fraction (Figure 22, Appendix C). This limitation of the CDB-step is further discussed in Section 4.3.1.

Below 40 cm, corresponding to the depth of SO_4^{2-} depletion (Figure 7), HPO_4^{2-} concentrations suddenly decline, pointing towards a removal mechanism. The cause behind this decline is not evident. Theoretically, the drawdown of HPO_4^{2-} could be caused by a diffusive flux resulting from a sink-switch to an authigenic mineral formation. Since Fe^{2+} concentrations increase also slightly below 40 cm, authigenic ferrous phosphate precipitation below the second SMTZ is a feasible hypothesis. Apatite formation, however, could also be possible since it is supersaturated in the porewater (Table 8, Appendix B). Data from deeper sediment intervals would be required to reveal the source of HPO_4^{2-} drawdown.

The role of Fe-oxides as a phase for efficient P burial is shown at CB2.2. The upper sediment,

which is enriched in Fe-oxides, is capable in retaining 57 % more particulate P ($\sim 19 \mu\text{mol/g}$) than the deeper sediment, where most reactive Fe is associated with S. Evidence for ferrous phosphate formation could not be shown. However, it cannot be excluded as a possible phase for P burial in the upper sediment.

4.3 Nature of CDB-P pool

4.3.1 Limitations

Sequential extraction methods only identify indirectly targeted mineral phases (e.g. Hyacinthe and Van Cappellen, 2004). To identify certain mineral phases, different methods need to be combined. The combination of traditional extraction methods and spectroscopic techniques was successful to identify ferrous phosphates. However, some limitations regarding the sequential extraction methods appeared along the process.

The CDB-step of the SEDEX is considered to target the Fe-bound P phase (Ruttenberg, 1993). However, reports on the dissolution of other non-target P-phases, challenges the accuracy of this step (Jensen and Thamdrup, 1993; Kostka and Luther, 1994; Dijkstra et al., 2016). At Strömmen, and especially at CB2.2, dissolved Fe concentrations in the CDB-solution were very low despite extracting significant amounts of P (Figure 22, Appendix C). For instance, an average of $\sim 4 \mu\text{mol/g}$ P was extracted between 31 and 39 cm depth at CB2.2. No Fe nor Mn was detected in the CDB-solution. This clearly shows that the CDB-P pool does not necessarily translate into the Fe-bound P pool. Simultaneously, Ca, Al, and Si were detectable in significant amounts, suggesting a potential underestimation of other P pools such as apatite (Petersen et al., 1966; Schenau and De Lange, 2000).

Despite low Fe-concentrations in the CDB step of the SEDEX, Fe-oxide concentrations were high in these sediment intervals (Figure 9). Possibly, the Fe-extraction overestimates the Fe-oxide pool. It has been shown that magnetite and clay particles can be extracted in the first two steps of the Fe-extraction (Poulton and Canfield, 2005; Claff et al., 2010).

The need to combine different methods is also stressed for being able to find the interaction of other cations in authigenic vivianite formation. The Mn- and Mg-enriched vivianite crystals would have not been revealed by sequential extractions and is only detected by the SEM-EDS and μXRF .

4.3.2 Interactions of Mg in ferrous phosphates

At Strömmen, Mg- enriched ferrous phosphates appear to be a phase of permanent P burial (Section 4.2.1). This is the first time that authigenic Mg-enriched ferrous phosphates have been reported for a coastal system. So far, it has only been shown in marine settings (Burns, 1997; Hsu et al., 2014; Dijkstra et al., 2016). Vivianite is the Fe-rich end member of the vivianite mineral group, while baricite is the Mg-rich end member (Section 1.1). Vivianite crystals with a chemical composition anywhere between vivianite and baricite are likely in the marine realm due to higher Mg concentrations than found in lacustrine systems (Rothe et al., 2016). A question remaining is why Mg plays

a role in the formation of ferrous phosphates at Strömmen and not at other coastal sites.

The knowledge on the rate and mechanism of vivianite crystal growth is very limited (Rothe et al., 2016). An answer based on kinetic or thermodynamic grounds is consequently not feasible. Therefore, Strömmen is compared to two sites in the Bothnian Sea: US5B and Öre estuary (Egger et al., 2015; Lenstra et al., in prep.), where vivianite was found below the SMTZ. The concentrations of SO_4^{2-} , Mg^{2+} , Ca^{2+} and NH_4^+ are comparable among the three sites (Figure 35, Appendix I). However, Strömmen has significantly lower Fe^{2+} and Mn^{2+} and higher HPO_4^{2-} concentrations than US5B and Öre estuary. Strömmen is also depleted in reactive Fe in comparison to total S.

Vivianite at US5B and Öre estuary is enriched in Mn^{2+} , showing the influence of the surrounding geochemical composition on authigenic minerals. Possibly, Mn^{2+} has a higher affinity to vivianite crystal growth than Mg^{2+} does. Consequently, it becomes chemically feasible for Mg^{2+} to participate in vivianite formation only when Mn^{2+} concentrations are low. Vivianite enriched in Mg had lower Mn^{2+} porewater concentrations at Landsort Deep, supporting the idea for competition between the two species (Dijkstra et al., 2016). Additionally, Mn-enriched vivianite, as found at ET5.1, has no significant amounts of Mg, supporting the idea that Mn^{2+} outcompetes Mg^{2+} (Table 10, Appendix E.2 and Figure 28d, AppendixF).

The formation of this Mg-enriched phase at Strömmen probably requires some presence of Fe^{2+} . Vivianite has in comparison to other metal phosphates a low solubility product (Nriagu, 1972). Therefore, the presence of Fe^{2+} is potentially needed to trigger nucleation of ferrous phosphate crystals. But since Fe^{2+} concentrations are very low at Strömmen, Mg^{2+} might then enable further crystal growth. This is thermodynamically probably not attractive at the other two sites as Fe^{2+} is in surplus. This is only a hypothesis and would need further support by kinetic and thermodynamic laboratory experiments.

Another significant difference between the sites is the concentration of heavy metals. In comparison to US5B and Öre estuary, Strömmen is enriched in Cu (Figure 35), Pb and Zn (data not shown here). Vivianite has been identified to immobilize Cu and Zn in soils and sediments (Liu and Zhao, 2007; Taylor et al., 2008). Since heavy metals, like Fe, have a high affinity for HS^- , they are only available for reactions with HPO_4^{2-} after the depletion of HS^- (Morse and Luther III, 1999). Certain heavy metal minerals have extremely low solubilities in soils (Bolan et al., 2003, and references therein). Potentially, heavy metals could facilitate authigenic ferrous phosphate formation with Mg involved at depth at Strömmen. Regarding the μXRF data, a connection between P enrichment and Zn and Cu is visible (Figure 29, Appendix F). The correlation is not as strong as with other elements, as both Zn and Cu are trace elements in the sediments.

Altogether, the presence of heavy metals might play a role in metal phosphate formation at Strömmen. As Fe^{2+} is very low (10 times lower than at the other two sites), but HPO_4^{2-} concentrations are very high, it might be that it becomes chemically feasible that Mg^{2+} substitutes Fe^{2+} to form metal phosphates. To support this hypothesis, more kinetic and thermodynamic data are required for minerals with a composition anywhere between vivianite and baricite.

4.4 Influence of salinity on coastal nutrient filter capacity

Sediments may retain nutrients efficiently (Nixon et al., 1996). Here, the results indicate that the efficiency of nutrient retention is strongly influenced by salinity.

As the sedimentation accumulation rate of Strömmen is not available yet, the comparison regarding P burial is not based on total P burial rates. Instead, the average P concentrations of the deeper sediment were used, where a mobilization of P may be excluded.

The permanently buried total P pool declines significantly with increasing salinity (Figure 18). The mean concentrations of P buried at ET5.1 is $\sim 20\%$ higher than at Strömmen, and 75% higher than at CB2.2. However, these sites are not located in the same estuary. Hence, other variables besides salinity might influence P burial. Regarding four subestuaries in the Chesapeake Bay, including the Choptank River, the same trend becomes apparent (O’Keefe, 2007; Hartzell et al., 2010, 2017). At low salinity (ET5.1) more than twice of particulate P is buried than at a salinity of 10 ($<40\ \mu\text{mol/g}$ to $>20\ \mu\text{mol/g}$) (Hartzell et al., 2017). Thus, this suggests that salinity is a key variable influencing the total P burial in coastal sediments.

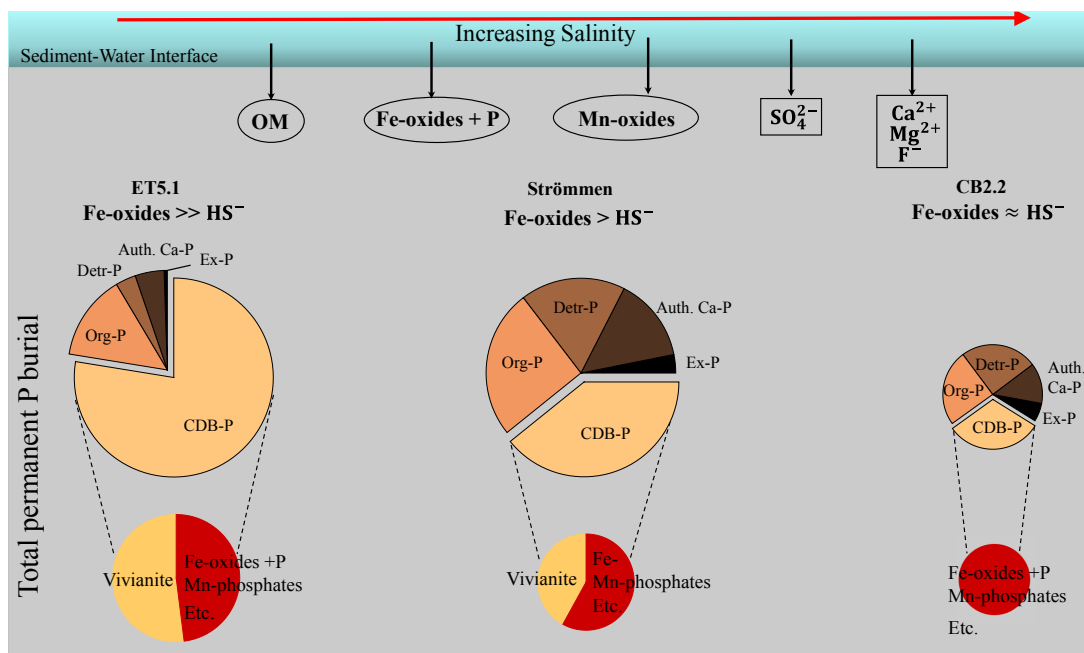


Figure 18: Decline and change in composition in the permanent buried P pool with increasing salinity. This is a simplified schematic highlighting the change in composition and size in the permanent buried P pool with increasing salinity. The data of the study sites are used as examples. Organic matter, Fe-oxides with P, Mn-oxides, SO_4^{2-} , and cations (as examples Ca^{2+} , Mg^{2+} , F^-) are available in the sediment. The amount of SO_4^{2-} increases with increasing salinity, leading to less available reactive Fe. It results in a decline in the CDB-P fraction. Other P burial pools become important. Also the role of vivianite declines with increasing salinity. The interaction of other cations besides Fe^{2+} in the formation of vivianite are excluded for simplicity. The amount of P retained declines with salinity. Besides salinity, other factors such as amount of OM, microbial community, presence of macrofauna may alter the trend. For simplicity, this is excluded in the schematic. Note that the CDB-P is composed of various mineral phases. It is possible that the Fe-bound P is overestimated in sediments.

Conceivably, the size of the buried P pool varies due to changes in composition of the P burial fluxes (Figure 18). More reactive Fe is scavenged by HS^- formed by SO_4^{2-} reduction with increasing salinity, leading to a reduction in available Fe for P burial (Krom and Berner, 1980; Caraco et al., 1989; Roden and Edmonds, 1997). This effect is seen in a reduction in Fe-bound P burial fluxes with increasing salinity (Figure 18). The reduction in Fe-bound P pools is also visible in the four subestuaries studied by Hartzell et al. (2017). The Fe-bound P pool and simultaneously the total buried P pool decline significantly at a salinity of 3 to 4. Such salinities translate roughly into SO_4^{2-} concentrations at which SO_4^{2-} reduction becomes limited by SO_4^{2-} (Boudreau and Westrich, 1984; Roden and Tuttle, 1993). Possibly, this salinity boundary also represent the limit for vivianite formation in the Chesapeake Bay. This suggests that Fe-bound P burial fluxes (and vivianite precipitation) are predominantly controlled by SO_4^{2-} concentrations. Thus, other P burial pools play a more important role at higher salinities, retaining less total P.

Despite having a more comparable salinity to CB2.2 than to ET5.1, Strömmen has a higher total P concentration at depth than CB2.2 has. Potentially, the difference is caused by the authigenic ferrous phosphate formation. The presence of vivianite has been identified as the cause of higher P retention at sites of similar environments (Rothe et al., 2016). As Strömmen has higher total Fe concentrations than the Chesapeake Bay sites (Figure 8), it shows that the balance between Fe to S is likely a key variable in P retention, allowing the inner Stockholm Archipelago to be an efficient nutrient filter (Almroth-Rosell et al., 2016; Karlsson et al., 2010; Puttonen et al., 2014).

In summary, the coastal nutrient function appears to decline with salinity as reactive Fe becomes scavenged by HS^- . This shows that besides sedimentation rate (Asmala et al., 2017), salinity is a key factor determining the coastal nutrient filter function of P. The boundary for efficient P retention might lie around 3 to 4 psu in the Chesapeake Bay. Other factors such as amount of available Fe, microbial community or presence of macrofauna might alter the boundary in other systems. Vivianite may further enhance P retention at low salinity due to lower Fe to P ratios than Fe-oxides to P (1.5 versus 10).

4.4.1 Implications

A key question remaining is how future changes may influence currently permanently buried P in the form of ferrous phosphates.

For the Chesapeake Bay, it is anticipated that salinity will increase due to sea level rise. Furthermore, lower oxygen concentrations are expected due to intensified water stratification, leading subsequently to more reducing sediment conditions (Diaz and Rosenberg, 2008; Boon et al., 2010; Najjar et al., 2010).

Regarding long-term monitoring data for CB2.2 and Strömmen, a possible link between lower oxygen concentrations and rising HPO_4^{2-} flux from sediment is visible (Appendix G). Additionally, Callender and Hammond (1982) showed that HPO_4^{2-} efflux increase with increasing salinity. The

release of HPO_4^{2-} from the sediment is potentially in both cases linked to a loss of Fe-oxides. Consequently, environmental changes expected in the Chesapeake Bay may lead to a loss of P retention capacity in the sediment, causing elevated HPO_4^{2-} fluxes. Additionally, the increase in salinity might lead to a release of HPO_4^{2-} buried currently in the form of vivianite. It has been reported that vivianite crystals are pitted or dissolved due to the presence of HS^- , and may cause increases in benthic P fluxes (Murphy et al., 2001; O'Connell et al., 2015). Dijkstra et al. (2018) showed that vivianite crystals dissolve within 100 hours of being exposed to sulfidic seawater conditions.

Summarizing, it might be postulated that in the future less P is retained by the sediment in the Chesapeake Bay, and even that some P currently buried in the form of vivianite might be released, prolonging and enhancing eutrophication. This is only an initial hypothesis and requires further assessment, for instance, through models. Also, a better understanding of the variables controlling vivianite formation and dissolution in various environments is required.

In contrast to the Chesapeake Bay, climate change prognosis indicates an increase of precipitation in the Baltic Sea region and a corresponding decline in salinity. The region around the Stockholm archipelago is expected to experience a freshening of two to three psu (Meier et al., 2006). Additionally, riverine Fe inputs to the Baltic Sea have increased in the past and are expected to rise even further (Kritzberg and Ekström, 2012; Björnerås et al., 2017). Since authigenic vivianite formation appears to be strongly influenced by Fe availability and salinity, vivianite precipitation may be strengthened in the future in the Baltic Sea, positively influencing eutrophication.

5 Conclusion

Concluding, the results strongly indicate the role of Fe to S dynamics for P burial in the coastal zone.

The P retention capacity of the sediment declines with increasing salinity. At ET5.1, ~ 20 % and 75 % more total P is buried than at Strömmen and CB2.2. Simultaneously, the P burial phases change with increasing salinity. As HS^- scavenges more reactive Fe at higher salinities, the Fe-bound P burial flux becomes less significant for total P burial. The same trend is observed in the formation of authigenic ferrous phosphate. The position of the SMTZ is deeper at higher salinity sites, resulting in a smaller reactive Fe pool below the SMTZ. Consequently, conditions favorable for authigenic phosphate formation are likely not met at higher salinity sites. At ET5.1, ~ 23 $\mu\text{mol/g}$ particulate P is likely related to vivianite at depth. This pool declines to ~ 7 $\mu\text{mol/g}$ at Strömmen and no sign of ferrous phosphates is present at CB2.2. Consequently at higher salinities, other P burial fluxes, such as apatite and organics, become more important.

Additionally, the combination of traditional extraction methods and spectroscopic techniques was successful to identify the possible presence of authigenic ferrous phosphates at two of the three study sites. The application of spectroscopic techniques unveiled the role of other cations in the formation of authigenic ferrous phosphate. If only the traditional extraction methods were used, this information may have been lost. At ET5.1, significant substitution of Fe by Mn is revealed in vivianite crystals. Mg substitutes Fe at Strömmen, leading to an authigenic phase, which is likely more similar to baricite rather than vivianite. Furthermore, the presence of heavy metals might facilitate ferrous phosphate formation. However, the exact nature of the mineral phase could not be identified and would require further analysis. The substitution of Fe by other cations needs to be further investigated, also in view of their differences in chemical behavior. This is essential in order to understand how environmental systems may react to future changes.

Summarizing, these results suggest that increasing salinity leads to a reduction in the coastal zone's capacity to retain P. The loss in retention capacity is likely linked to a decline in Fe-bound P due to scavenging of reactive Fe by HS^- . Therefore, coastal sediments may act as efficient P retention sites if Fe-bound, and especially authigenic ferrous phosphates, are present. These conditions are commonly encountered at oligohaline sites (salinity ≤ 5), implying a better buffer mechanism for eutrophication associated P loading at these sites.

References

- Aller, R. Sedimentary diagenesis, depositional environments, and benthic fluxes. 2014.
- Almroth-Rosell, E., Edman, M., Eilola, K., Markus Meier, H. E., and Sahlberg, J. Modelling nutrient retention in the coastal zone of an eutrophic sea. *Biogeosciences*, 13(20):5753–5769, 2016.
- Anschutz, P., Zhong, S., Sundby, B., Mucci, A., and Gobeil, C. Burial efficiency of phosphorus and the geochemistry of iron in continental margin sediments. *Limnology and Oceanography*, 43(1): 53–64, 1998.
- APHA. Standard methods for the examination of water and wastewater. *American Public Health Association (APHA): Washington, DC, USA*, 2005.
- Appleby, P. and Oldfield, F. The calculation of lead-210 dates assuming a constant rate of supply of unsupported ^{210}Pb to the sediment. *Catena*, 5(1):1–8, 1978.
- Arnold, R. R., Cornwell, J. C., Dennison, W. C., and Stevenson, J. C. Sediment-based reconstruction of submersed aquatic vegetation distribution in the Severn River, a sub-estuary of Chesapeake Bay. *Journal of Coastal Research*, pages 188–195, 2000.
- Asmala, E., Carstensen, J., Conley, D. J., Slomp, C. P., Stadmark, J., and Voss, M. Efficiency of the coastal filter: Nitrogen and phosphorus removal in the Baltic Sea. *Limnology and Oceanography*, 62(S1), 2017.
- Babaie, E., Lin, B., Goel, V. K., and Bhaduri, S. B. Evaluation of amorphous magnesium phosphate (AMP) based non-exothermic orthopedic cements. *Biomedical Materials (Bristol)*, 11(5), 2016.
- Berner, R. A. Sedimentary pyrite formation. *American journal of science*, 268(1):1–23, 1970.
- Berner, R. A. *Early diagenesis: a theoretical approach*. Number 1. Princeton University Press, 1980.
- Björnerås, C., Weyhenmeyer, G. A., Evans, C. D., Gessner, M. O., Grossart, H. P., Kangur, K., Kokorite, I., Kortelainen, P., Laudon, H., Lehtoranta, J., Lottig, N., Monteith, D. T., Nöges, P., Nöges, T., Oulehle, F., Riise, G., Rusak, J. A., Räike, A., Sire, J., Sterling, S., and Kritzberg, E. S. Widespread Increases in Iron Concentration in European and North American Freshwaters. *Global Biogeochemical Cycles*, 31(10):1488–1500, 2017.
- Bolan, N. S., Adriano, D. C., and Naidu, R. Role of Phosphorus in (Im)mobilization and Bioavailability of Heavy Metals in the Soil-Plant System. In *Reviews of environmental contamination and toxicology*, pages 1–44. Springer, 2003.
- Boon, J. D., Brubaker, J. M., and Forrest, D. R. Chesapeake Bay Land Subsidence and Sea Level Change: an evaluation of past and present trends and future outlook. *Special Report in Applied Marine Science and Ocean Engineering, Virginia Institute of Marine Sciences*, (425), 2010.
- Boudreau, B. P. and Westrich, J. T. The dependence of bacterial sulfate reduction on sulfate concentration in marine sediments. *Geochimica et cosmochimica acta*, 48(12):2503–2516, 1984.

- Brush, G. S., Martin, E. A., DeFries, R. S., and Rice, C. A. Comparisons of ^{210}Pb and Pollen Methods for Determining Rates of Estuarine Sediment Accumulation. *Quaternary Research*, 18 (2):196–217, 1982.
- Burdige, D. J. Estuarine and coastal sediments–coupled biogeochemical cycling. *Treatise on Estuarine and Coastal Science*, 5:279–308, 2011.
- Burns, S. J. Early Diagenesis in Amazon Fan Sediments. *Proceedings of the Ocean Drilling Program, Scientific Results*, 155:531–538, 1997.
- Burton, E. D., Sullivan, L. A., Bush, R. T., Johnston, S. G., and Keene, A. F. A simple and inexpensive chromium-reducible sulfur method for acid-sulfate soils. *Applied Geochemistry*, 23 (9):2759–2766, 2008.
- Burton, E. D., Bush, R. T., Johnston, S. G., Sullivan, L. A., and Keene, A. F. Sulfur biogeochemical cycling and novel Fe–S mineralization pathways in a tidally re-flooded wetland. *Geochimica et Cosmochimica Acta*, 75(12):3434–3451, 2011.
- Callender, E. and Hammond, D. E. Nutrient exchange across the sediment-water interface in the Potomac River estuary. *Estuarine, Coastal and Shelf Science*, 15(4):395–413, 1982.
- Canfield, D. E., Raiswell, R., and Bottrell, S. H. The reactivity of sedimentary iron minerals toward sulfide. *American Journal of Science*, 292(9):659–683, 1992.
- Caraco, N., Cole, J., and Likens, G. Evidence for sulphate-controlled phosphorus release from sediments of aquatic systems. *Nature*, 341(6240):316, 1989.
- Charette, M. A., Sholkovitz, E. R., and Hansel, C. M. Trace element cycling in a subterranean estuary: Part 1. Geochemistry of the permeable sediments. *Geochimica et Cosmochimica Acta*, 69(8):2095–2109, 2005.
- Chesapeake Bay Program. Chesapeake Bay Program Water Quality Database 1984-present. http://www.chesapeakebay.net/data/downloads/cbp_water_quality_database_1984_present, Accessed April 2018.
- Claff, S. R., Sullivan, L. A., Burton, E. D., and Bush, R. T. A sequential extraction procedure for acid sulfate soils: Partitioning of iron. *Geoderma*, 155(3-4):224–230, 2010.
- Cline, J. D. Spectrophotometric determination of hydrogen sulfide in natural waters. *Limnology and Oceanography*, 14(3):454–458, 1969.
- Compton, J., Mallinson, D., Glenn, C., Filippelli, G., Föllmi, K., Shields, G., and Zanin, Y. Variations in the global phosphorus cycle. 2000.
- Conley, D. J. Biogeochemical nutrient cycles and nutrient management strategies. In *Man and River Systems*, pages 87–96. Springer, 1999.
- Conley, D. J., Paerl, H. W., Howarth, R. W., Boesch, D. F., Seitzinger, S. P., Havens, K. E., Lancelot, C., Likens, G. E., et al. Controlling Eutrophication: Nitrogen and Phosphorus. *Science*, 323 (5917):1014–1015, 2009.

- Diaz, R. J. and Rosenberg, R. Spreading Dead Zones and Consequences for Marine Ecosystems. *Science*, 321(5891):926–929, 2008.
- Dijkstra, N., Kraal, P., Kuypers, M. M., Schnetger, B., and Slomp, C. P. Are iron-phosphate minerals a sink for phosphorus in anoxic black sea sediments? *PloS one*, 9(7):e101139, 2014.
- Dijkstra, N., Slomp, C. P., and Behrends, T. Vivianite is a key sink for phosphorus in sediments of the Landsort Deep, an intermittently anoxic deep basin in the Baltic Sea. *Chemical Geology*, 438, 2016.
- Dijkstra, N., Hagens, M., Egger, M., and Slomp, C. P. Post-depositional formation of vivianite-type minerals alters sediment phosphorus records. *Biogeosciences*, 15(3):861, 2018.
- Egger, M., Rasigraf, O., Sapart, C. J., Jilbert, T., Jetten, M. S., Roeckmann, T., van der Veen, C., Banda, N., Kartal, B., Ettwig, K. F., et al. Iron-mediated anaerobic oxidation of methane in brackish coastal sediments. *Environmental Science & Technology*, 49(1):277–283, 2014.
- Egger, M., Jilbert, T., Behrends, T., Rivard, C., and Slomp, C. P. Vivianite is a major sink for phosphorus in methanogenic coastal surface sediments. *Geochimica et Cosmochimica Acta*, 169: 217–235, 2015.
- Fagel, N., Alleman, L., Granina, L., Hatert, F., Thamo-Bozso, E., Cloots, R., and André, L. Vivianite formation and distribution in Lake Baikal sediments. *Global and Planetary Change*, 46(1-4):315–336, 2005.
- Fisher, T., Hagy III, J., Boynton, W., Williams, M., et al. Cultural eutrophication in the Choptank and Patuxent estuaries of Chesapeake Bay. *Limnology and Oceanography*, 51(part2):435–447, 2006.
- Froelich, P., Klinkhammer, G., Bender, M. L., Luedtke, N., Heath, G. R., Cullen, D., Dauphin, P., Hammond, D., Hartman, B., and Maynard, V. Early oxidation of organic matter in pelagic sediments of the eastern equatorial Atlantic: suboxic diagenesis. *Geochimica et cosmochimica acta*, 43(7):1075–1090, 1979.
- Froelich, P., Bender, M., Luedtke, N., Heath, G., and DeVries, T. The marine phosphorus cycle. *Am. J. Sci*, 282(4):474–511, 1982.
- Gao, Y., Lee, J., Neufeld, J. D., Park, J., Rittmann, B. E., and Lee, H.-S. Anaerobic oxidation of methane coupled with extracellular electron transfer to electrodes. *Scientific Reports*, 7(1):5099, 2017.
- Garnier, J., Beusen, A., Thieu, V., Billen, G., and Bouwman, L. N: P: Si nutrient export ratios and ecological consequences in coastal seas evaluated by the ICEP approach. *Global Biogeochemical Cycles*, 24(4), 2010.
- Gelesh, L., Marshall, K., Boicourt, W., and Lapham, L. Methane concentrations increase in bottom waters during summertime anoxia in the highly eutrophic estuary, Chesapeake Bay, U.S.A. *Limnology and Oceanography*, 61(2011):S253–S266, 2016.

- Glud, R. N. Oxygen dynamics of marine sediments. *Marine Biology Research*, 4(4):243–289, 2008.
- Goodbred Jr, S. L. and Kuehl, S. A. Floodplain processes in the Bengal Basin and the storage of Ganges–Brahmaputra river sediment: an accretion study using ^{137}Cs and ^{210}Pb geochronology. *Sedimentary Geology*, 121(3-4):239–258, 1998.
- Graeser, S., Postl, W., Bojar, H.-P., Berlepsch, P., Armbruster, T., Raber, T., Ettinger, K., and Walter, F. Struvite-(K), $\text{KMgPO}_4 \cdot 6\text{H}_2\text{O}$, the potassium equivalent of struvite – a new mineral. *European Journal of Mineralogy*, 20(May):629–633, 2008.
- Gross, M., Karweit, M., Cronin, W. B., and Schubel, J. R. Suspended sediment discharge of the Susquehanna River to northern Chesapeake Bay, 1966 to 1976. *Estuaries*, 1(2):106–110, 1978.
- Gunnars, A., Blomqvist, S., Johansson, P., and Andersson, C. Formation of Fe(III) oxyhydroxide colloids in freshwater and brackish seawater, with incorporation of phosphate and calcium. *Geochimica et Cosmochimica Acta*, 66(5):745–758, 2002.
- Hagy, J. D., Boynton, W. R., Keefe, C. W., and Wood, K. V. Hypoxia in Chesapeake Bay, 1950–2001: long-term change in relation to nutrient loading and river flow. *Estuaries*, 27(4):634–658, 2004.
- Hartzell, J. L., Jordan, T. E., and Cornwell, J. C. Phosphorus burial in sediments along the salinity gradient of the Patuxent River, a subestuary of the Chesapeake Bay (USA). *Estuaries and Coasts*, 33(1):92–106, 2010.
- Hartzell, J. L., Jordan, T. E., and Cornwell, J. C. Phosphorus Sequestration in Sediments Along the Salinity Gradients of Chesapeake Bay Subestuaries. *Estuaries and Coasts*, pages 1–19, 2017.
- Helder, W. and De Vries, R. An automatic phenol-hypochlorite method for the determination of ammonia in sea-and brackish waters. *Netherlands Journal of Sea Research*, 13(1):154–160, 1979.
- Helz, G. R., Sinex, S. A., Ferri, K. L., and Nichols, M. Processes controlling Fe, Mn and Zn in sediments of northern Chesapeake Bay. *Estuarine, Coastal and Shelf Science*, 21(1):1–16, 1985.
- Hirschberg, D. J. and Schubel, J. R. Recent geochemical history of flood deposits in the northern Chesapeake Bay. *Estuarine and Coastal Marine Science*, 9(6), 1979.
- Hsu, T.-W., Jiang, W.-T., and Wang, Y. Authigenesis of vivianite as influenced by methane-induced sulfidization in cold-seep sediments off southwestern Taiwan. *Journal of Asian Earth Sciences*, 89(August 2014):88–97, 2014.
- Huettel, M., Ziebis, W., Forster, S., and Luther Iii, G. Advective transport affecting metal and nutrient distributions and interfacial fluxes in permeable sediments. *Geochimica et Cosmochimica Acta*, 62(4):613–631, 1998.
- Huettel, M. and Webster, I. T. Porewater flow in permeable sediments. *The benthic boundary layer: transport processes and biogeochemistry*, pages 144–179, 2001.

- Hyacinthe, C. and Van Cappellen, P. An authigenic iron phosphate phase in estuarine sediments: composition, formation and chemical reactivity. *Marine Chemistry*, 91(1-4):227–251, 2004.
- Jensen, H. S. and Thamdrup, B. Iron-bound phosphorus in marine sediments as measured by bicarbonate-dithionite extraction. *Hydrobiologia*, 253(1-3):47–59, 1993.
- Jensen, S., Mortensen, P. B., Andersen, F., Rasmussen, E., and Jensen, A. Phosphorus cycling in a coastal marine sediment, Aarhus Bay, Denmark. *Limnology and Oceanography*, 40(5):908–917, 1995.
- Jilbert, T. and Slomp, C. P. Iron and manganese shuttles control the formation of authigenic phosphorus minerals in the euxinic basins of the Baltic Sea. *Geochimica et Cosmochimica Acta*, 107:155–169, 2013.
- Jørgensen, B. B. The sulfur cycle of a coastal marine sediment (Limfjorden, Denmark). *Limnology and Oceanography*, 22(5):814–832, 1977.
- Jørgensen, B. B. Bacteria and marine biogeochemistry. In *Marine geochemistry*, pages 169–206. Springer, 2006.
- Karlsson, O. M., Jonsson, P. O., Lindgren, D., Malmaeus, J. M., and Stehn, A. Indications of recovery from hypoxia in the inner Stockholm archipelago. *Ambio*, 39(7):486–495, 2010.
- Kemp, W. M., Boynton, W. R., Adolf, J. E., Boesch, D. F., Boicourt, W. C., Brush, G., Cornwell, J. C., Fisher, T. R., Glibert, P. M., Hagy, J. D., et al. Eutrophication of Chesapeake Bay: historical trends and ecological interactions. *Marine Ecology Progress Series*, 303:1–29, 2005.
- Kemp, W., Testa, J., Conley, D., Gilbert, D., and Hagy, J. Temporal responses of coastal hypoxia to nutrient loading and physical controls. *Biogeosciences*, 6(12):2985–3008, 2009.
- Ko, F.-C. and Baker, J. E. Seasonal and annual loads of hydrophobic organic contaminants from the Susquehanna River basin to the Chesapeake Bay. *Marine Pollution Bulletin*, 48(9-10):840–851, 2004.
- Kostka, J. E. and Luther, G. W. Partitioning and speciation of solid phase iron in saltmarsh sediments. *Geochimica et Cosmochimica Acta*, 58(7):1701–1710, 1994.
- Kraal, P. and Slomp, C. P. Rapid and extensive alteration of phosphorus speciation during oxic storage of wet sediment samples. *PloS one*, 9(5):e96859, 2014.
- Kraal, P., Slomp, C. P., Forster, A., Kuypers, M. M., and Sluijs, A. Pyrite oxidation during sample storage determines phosphorus fractionation in carbonate-poor anoxic sediments. *Geochimica et Cosmochimica Acta*, 73(11):3277–3290, 2009.
- Kraal, P., Dijkstra, N., Behrends, T., and Slomp, C. P. Phosphorus burial in sediments of the sulfidic deep Black Sea: Key roles for adsorption by calcium carbonate and apatite authigenesis. *Geochimica et Cosmochimica Acta*, 204(February):140–158, 2017.
- Kritzberg, E. and Ekström, S. Increasing iron concentrations in surface waters-a factor behind brownification? *Biogeosciences*, 9(4):1465, 2012.

- Krom, M. D. and Berner, R. A. Adsorption of phosphate in anoxic marine sediments. *Limnology and oceanography*, 25(5):797–806, 1980.
- Lenstra, W. K., Egger, M., van Helmond, N. A. G. M., Kritzberg, E., Conley, D. J., and Slomp, C. P. Variations in river input of iron impact sedimentary phosphorus burial in an oligotrophic estuary. in prep.
- Li, W., Joshi, S. R., Hou, G., Burdige, D. J., Sparks, D. L., and Jaisi, D. P. Characterizing Phosphorus Speciation of Chesapeake Bay Sediments Using Chemical Extraction, ^{31}P NMR, and X-ray Absorption Fine Structure Spectroscopy. *Environmental Science & Technology*, 49(1): 203–211, 2015.
- Libes, S. *Introduction to marine biogeochemistry*. Academic Press, 2011.
- Liu, R. and Zhao, D. In situ immobilization of Cu (II) in soils using a new class of iron phosphate nanoparticles. *Chemosphere*, 68(10):1867–1876, 2007.
- McGlathery, K. J., Sundbäck, K., and Anderson, I. C. Eutrophication in shallow coastal bays and lagoons: the role of plants in the coastal filter. *Marine Ecology Progress Series*, 348:1–18, 2007.
- Meier, H. E., Kjellström, E., and Graham, L. P. Estimating uncertainties of projected Baltic Sea salinity in the late 21st century. *Geophysical Research Letters*, 33(15):1–4, 2006.
- Middelburg, J. J. and Levin, L. A. Coastal hypoxia and sediment biogeochemistry. *Biogeosciences*, 6(7):1273–1293, 2009.
- Morse, J. and Luther III, G. Chemical influences on trace metal-sulfide interactions in anoxic sediments. *Geochimica et Cosmochimica Acta*, 63(19-20):3373–3378, 1999.
- Mort, H. P., Adatte, T., Föllmi, K. B., Keller, G., Steinmann, P., Matera, V., Berner, Z., and Stüben, D. Phosphorus and the roles of productivity and nutrient recycling during oceanic anoxic event 2. *Geology*, 35(6):483–486, 2007.
- Mort, H. P., Slomp, C. P., Gustafsson, B. G., and Andersen, T. J. Phosphorus recycling and burial in Baltic Sea sediments with contrasting redox conditions. *Geochimica et Cosmochimica Acta*, 74(4):1350–1362, 2010.
- Murphy, T. P., Lawson, A., Kumagai, M., and Nalewajko, C. Release of phosphorus from sediments in Lake Biwa. *Limnology*, 2(2):119–128, 2001.
- Najjar, R. G., Pyke, C. R., Adams, M. B., Breitburg, D., Hershner, C., Kemp, M., Howarth, R., Mulholland, M. R., Paolisso, M., Secor, D., Sellner, K., Wardrop, D., and Wood, R. Potential climate-change impacts on the Chesapeake Bay. *Estuarine, Coastal and Shelf Science*, 86(1): 1–20, 2010.
- National Oceanic and Atmospheric Administration. NOAA, National Centers for Environmental Information. <https://maps.ngdc.noaa.gov/viewers/bathymetry/>, Accessed April 2018.

- Nembrini, G. P., Capobianco, J. A., Viel, M., and Williams, A. F. A Mössbauer and chemical study of the formation of vivianite in sediments of Lago Maggiore (Italy). *Geochimica et Cosmochimica Acta*, 47(8):1459–1464, 1983.
- Ning, W., Ghosh, A., Jilbert, T., Slomp, C. P., Khan, M., Nyberg, J., Conley, D. J., and Filipsson, H. L. Evolving coastal character of a Baltic Sea inlet during the Holocene shoreline regression: impact on coastal zone hypoxia. *Journal of paleolimnology*, 55(4):319–338, 2016.
- Nixon, S., Ammerman, J., Atkinson, L., Berounsky, V., Billen, G., Boicourt, W., Boynton, W., Church, T., Ditoro, D., Elmgren, R., et al. The fate of nitrogen and phosphorus at the land-sea margin of the North Atlantic Ocean. *Biogeochemistry*, 35(1):141–180, 1996.
- Nriagu, J. O. Stability of vivianite and ion-pair formation in the system $\text{Fe}_3(\text{PO}_4)_2\text{--H}_3\text{PO}_4\text{--H}_2\text{O}$. *Geochimica et Cosmochimica Acta*, 36(4):459–470, 1972.
- O’Connell, D. W., Jensen, M. M., Jakobsen, R., Thamdrup, B., Andersen, T. J., Kovacs, A., and Hansen, H. C. B. Vivianite formation and its role in phosphorus retention in Lake Ørn, Denmark. *Chemical geology*, 409:42–53, 2015.
- O’Keefe, J. A. *Sediment biogeochemistry across the Patuxent River estuarine gradient: Geochronology and iron-sulfur-phosphorus interactions*. University of Maryland, College Park, 2007.
- Palinkas, C. M., Halka, J. P., Li, M., Sanford, L. P., and Cheng, P. Sediment deposition from tropical storms in the upper Chesapeake Bay: Field observations and model simulations. *Continental Shelf Research*, 86(C):6–16, 2014.
- Palinkas, C. M., Sanford, L. P., and Koch, E. W. Influence of Shoreline Stabilization Structures on the Nearshore Sedimentary Environment in Mesohaline Chesapeake Bay. *Estuaries and Coasts*, pages 1–14, 2017.
- Palinkas, C. and Nittrouer, C. Modern sediment accumulation on the Po shelf, Adriatic Sea. *Continental Shelf Research*, 27(3-4):489–505, 2007.
- Petersen, G., Chesters, G., and Lee, G. Quantitative determination of calcite and dolomite in soils. *European Journal of Soil Science*, 17(2):328–338, 1966.
- Poulton, S. W. and Canfield, D. E. Development of a sequential extraction procedure for iron: Implications for iron partitioning in continentally derived particulates. *Chemical Geology*, 214 (3-4):209–221, 2005.
- Puttonen, I., Mattila, J., Jonsson, P., Karlsson, O. M., Kohonen, T., Kotilainen, A., Lukkari, K., Malmaeus, J. M., and Rydin, E. Distribution and estimated release of sediment phosphorus in the northern Baltic Sea archipelagos. *Estuarine, Coastal and Shelf Science*, 145:9–21, 2014.
- Qi, C., Zhu, Y.-J., Lu, B.-Q., Wu, J., and Chen, F. Amorphous magnesium phosphate flower-like hierarchical nanostructures: microwave-assisted rapid synthesis using fructose 1,6-bisphosphate trisodium salt as an organic phosphorus source and application in protein adsorption. *RSC Adv.*, 5(19):14906–14915, 2015.

- Rabalais, N. N., Turner, R. E., Díaz, R. J., and Justić, D. Global change and eutrophication of coastal waters. *ICES Journal of Marine Science*, 66(7):1528–1537, 2009.
- Rahman, M. M., Salleh, M. A. M., Rashid, U., Ahsan, A., Hossain, M. M., and Ra, C. S. Production of slow release crystal fertilizer from wastewaters through struvite crystallization - A review. *Arabian Journal of Chemistry*, 7(1):139–155, 2014.
- Raiswell, R., Buckley, F., Berner, R. A., and Anderson, T. Degree of pyritization of iron as a paleoenvironmental indicator of bottom-water oxygenation. *Journal of Sedimentary Research*, 58(5), 1988.
- Raiswell, R. and Canfield, D. E. Sources of iron for pyrite formation in marine sediments. *American Journal of Science*, 298(3):219–245, 1998.
- Raiswell, R. and Canfield, D. E. The iron biogeochemical cycle past and present. *Geochemical perspectives*, 1(1):1–2, 2012.
- Roden, E. and Edmonds, J. Phosphate mobilization in iron-rich anaerobic sediments: microbial Fe (III) oxide reduction versus iron-sulfide formation. *Archiv für Hydrobiologie*, 139(3):347–378, 1997.
- Roden, E. E. and Tuttle, J. H. Inorganic sulfur turnover in oligohaline estuarine sediments. *Biogeochemistry*, 22(2):81–105, 1993.
- Rothe, M., Frederichs, T., Eder, M., Kleeberg, A., and Hupfer, M. Evidence for vivianite formation and its contribution to long-term phosphorus retention in a recent lake sediment: A novel analytical approach. *Biogeosciences*, 11(18):5169–5180, 2014.
- Rothe, M., Kleeberg, A., Grüneberg, B., Friese, K., Pérez-Mayo, M., and Hupfer, M. Sedimentary sulphur: iron ratio indicates vivianite occurrence: a study from two contrasting freshwater systems. *Plos one*, 10(11):e0143737, 2015.
- Rothe, M., Kleeberg, A., and Hupfer, M. The occurrence, identification and environmental relevance of vivianite in waterlogged soils and aquatic sediments. *Earth-Science Reviews*, 158:51–64, 2016.
- Ruttenberg, K. C. . Development of a Sequential Extraction Method for Different Forms of Phosphorus in Marine Sediments. *Limnology and Oceanography*, 37(7):1460–1482, 1992.
- Ruttenberg, K. Reassessment of the oceanic residence time of phosphorus. *Chemical Geology*, 107 (3-4):405–409, 1993.
- Ruttenberg, K. The global phosphorus cycle. *Treatise on geochemistry*, 8:682, 2003.
- Ruttenberg, K. The global phosphorus cycle. 2014.
- Rydin, E., Malmaeus, J. M., Karlsson, O. M., and Jonsson, P. Phosphorus release from coastal Baltic Sea sediments as estimated from sediment profiles. *Estuarine, Coastal and Shelf Science*, 92(1):111–117, 2011.

- Sanford, L. P. Wave-forced resuspension of upper Chesapeake Bay muds. *Estuaries*, 17(1):148–165, 1994.
- Sapota, T., Aldahan, A., and Al-Aasm, I. S. Sedimentary facies and climate control on formation of vivianite and siderite microconcretions in sediments of Lake Baikal, Siberia. *Journal of Paleolimnology*, 36(3):245–257, 2006.
- Savenko, A. Precipitation of phosphate with iron hydroxide forming by mixing of submarine hydrothermal solutions and the sea water (on the base of experimental data). *Geochemistry International*, 9:1383–1389, 1995.
- Schenau, S. and De Lange, G. A novel chemical method to quantify fish debris in marine sediments. *Limnology and Oceanography*, 45(4):963–971, 2000.
- Schulz, H. D. and Zabel, M. *Marine geochemistry*, volume 2. Springer, 2006.
- Selman, M., Greenhalgh, S., Diaz, R., and Sugg, Z. Eutrophication and hypoxia in coastal areas: a global assessment of the state of knowledge. *WRI Policy Note*, (1):1–6, 2008.
- Slomp, C. P. Phosphorus cycling in the estuarine and coastal zones. Elsevier/Academic Press, 2011.
- Slomp, C. P., Epping, E. H., Helder, W., and Raaphorst, W. V. A key role for iron-bound phosphorus in authigenic apatite formation in North Atlantic continental platform sediments. *Journal of marine Research*, 54(6):1179–1205, 1996.
- Soetaert, K., Herman, P. M., and Middelburg, J. J. A model of early diagenetic processes from the shelf to abyssal depths. *Geochimica et Cosmochimica Acta*, 60(6):1019–1040, 1996.
- Staver, L. W., Staver, K. W., and Stevenson, J. C. Nutrient inputs to the Choptank River estuary: Implications for watershed management. *Estuaries*, 19(2B):342–358, 1996.
- Strickland, J. D. and Parsons, T. R. A practical handbook of seawater analysis. 1972.
- Taylor, K. G., Hudson-Edwards, K. A., Bennett, A. J., and Vishnyakov, V. Early diagenetic vivianite $[\text{Fe}_3(\text{PO}_4)_2 \cdot 8 \text{H}_2\text{O}]$ in a contaminated freshwater sediment and insights into zinc uptake: A μ -EXAFS, μ -XANES and Raman study. *Applied Geochemistry*, 23(6):1623–1633, 2008.
- Testa, J. M. and Kemp, W. M. Spatial and Temporal Patterns of Winter–Spring Oxygen Depletion in Chesapeake Bay Bottom Water. *Estuaries and Coasts*, 37(6):1432–1448, 2014.
- Timothy, R., Yoshiaki, M., and Carol, M. A manual of chemical and biological methods for seawater analysis. *Pergamon Press. Inc*, 395:475–490, 1984.
- Vahtera, E., Conley, D. J., Gustafsson, B. G., Kuosa, H., Pitkänen, H., Savchuk, O. P., Tamminen, T., Viitasalo, M., Voss, M., Wasmund, N., et al. Internal ecosystem feedbacks enhance nitrogen-fixing cyanobacteria blooms and complicate management in the Baltic Sea. *AMBIO: A journal of the Human Environment*, 36(2):186–194, 2007.

- Van Cappellen, P. and Ingall, E. D. Benthic phosphorus regeneration, net primary production, and ocean anoxia: a model of the coupled marine biogeochemical cycles of carbon and phosphorus. *Paleoceanography*, 9(5):677–692, 1994.
- Van Santvoort, P. J. M., De Lange, G., Thomson, J., Colley, S., Meysman, F., and Slomp, C. Oxidation and origin of organic matter in surficial Eastern Mediterranean hemipelagic sediments. *Aquatic Geochemistry*, 8(3):153–175, 2002.
- Voss, M., Emeis, K.-C., Hille, S., Neumann, T., and Dippner, J. Nitrogen cycle of the Baltic Sea from an isotopic perspective. *Global biogeochemical cycles*, 19(3), 2005.
- Williams, K. F. and Reed, L. A. Appraisal of stream sedimentation in the Susquehanna River basin. Technical report, US Government Printing Office, 1972.
- Zhang, Q., Brady, D. C., and Ball, W. P. Long-term seasonal trends of nitrogen, phosphorus, and suspended sediment load from the non-tidal Susquehanna River Basin to Chesapeake Bay. *Science of the total environment*, 452:208–221, 2013.

Appendix A ^{210}Pb ET5.1

The excess ^{210}Pb profile shows a constant decline with small variations. Also, the sand fraction increases gradually pointing to no sudden changes in sediment deposition at ET5.1.

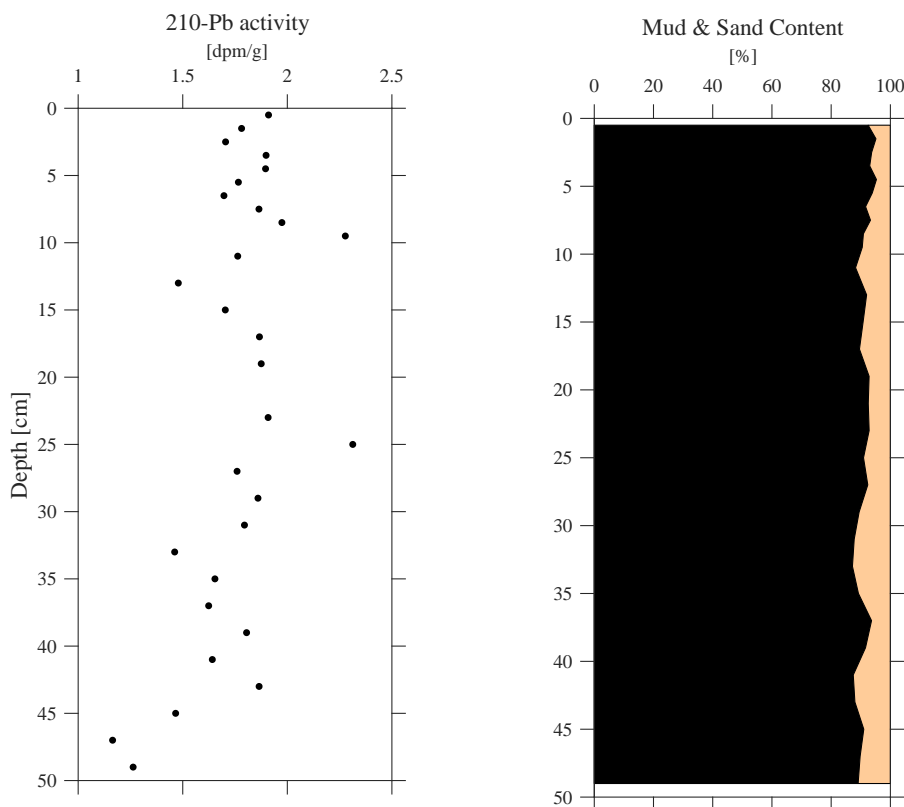


Figure 19: ^{210}Pb depth profile and sedimentary composition at ET5.1; the mud fraction is presented in black and the sand fraction in orange

Appendix B Additional porewater profiles and saturation indices

Zoomed in porewater profiles for Strömmen are presented in Figure 20, allowing to see trends, which were hidden in Figure 7 due to higher concentrations at the Chesapeake Bay sites.

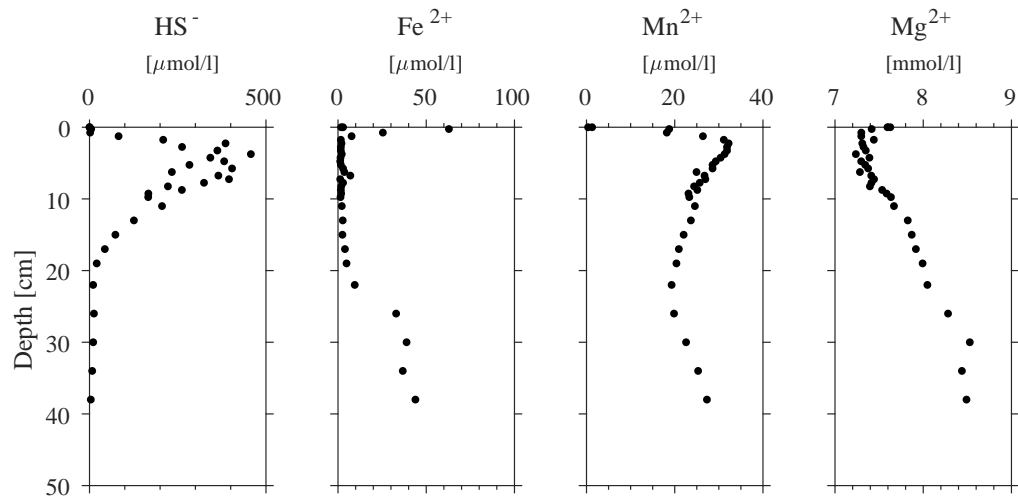


Figure 20: Zommed in porewater profiles (sulfide, ferrous iron, manganese and magnesium) for Strömmen

The porewater trends of Cl^- and K^+ are displayed in Figure 21. At CB2.2 the intrusion of fresher water becomes visible by a decline in Cl^- at 10 cm depth.

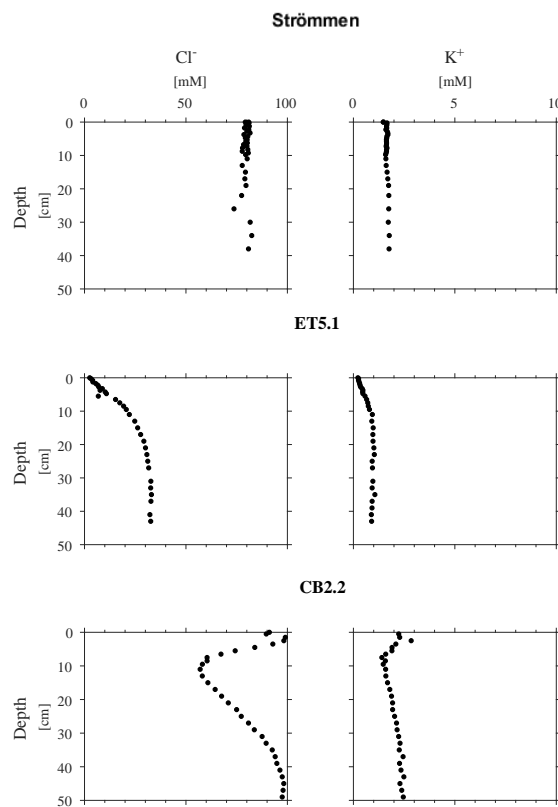


Figure 21: Supplement porewater profiles

Table 6 displays the saturation indices for Strömmen of four minerals able to bury P. The applied

Table 6: Saturation indices for hydroxylapatite, vivianite, MnHPO_4 and struvite at Strömmen.

Depth (cm)	SI Vivianite	SI MnHPO_4	SI Hydroxylapatite	SI Struvite
0	-3.446	-0.936	1.327	-5.311
0.25	5.345	3.188	8.751	-2.117
0.75	3.571	3.072	7.599	-2.435
1.25	-100.903	3.152	8.635	-1.819
1.75	-102.845	2.925	8.055	-1.819
2.25	-104.608	2.681	8.022	-1.9
2.75	-103.462	2.862	8.135	-1.672
3.25	-104.35	2.744	8.1197	-1.719
3.75	-103.687	2.693	7.323	-1.838
4.25	-102.86	2.812	7.395	-1.942
4.75	-103.151	2.63	7.413	-1.872
5.25	-102.268	2.891	7.502	-1.826
5.75	-103.255	2.753	7.567	-1.72
6.25	-101.701	2.913	7.538	-1.767
6.75	-102.881	2.794	7.675	-1.659
7.25	-103.155	2.762	7.67	-1.655
7.75	-102.555	2.84	7.773	-1.614
8.25	-101.479	2.98	7.801	-1.661
8.75	-101.967	2.918	7.837	-1.582
9.25	-100.659	3.066	7.879	-1.576
9.75	-100.66	3.071	7.913	-1.567
11	-101.214	3.029	7.976	-1.511
13	-99.781	3.182	8.028	-1.479
15	-98.178	3.314	8.08	-1.441
17	-96.343	3.428	8.167	-1.481
19	-93.113	3.53	8.189	-1.457
22	1.425	3.539	8.164	-1.429
26	3.646	3.472	8.144	-1.527
30	3.892	3.497	8.174	-1.532
34	3.829	3.528	8.297	-1.594
38	4.034	3.5	8.246	-1.572

equilibrium constants were corrected for temperature. No pH measurements were available so that based on DIC and general sediment trends a pH was estimated. Hydroxylapatite and MnHPO_4 were supersaturated for the whole sediment, while struvite was undersaturated. Vivianite was supersaturated below 22 cm, coinciding with the depth of HPO_4^{2-} removal from the porewater and increase in Fe^{2+} concentration. Vivianite is also supersaturated in the first 0.75 cm, probably due to high Fe^{2+} and HPO_4^{2-} concentrations.

Table 7 shows the saturation indices for ET5.1 for hydroxylapatite, vivianite, MnHPO_4 and struvite. The applied equilibrium constants were corrected for temperature. No pH measurements were available so that based on DIC and general sediment trends a pH was estimated. Vivianite and MnHPO_4 were supersaturated in all sediment intervals. Hydroxylapatite was supersaturated below 1.25 cm and struvite was undersaturated for all sediment intervals.

Table 7: Saturation indices for hydroxylapatite, vivianite, MnHPO_4 and struvite at ET5.1

Depth (cm)	SI Vivianite	SI MnHPO_4	SI Hydroxylapatite	SI Struvite
0	-34.16	1.44	-3.01	-20.23
0.25	0.24	2.59	-2.31	-5.75
0.75	2.341	3.23	-0.50	-4.88
1.25	3.20	3.56	0.74	-4.28
1.75	4.95	4.2	2.72	-3.67
2.25	4.73	4.13	2.60	-3.59
2.75	5.73	4.46	3.84	-16.31
3.25	5.15	4.54	4.33	-278
3.75	5.92	4.56	4.58	-2.71
4.25	5.68	4.42	4.07	-2.65
4.75	2.42	3.34	0.82	-3.78
5.5	6.34	4.67	5.06	-15.69
6.5	6.51	4.68	5.21	-2.30
7.5	6.46	4.64	5.23	-2.28
8.5	6.60	4.70	5.30	-2.22
9.5	6.47	4.66	5.31	-2.17
11	4.1	3.82	2.92	-2.99
13	3.92	3.67	2.44	-3.09
15	5.64	4.40	4.73	-2.31
17	6.30	4.57	5.24	-2.15
19	6.48	4.63	5.50	-2.05
21	6.55	4.67	5.66	-2.01
23	6.60	4.69	5.77	-1.98
25	6.64	4.63	5.62	-2.00
27	6.58	4.57	5.60	-2.00
31	6.37	4.42	5.30	-2.08
33	5.94	4.26	4.64	-2.29
35	6.25	4.43	5.09	-2.20
37	6.50	4.51	5.25	-2.12
39	6.62	4.51	5.40	-2.09
41	6.32	4.38	5.05	-2.17
43	5.80	4.15	4.53	-2.37

Table 8 shows the saturation indices for CB2.2 for hydroxylapatite, vivianite, MnHPO_4 and struvite. The applied equilibrium constants were corrected for temperature. No pH measurements were available so that based on DIC and general sediment trends a pH was estimated. MnHPO_4 was supersaturated in all sediment intervals. Vivianite is supersaturated between 2.5 and 9.5 cm. MnHPO_4 was supersaturated in all sediment intervals. Hydroxylapatite was supersaturated in all sediment intervals, except in the first 0.75 cm, at 11 and 13 cm depth and struvite was undersaturated for all intervals.

Table 8: Saturation indices for hydroxylapatite, vivianite, MnHPO_4 and struvite at CB2.2. HPO_4^{2-} measurement missing for 6.5 cm.

Depth (cm)	SI Vivianite	SI MnHPO_4	SI Hydroxylapatite	SI Struvite
0	-34.27	0.27	2.63	-5.40
0.5	-4.58	0.21	2.39	-4.49
1.5	-1.3	3.03	3.96	-3.68
2.5	1.27	3.00	3.82	-3.78
3.5	-0.02	2.81	1.37	-4.20
4.5	1.78	3.11	2.37	-3.30
5.5	2.14	3.11	2.37	-3.84
6.5				
7.5	4.07	4.00	3.55	-3.28
8.5	3.80	3.85	3.18	-3.38
9.5	1.96	3.22	1.26	-3.94
11	-2.16	2.75	-0.05	-4.42
13	-2.56	2.54	-0.43	-4.57
15	0.37	3.33	2.43	-3.62
17	-0.52	3.46	3.48	-3.33
19	-32.80	3.51	3.92	-3.25
21	-32.35	3.65	4.53	-3.26
23	-0.25	3.63	4.46	-3.27
25	-2.45	3.68	4.66	-3.16
27	-3.08	3.71	4.88	-2.95
29	-2.20	3.75	5.19	-2.85
31	-31.91	3.83	5.53	-2.64
33	-31.85	3.86	5.69	-2.57
35	-1.91	3.91	5.83	-2.42
37	-2.06	3.88	5.78	-2.40
39	-1.27	3.78	5.39	-2.46
41	-0.72	3.65	4.87	-2.59
43	0.42	3.70	4.91	-2.54
45	-0.34	3.71	4.82	-2.53
47	1.38	3.69	4.68	-2.52
49	0.58	3.67	4.56	-2.50

Appendix C CDB fractions & Elemental ratios

Figure 22 presents the concentrations of HPO_4^{2-} (in red) and various cations in the CDB step of SEDEX. For Strömmen, no Mn is detectable. Generally, Mg concentrations are higher at Strömmen than the ones of the Chesapeake Bay sites. The presence of no Fe and Mn below 20 cm depth at CB2.2, implies that P extracted is not associated to Fe.

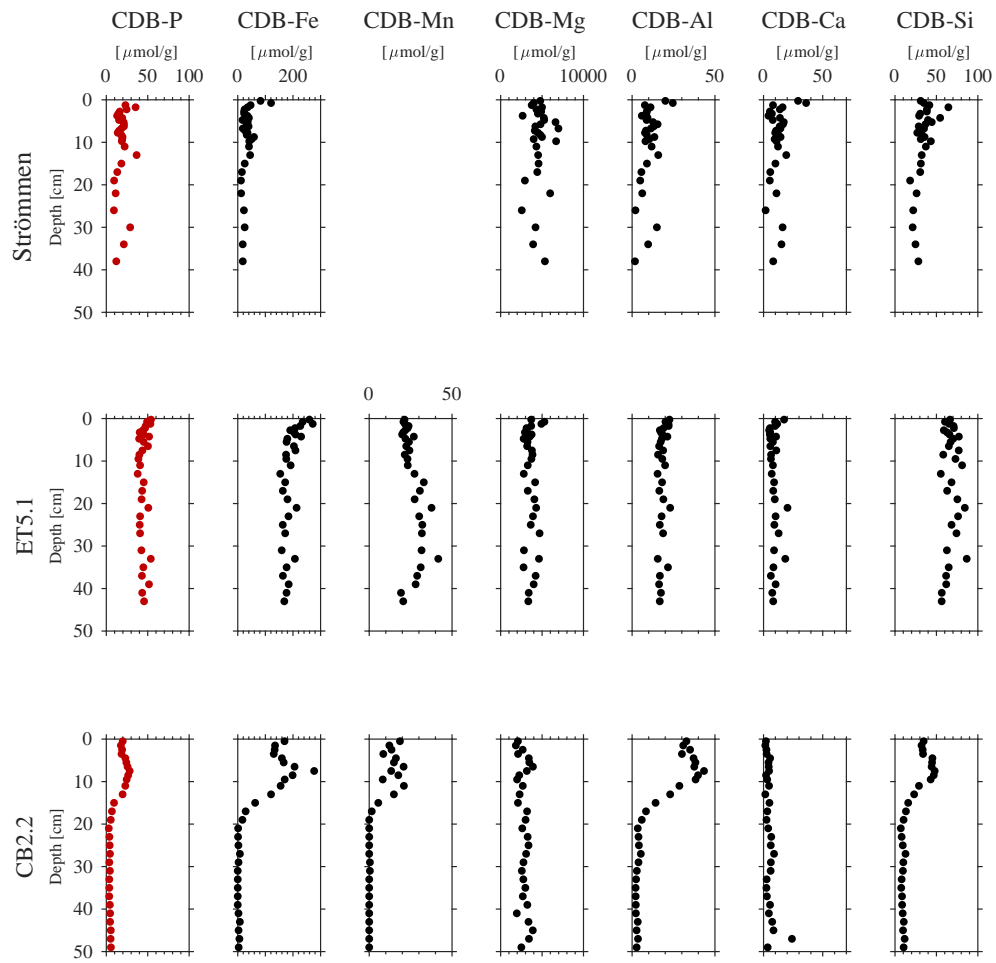


Figure 22: Elemental concentrations extracted in the CDB fraction of the SEDEX besides P

The ratios presented in Figure 23 are used in order to detect changes in the composition of the sediment. The change in composition can be either related to alteration in the input or changes in the elemental burial efficiency.

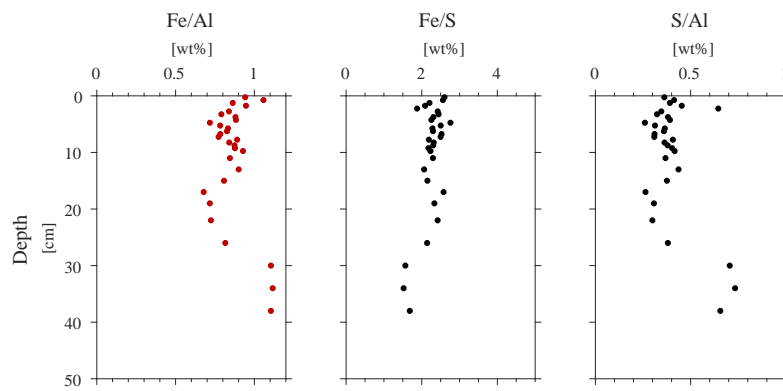


Figure 23: Fe/Al, Fe/S, and S/Al depth profiles at Strömmen

Appendix D P burial rates

Based on total P concentrations, P burial rates were calculated. Since no sediment accumulation rate was available for Strömmen, a more conservative and two progressive estimated rates were used, covering a range of reported values in the literature (Asmala et al., 2017; Rydin et al., 2011; Ning et al., 2016). The rates are summarized in Table 9. ET5.1 had the highest P burial rate, followed by CB2.2 and Strömmen (if for Strömmen the conservative estimate is used).

Table 9: P burial rates		
Site	Sediment accumulation rate [g/ cm ² yr]	P burial rate [g P/ m ² yr]
ET5.1	0.61	1.25
CB2.2	0.62	0.68
Strömmen	0.63	0.60
	1	0.93
	2	1.86

The estimates of P burial rates for the Chesapeake Bay are higher than expected based on the relationship established between sediment accumulation rate and P burial in the Baltic Sea by Asmala et al. (2017).

Appendix E SEM-EDS images

E.1 Strömmen

Figure 24 shows an overview SEM image of the sediment interval at 30 cm depth at Strömmen. The yellow arrows indicate pyrite, which was identified via its shape and elemental spot analysis. The amount of pyrite present, reflects the high DOP determined via the solid phase extraction. A flat-shaped crystal enriched in Mg and Fe is shown in Figure 25. No significant amount of P is detected via the EDS, while the elemental map show that some P is associated with the flat crystals, which were common at 30 cm.

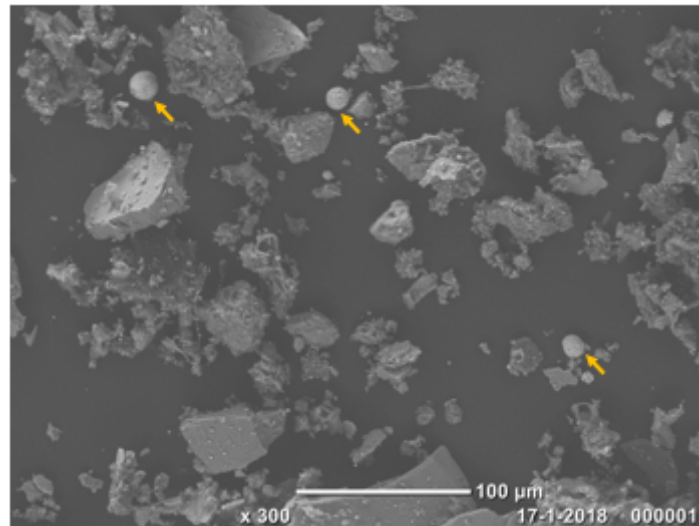


Figure 24: Overview SEM image of 30 cm sediment depth, Strömmen. Pyrite crystals indicated by yellow arrows

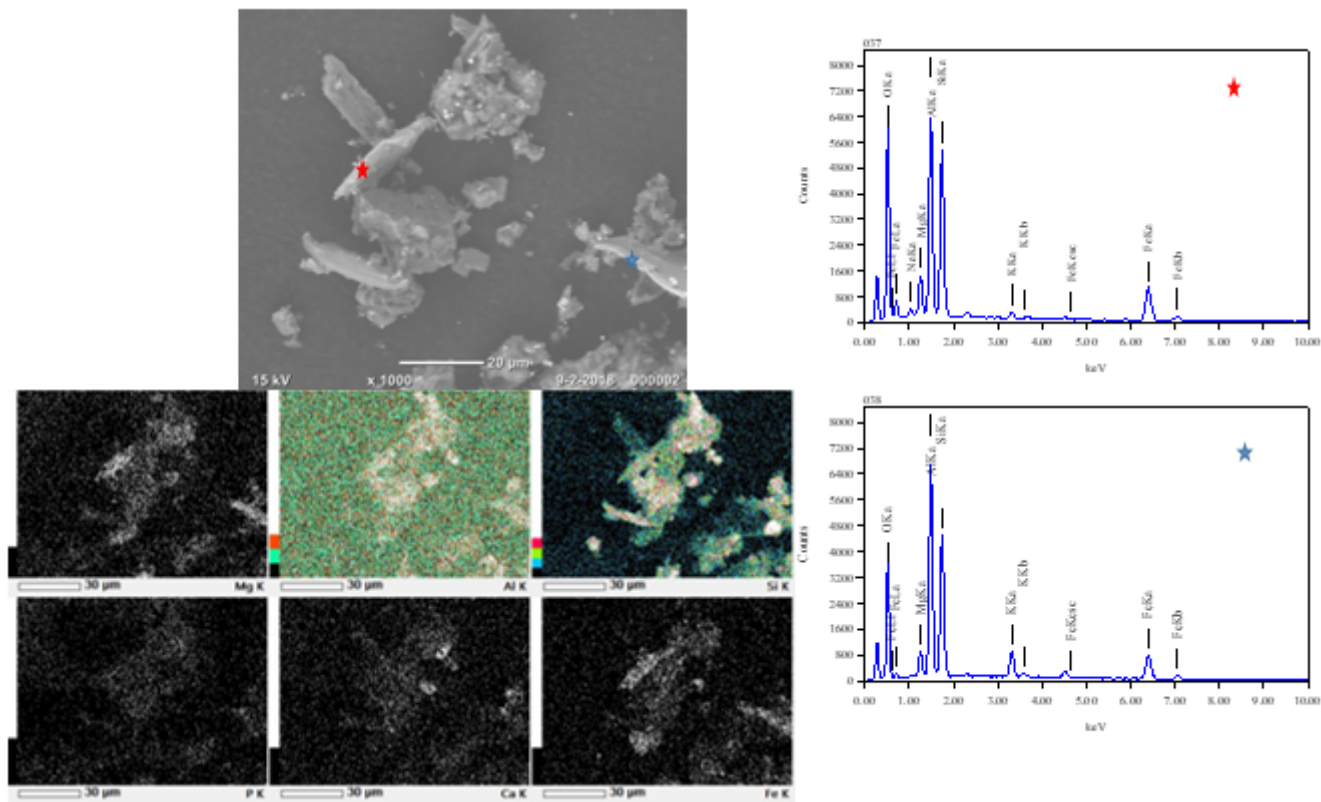
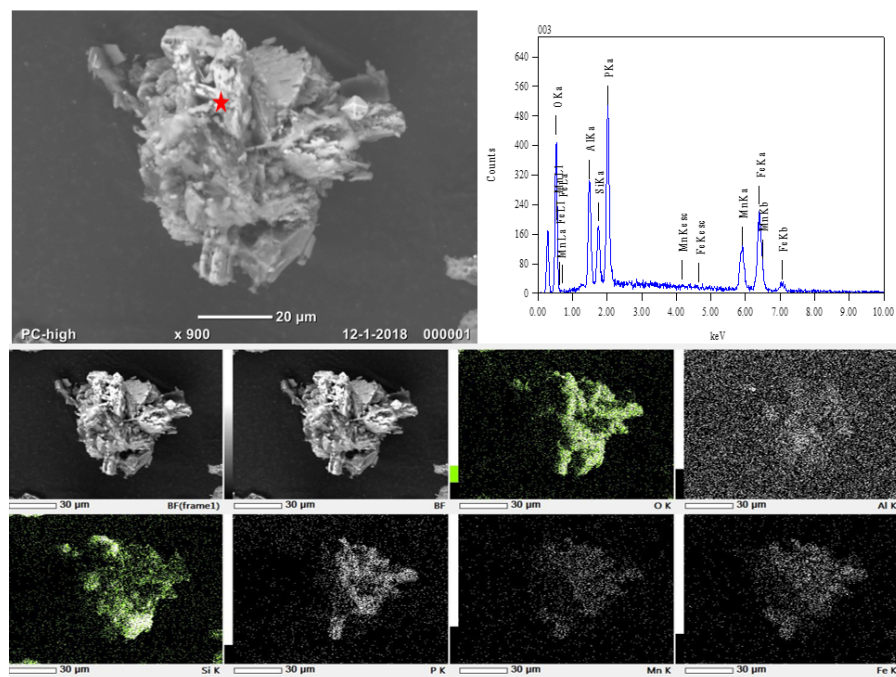


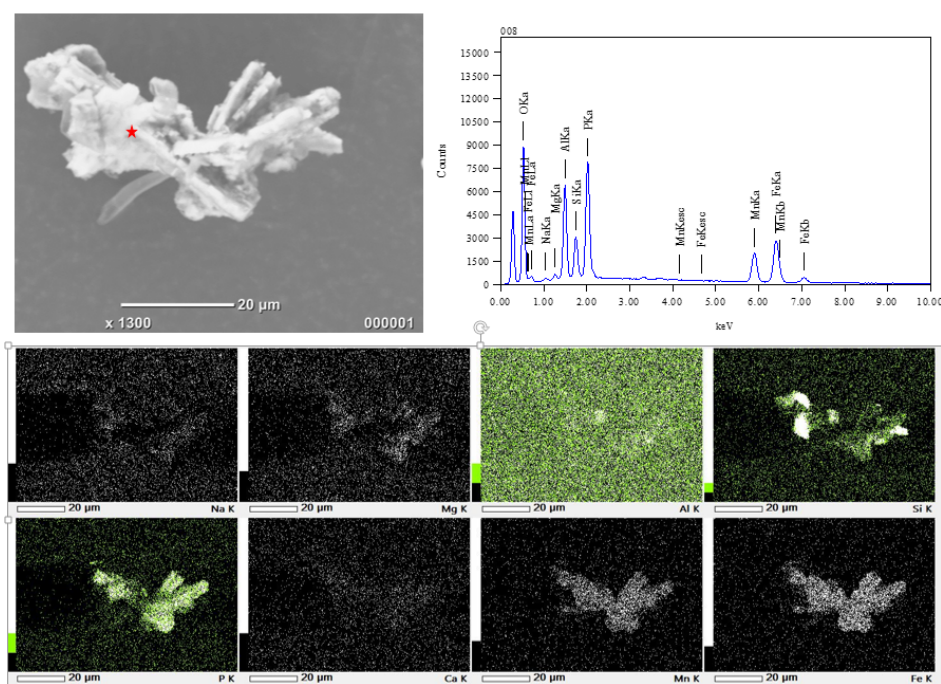
Figure 25: Mg and Fe enriched crystal at 30 cm depth, Strömmen

E.2 ET5.1

Further examples of vivianite like crystals at 5 and 30 cm depth at ET5.1 are presented in Figure 26. Both crystals are associated with Si-rich material, highlighting the often visible enrichment in organic material close to vivianite as reported by Rothe et al. (2016).



(a) 5 cm depth



(b) 30 cm depth

Figure 26: Crystals resembling vivianite at ET5.1 at two different depth intervals; the point of spot analyses is indicated by a red star

Table 10 summarizes the average elemental abundances and calculated ratios of the vivianite like crystals found at ET5.1 at various depths. Standard deviations are also provided and highlight the heterogeneity of the composition of the ferrous phosphates at the same depth (and even sometimes in the same crystal). All crystals are enriched in Mn.

Table 10: Relative elemental abundances in mol% and molar ratios in mol/mol as determined by SEM-EDS (n=number of measurements) for vivianite like crystals at depths of 5.5, 11 and 33 cm

	5.5 cm (n= 16)		11 cm (n=24cm)		30 cm (n=10)	
	Mean	ST. DEV	Mean	ST. DEV	Mean	ST. DEV
P	18.2	7.5	18.1	9.5	16.8	7.4
Fe	26.0	10.3	30.6	9.4	29.5	9.6
Mn	15.6	6.5	19.2	6.7	19.8	5.8
Mg	2.2	1.1	2.1	1.0	2.0	1.2
Si	15.3	14.2	12.1	12	12.9	12
Al	8.2	4.8	13.2	6.6	9.2	4.8
Fe/P	1.49	0.4	3.4	6.3	2.2	1.6
Mn/P	0.87	0.3	2.1	3.9	1.3	1.1
Mg/P	0.11	0.06	0.10	0.04	0.09	0.06
(Fe,Mn,Mg)/P	2.47	0.7	5.57	10.1	3.50	2.6
(Fe, Mn)/P	2.36	0.7	5.48	10.1	3.41	2.7

E.3 CB2.2

Figure 27 shows an overview SEM image at 29 cm depth at CB2.2, as well as the associated elemental maps measured by the EDS. A strong co-enrichment between S and Fe is visible, pointing towards the presence of pyrite. Additionally at the middle right side a coinciding enrichment in Ca and P is measured, suggesting the presence of apatite. Together detrital and authigenic apatite are responsible for about 40 % of total P burial at CB2.2.

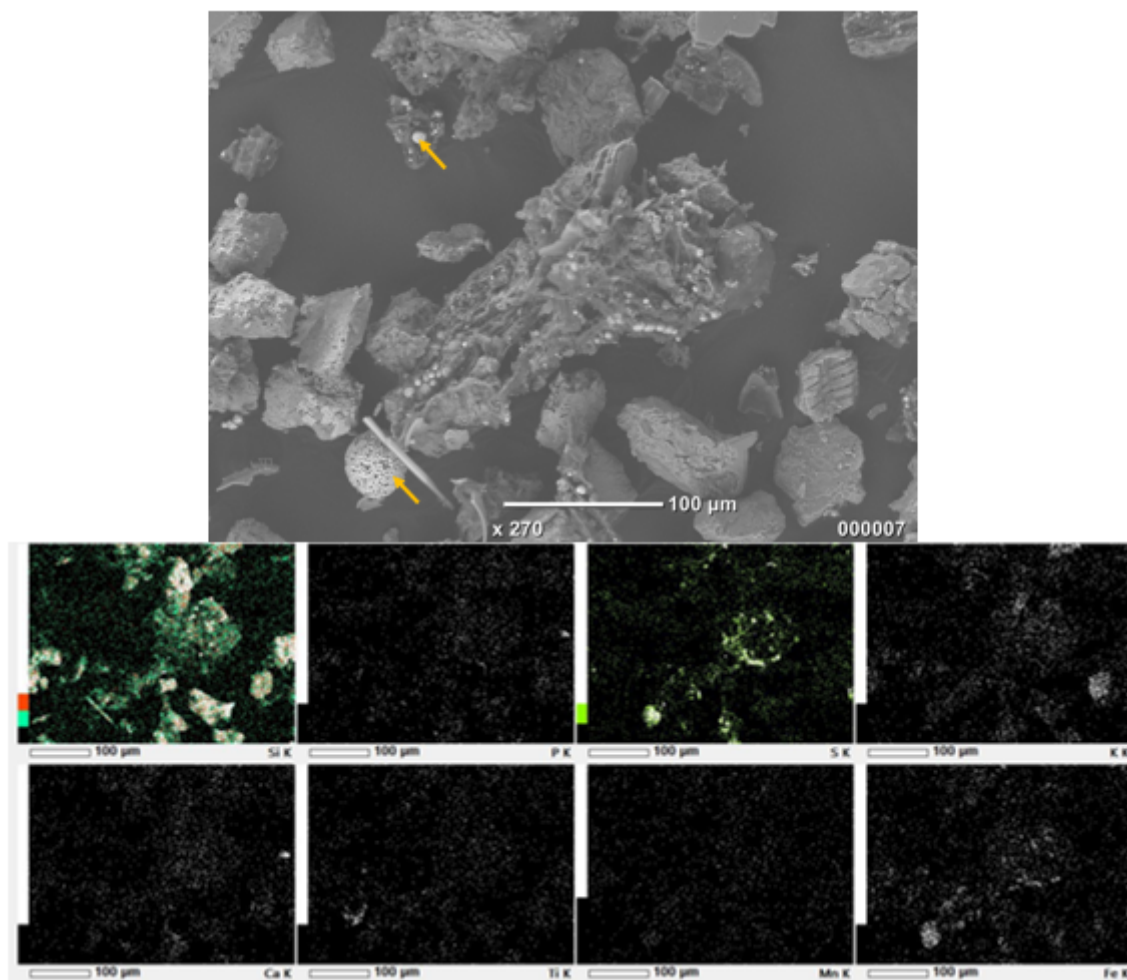


Figure 27: SEM image of CB2.2 at 29 cm indicating an enrichment in pyrite and possible apatite. Pyrite is indicated by yellow arrows.

Appendix F Additional μ XRF based correlation plots

Individual elemental correlation plots between P and Ca, Fe, Mn and Mg are shown in Figure 28. A strong correlation between Ca and P for the depth intervals at Strömmen becomes apparent (Figure 28a). This correlation is weaker at ET5.1, matching the solid phase extraction results. Apatite plays significant role in P burial at Strömmen but not at ET5.1.

The correlation between Fe and P is more pronounced at ET5.1 than at Strömmen, matching the significant Fe-bound P pool at ET5.1 (Figure 28b). Additionally, this highlights that Fe-bound P and vivianite plays a more important role in P burial at ET5.1 than at Strömmen.

No correlation between Mn and P is visible at Strömmen, while at ET5.1 a strong correlation is detected, suggesting potentially the formation of MnHPO_4 and Mn-enriched vivianite (Figure 28c). A visible correlation between Mg and P is only present at 22 and 30 cm, while the μ XRF images also show a link at 34 cm depth (Figure 28d). No link between Mg and P is visible at ET5.1.

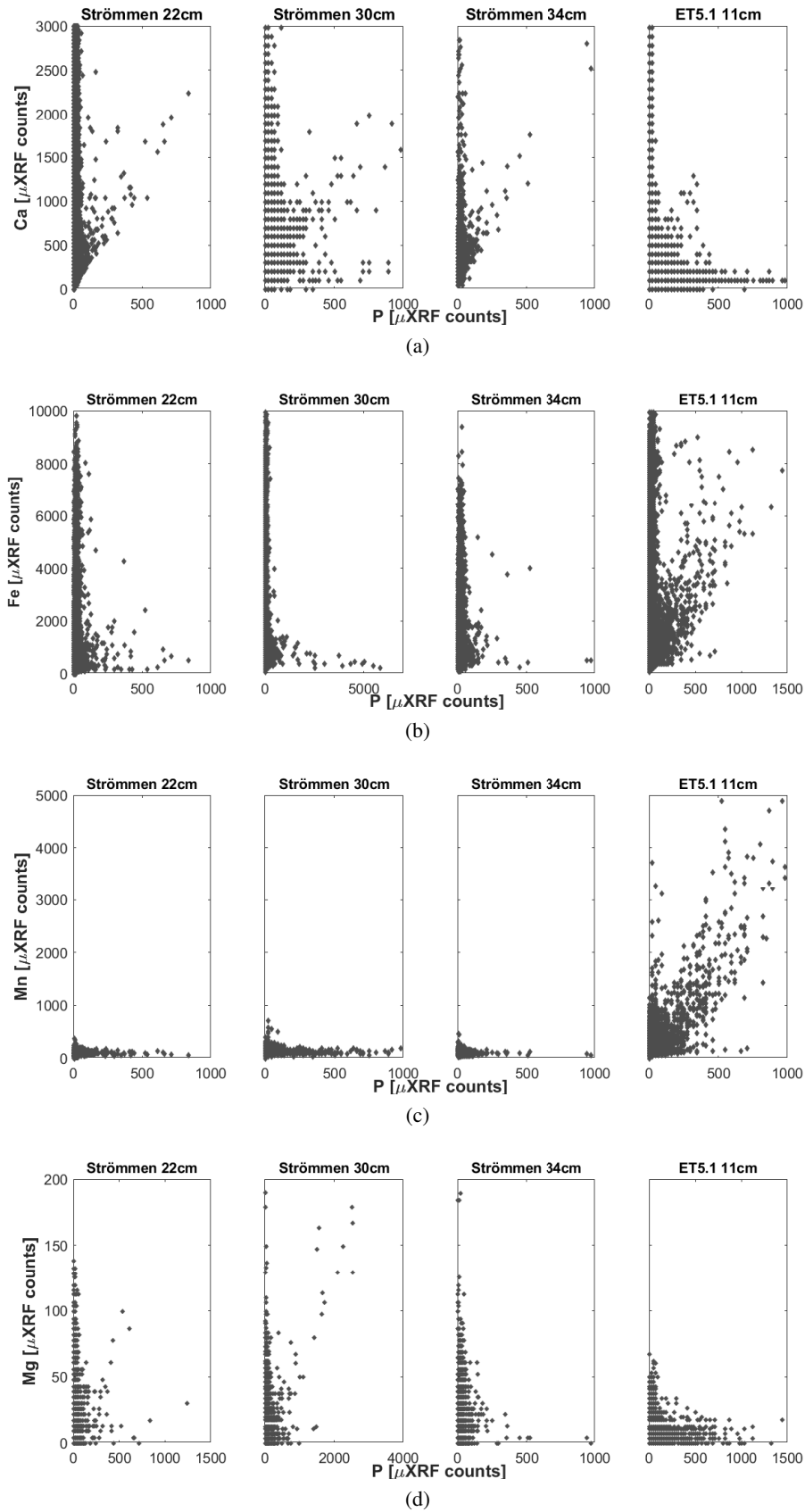


Figure 28: Additional μ XRF correlation plots for Ca, Fe, Mn, and Mg against P respectively

Cu to P has a random coinciding enrichment. Since Cu is a trace metal, and present only rarely no clear correlation is visible (Figure 29). No clear link between Zn enrichment and P is visible, while μ XRF images suggested this.

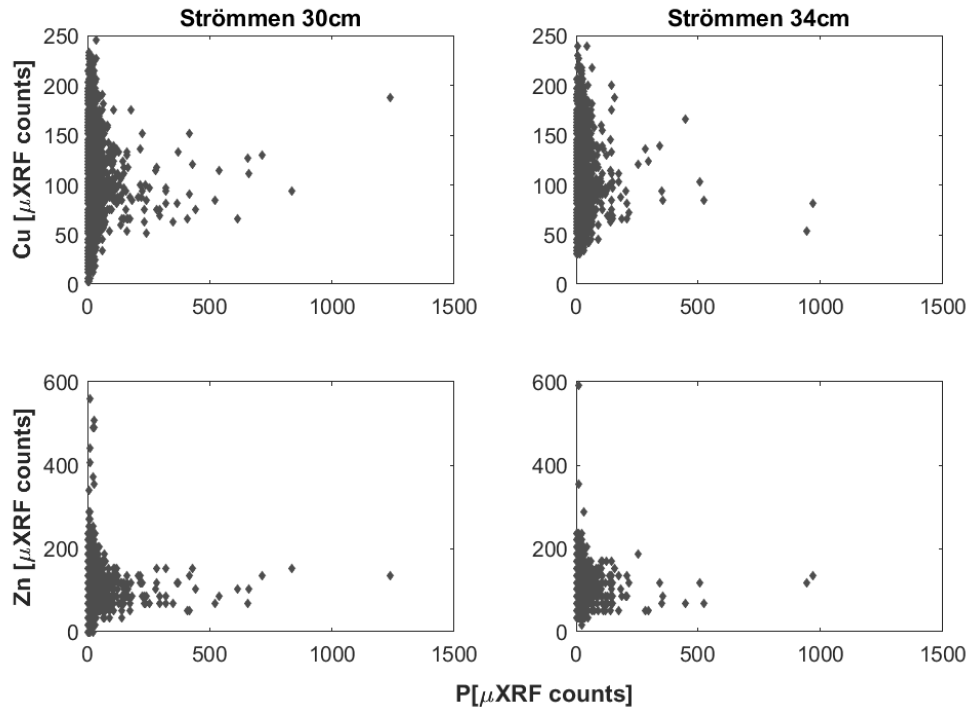


Figure 29: μ XRF count intensity of Cu and Zn against P respectively

Appendix G Water column trends of study sites

G.1 Strömmen

Figure 30 shows the dissolved oxygen and HPO_4^{2-} concentration trend in the water column at Strömmen between 2004 and 2009. Minima of dissolved oxygen in the bottom water are correlated to maxima in HPO_4^{2-} concentrations. This indicates potentially an increased efflux of HPO_4^{2-} from the sediment during low oxygen periods. The efflux might be related to the reduction of Fe-oxides.

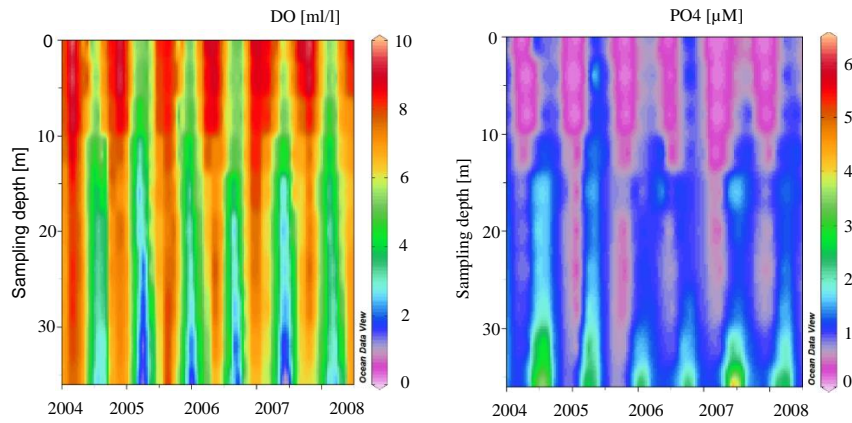


Figure 30: Dissolved oxygen and HPO_4^{2-} concentrations from the water column at Strömmen, 2004-2009. Data provided by the Swedish National Oceanographic Data Center/SHARK at the Swedish Meteorological and Hydrological Institute (SMHI)

G.2 ET5.1

The annual mean trend in temperature (T) shows an annual temperature range of 25 °C (Figure 31). Near fresh water conditions prevail during the first 5 months of the year, while higher salinities (up to 3) are reported in the second half of the year. During the summer DO concentrations are about 200 $\mu\text{mol/l}$ lower than during winter months. Coinciding to low oxygen concentrations, soluble reactive phosphorus (SRP) concentrations are slightly elevated.

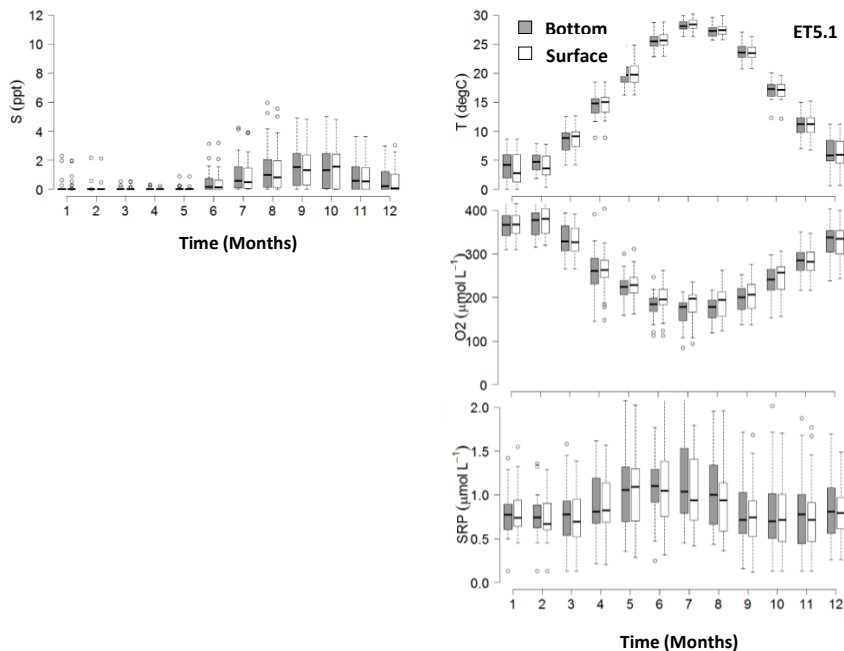


Figure 31: Annual mean salinity, temperature, oxygen and soluble reactive phosphorus trend in the surface and bottom water at ET5.1 from January 1986 to January 2018. Data is from the Chesapeake Bay Program (Accessed April 2018)

Figure 32 presents a time series of soluble reactive phosphorus (SRP) and dissolved oxygen (DO) concentrations in the surface and bottom water at ET5.1 from January 1986 to January 2018. An increase in SRP and a decline in DO is visible for this time period.

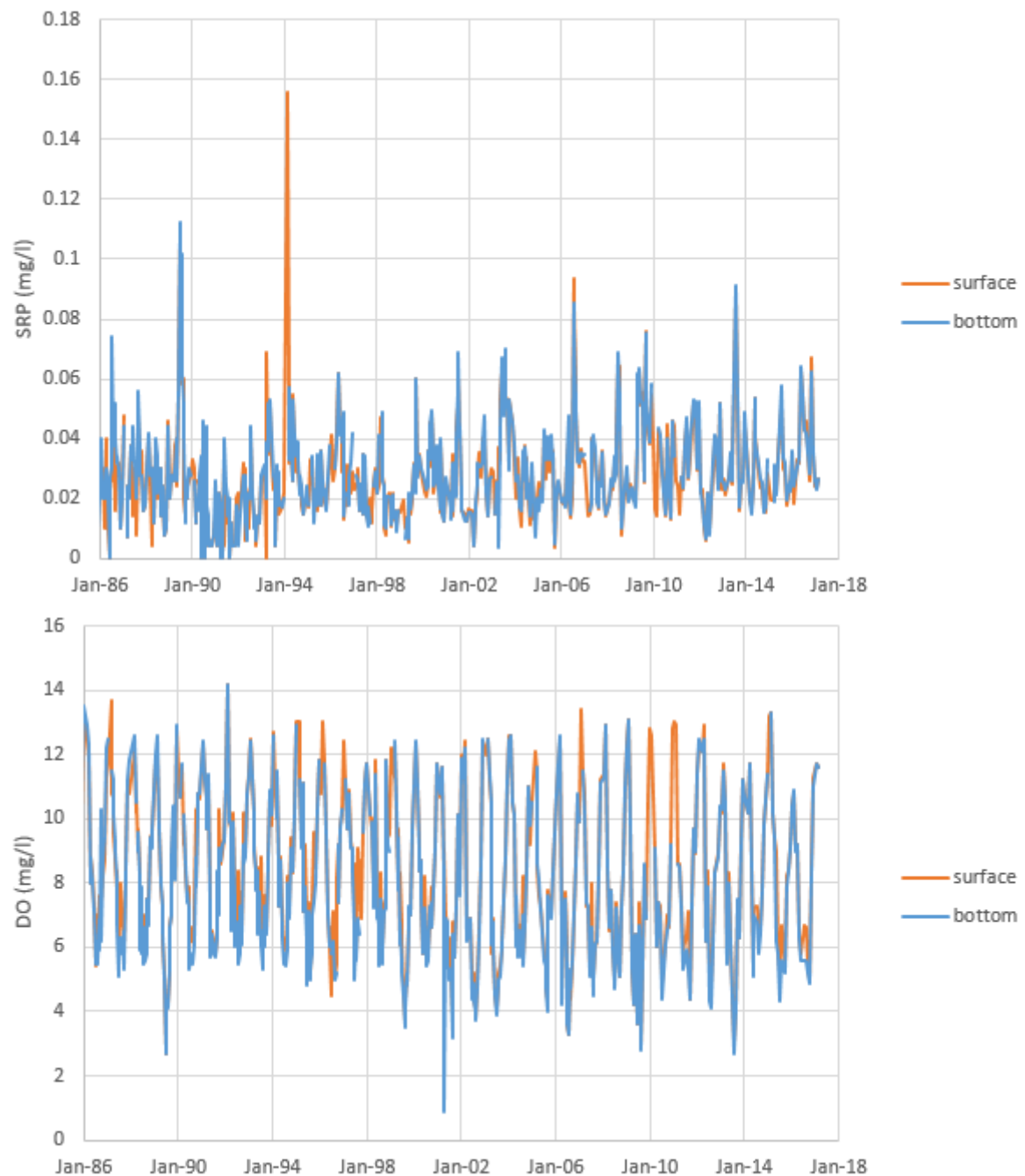


Figure 32: Soluble reactive phosphorus (SRP) (top) and dissolved oxygen (DO) (bottom) in the surface and bottom water at ET5.1 from January 1986 to January 2018. Data is from the Chesapeake Bay Program (Accessed April 2018)

G.3 CB2.2

The annual mean trend in temperature shows an annual temperature range of 25 °C (Figure 33). Salinity is the lowest during summer. Generally, a high range in salinity exist at CB2.2 (from 1 to nearly 10). The surface water has a significantly lower salinity than the bottom water, indicating stratification of the water column. During the summer DO concentrations are about 200 $\mu\text{mol/l}$ lower than during winter months. Coinciding to low oxygen concentrations, SRP concentrations are elevated at CB2.2. SRP concentrations in the bottom water are higher than in the surface water, indicating potentially that the sediment is a source for SRP during the summer. The release of SRP could then be related to increasing rates of OM degradation due to higher temperatures and possible Fe-oxide reduction in the anoxic sediments.

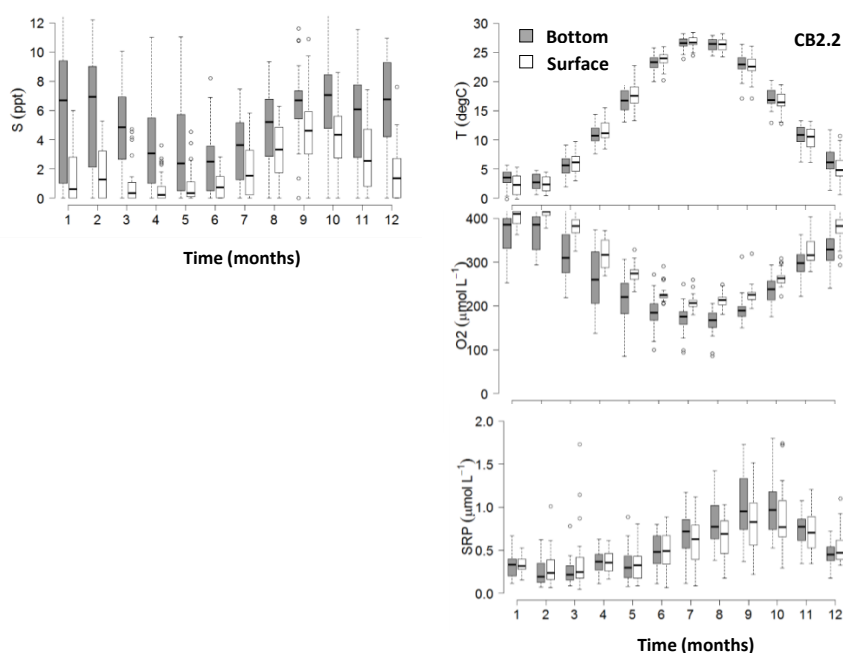


Figure 33: Annual mean salinity, temperature, oxygen and soluble reactive phosphorus trend in the surface and bottom water at CB2.2 from January 1986 to January 2018. Data is from the Chesapeake Bay Program (Accessed April 2018)

Figure 34 presents a time series of soluble reactive phosphorus (SRP) and dissolved oxygen (DO) concentrations in the surface and bottom water at CB2.2 from January 1986 to January 2018. An increase in SRP and a decline in DO is visible for this time period.

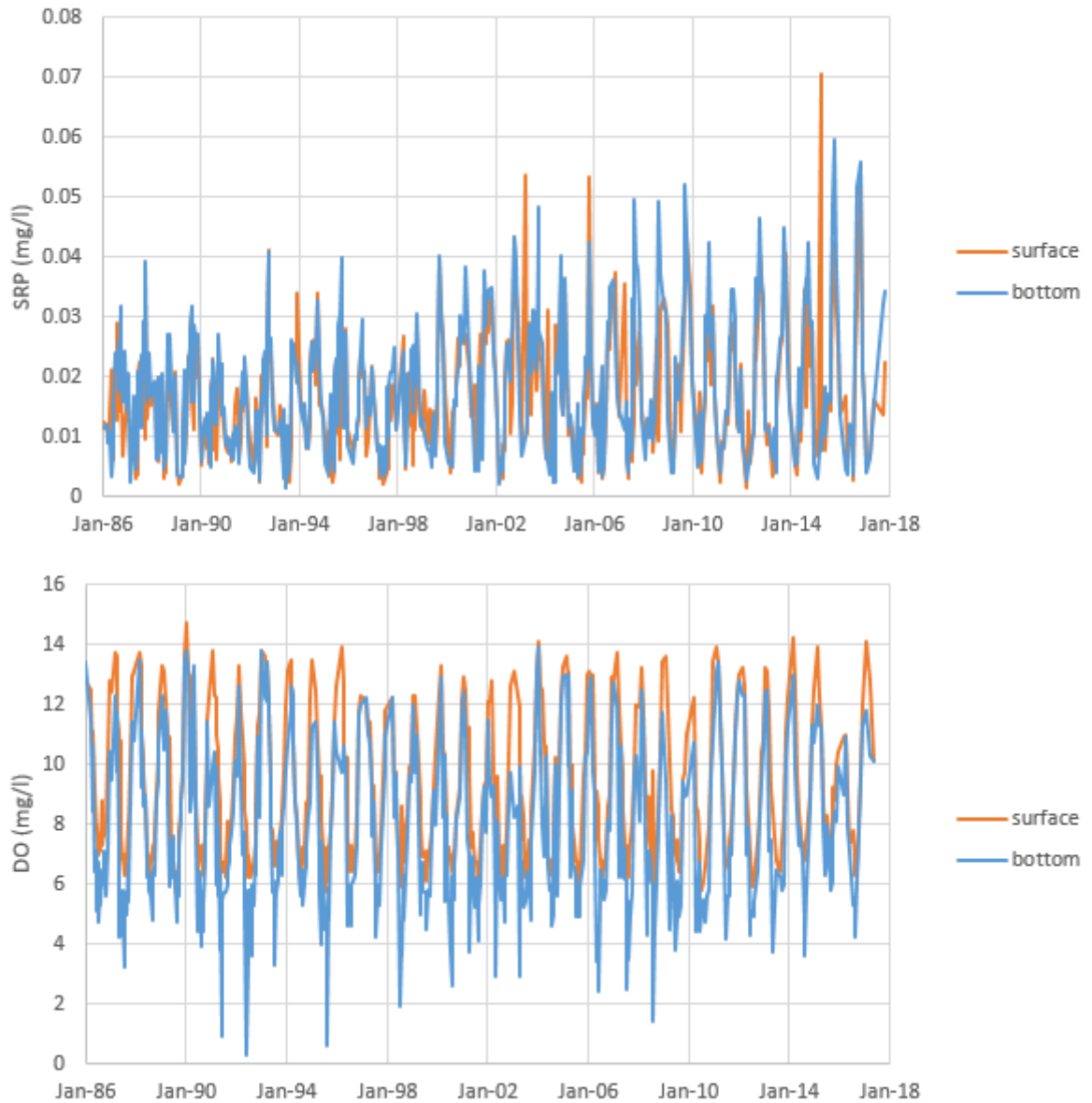


Figure 34: Soluble reactive phosphorus (SRP) (top) and dissolved oxygen (DO) (bottom) in the surface and bottom water at CB2.2 from January 1986 to January 2018. Data is from the Chesapeake Bay Program (Accessed April 2018)

Appendix H Calculations to estimate the amount of vivianite in the CDB-step

The same set of equations as presented in Egger et al. (2015) are used to estimate how much P of the Fe-bound P fraction might be associated to vivianite. Since a different Fe-extraction was used in this thesis, the set of equations were slightly adapted. Vivianite is supposed to dissolve in Step 1 and Step 2 of the Fe-extraction and CDB-step of SEDEX (Nembrini et al., 1983). Consequently, both fractions represent a combination of Fe and P associated with Fe-oxides (Fe_{FeOx} and P_{FeOx})

and vivianite ($Fe_{Vivianite}$ and $P_{Vivianite}$). The sum of Fe_{FeOx} and $Fe_{Vivianite}$ is the total amount of Fe dissolved during Step 1 (Fe(III)) and 2 of the Fe extraction. The sum of P_{FeOx} and $P_{Vivianite}$ is equal to the total CDB-P concentration. A typical ratio for Fe-oxide bound P is 10 (Fe_{FeOx}/P_{FeOx}) (Slomp et al., 1996). Combining this with the theoretical ratio of 1.5 for vivianite ($Fe_{Vivianite}/P_{Vivianite}$) (Egger et al., 2015) leads in a set of 4 equations with 4 unknowns.

$$Fe_{FeOx} + Fe_{Vivianite} = \text{Fe of Step 1 and Step 2 Fe-extraction} \quad (3)$$

$$P_{FeOx} + P_{Vivianite} = \text{CDB-P} \quad (4)$$

$$Fe_{FeOx} = 10P_{FeOx} \quad (5)$$

$$Fe_{Vivianite} = 1.5P_{Vivianite} \quad (6)$$

Solving these equations for $P_{Vivianite}$ provides then an estimate of the fraction of P possible associated to vivianite.

Appendix I Comparison of Strömmen, USB5 and Öre estuary

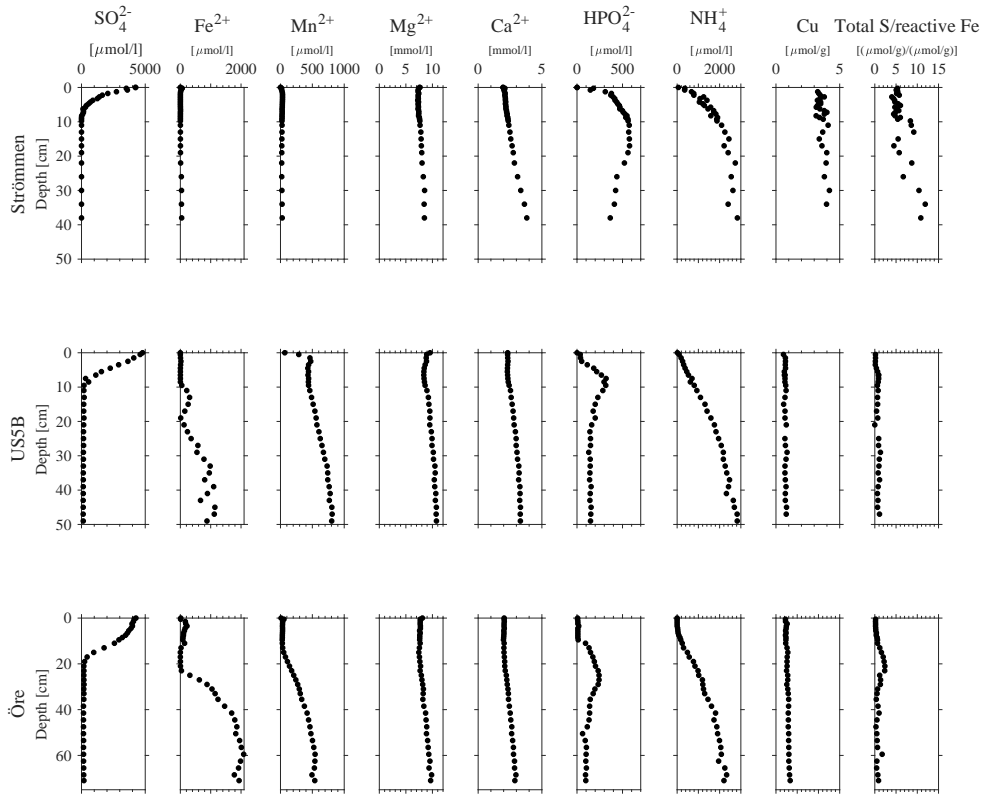


Figure 35: Depth profiles of SO_4^{2-} , Fe^{2+} , Mn^{2+} , Mg^{2+} , HPO_4^{2-} , NH_4^+ , Cu, and total S to reactive Fe at Strömmen, USB5 and Öre estuary. Data is from Egger et al. (2015) and Lenstra et al. (in prep.)